UNDERSTANDING GALACTIC COSMIC RAY MODULATION: OBSERVATIONS AND THEORY

Dissertation
zur Erlangung des Doktorgrades
der Mathematisch-Naturwissenschaftlichen Fakultät
der Christian-Albrechts-Universität zu Kiel
vorgelegt von

JAN GIESELER

– Kiel, Januar 2018 –

Jan Gieseler:
Understanding Galactic Cosmic Ray Modulation:
Observations and Theory

ERSTER GUTACHTER (SUPERVISOR):
Prof. Dr. B. Heber

ZWEITER GUTACHTER:
PD Dr. H. Fichtner

TAG DER MÜNDLICHEN PRÜFUNG:
27. März 2018

ABSTRACT

The modulation of Galactic Cosmic Rays (GCRs) in the heliosphere has been a topic of ongoing research almost since the first detection of GCRs more than 100 years ago. Over this time, different aspects of the modulation have been discovered and investigated, like various timescales and periodicities of variation, charge-sign effects correlating with the 22-year cycle of the Heliospheric Magnetic Field (HMF), or dependences of the modulation strength with the particle energy. One recent example of periodic short-term variations of GCRs and Jovian electrons is analyzed in the beginning of this thesis (Gieseler et al., 2009). But although GCR measurements were available for decades, they also were very often suffering from various observational limitations, whether it be the constrains in energy range and resolution or the lack of continuous observations over longer time periods and at different locations in the heliosphere.

In 1990, the Ulysses spacecraft was launched. With its peculiar, highly inclined orbit around the Sun and the Kiel Electron Telescope (KET) onboard (capable of measuring electrons and protons in the GV range, where the modulation shows significant effects), this mission allowed for unprecedented investigations of the spatial distribution of GCRs in the heliosphere and charge-sign effects of the modulation. Two such analyses are presented in this thesis: For the $A < 0$ solar minimum in the 2000s, the radial and latitudinal gradients of GCRs were calculated (Heber et al., 2008), and also charge-sign effects of this so-called unusual solar minimum were examined (Heber et al., 2009). However, this investigations were hindered by the fact that there were no corresponding measurements at Earth, and workarounds like comparison with same-rigidity particles of different species or assumptions regarding the behavior of different charged particles needed to be introduced. With the launch of the Payload for Antimatter Matter Exploration and Light-nuclei Astrophysics (PAMELA) detector on an Earth orbiting satellite in 2006, this gap was closed. PAMELA provided for the first time in-situ intensities of GCR electrons and protons (as well as higher nuclei and anti-particles) over a wide range of energy with unprecedented energy resolution and statistics. With this tool at hand, it was possible to re-investigate the radial and latitudinal gradients of positively charged GCRs for the 2000s $A < 0$ solar minimum with more accuracy than ever before (De Simone et al., 2011; Gieseler et al., 2013; Gieseler and Heber, 2016).

Additionally, the high-resolution rigidity spectrum of GCR protons provided by PAMELA allowed us to investigate the rigidity-dependence of the so-called force field approach. This is a very simple but also quite handy one-parameter model to describe the modulation of a given Local Interstellar Spectrum (LIS) throughout the heliosphere until it is observed at Earth. Demonstrating the severe limitations of this commonly used model, a straightforward and easy to use workaround introducing a rigidity-dependence is presented in the last part of this thesis (Gieseler et al., 2017).

ZUSAMMENFASSUNG

Die Modulation der Galaktischen Kosmischen Strahlung (GKS) in der Heliosphäre ist praktisch seit der Entdeckung der GKS vor mehr als 100 Jahren ein Thema andauernder Forschung. Im Laufe dieser Zeit wurden unterschiedliche Aspekte der Modulation entdeckt und untersucht, darunter verschiedene Zeitskalen und Periodizitäten der Variation, vorzeichenabhängige Effekte, die mit dem 22-Jahres-Zyklus des Heliosphärischen Magnetfeldes (HMF) korrelieren, oder Abhängigkeiten der Modulationsstärke von der Teilchenenergie. Ein aktuelles Beispiel periodischer, kurzzeitiger Variationen der GKS und von Jupiterelektronen wird zu Beginn dieser Arbeit analysiert (Gieseler et al., 2009). Aber obwohl GKS-Messungen seit Jahrzehnten verfügbar waren, litten sie die meiste Zeit über unter verschiedenen Beobachtungs-Einschränkungen. Seien es Limitierungen im messbaren Energiebereich oder der Energieauflösung, sei es ein Mangel an kontinuierlichen Beobachtungen über längere Zeiträume oder an verschiedenen Positionen in der Heliosphäre.

Im Jahr 1990 wurde die Raumsonde Ulysses gestartet. Mit ihrer außergewöhnlichen, stark geneigten Umlaufbahn um die Sonne und dem Kiel Electron Telescope (KET) an Bord (das Elektronen und Protonen im GV-Bereich messen konnte, wo die Modulation signifikante Auswirkungen zeigt) erlaubte diese Mission vorher nie dagewesene Untersuchungen der räumlichen Verteilung der GKS in der Heliosphäre sowie von vorzeichenabhängigen Effekten der Modulation. Zwei solche Untersuchungen werden in dieser Arbeit vorgestellt: Für das $A < 0$ solare Minimum in den 2000ern wurden die radialen und Breitengradienten der GKS berechnet (Heber et al., 2008). Außerdem wurden vorzeichenabhängige Effekte während dieses sogenannten ungewöhnlichen solaren Minimums untersucht (Heber et al., 2009). Allerdings wurden diese Analysen dadurch eingeschränkt, dass keine vergleichbaren Messungen an der Erde zur Verfügung standen. Deshalb mussten Behelfslösungen gefunden werden, etwa indem Teilchen gleicher Steifigkeit aber unterschiedlicher Spezies verglichen wurden, oder indem Annahmen betreffend des Verhaltens von Teilchen mit unterschiedlichen Ladungsvorzeichen getroffen wurden. Mit dem Start des Detektors Payload for Antimatter Matter Exploration and Light-nuclei Astrophysics (PAMELA) auf einem die Erde umkreisenden Satelliten im Jahr 2006 wurde diese Lücke geschlossen. PAMELA ermöglichte zum ersten Mal die In-situ-Messung der GKS-Intensitäten von Elektronen und Protonen (sowie schwererer Elemente und Antiteilchen) über einen großen Energiebereich mit bis dahin unerreichter Energieauflösung und Statistik. Mit diesen Mitteln konnten die radialen und Breitengradienten der GKS für das 2000er $A < 0$ solare Minimum mit höherer Genauigkeit als je zuvor und für neue Energien untersucht werden (De Simone et al., 2011; Gieseler et al., 2013; Gieseler and Heber, 2016).

Darüber hinaus ermöglicht das von PAMELA gemessene, hochaufgelöste Steifigkeitsspektrum von GKS-Protonen die Untersuchung der Steifigkeitsabhängigkeit

des sogenannten Force-Field-Ansatzes. Hierbei handelt es sich um ein sehr einfaches, aber auch leicht nutzbares Modell mit nur einem Parameter, mit dem sich die Modulation des Lokalen Interstellaren Spektrums (LIS) durch die Heliosphäre bis zur Messung an der Erde beschreiben lässt. Nach der Demonstration der schwerwiegenden Einschränkungen dieses weitverbreiteten Modells wird eine einfache und leicht zu nutzende Behelfslösung vorgeschlagen, die eine Steifigkeitsabhängigkeit integriert (Gieseler et al., 2017).

PUBLICATIONS

Latitudinal gradients of galactic cosmic rays during the 2007 solar minimum

Heber, B., **J. Gieseler**, P. Dunzlaff, R. Gómez-Herrero, A. Klassen, R. Müller-Mellin, R. A. Mewaldt, M. S. Potgieter, S. E. S. Ferreira, *Astrophys. J.*, 689, 2, 1443-1447 (2008), DOI:10.1086/592596

Modulation of galactic cosmic ray protons and electrons during an unusual solar minimum

Heber, B., A. Kopp, **J. Gieseler**, R. Müller-Mellin, H. Fichtner, K. Scherer, M. S. Potgieter, S. E. S. Ferreira, *Astrophys. J.*, 699, 2, 1956-1963 (2009), DOI:10.1088/0004-637X/699/2/1956

Latitudinal and radial gradients of galactic cosmic ray protons in the inner heliosphere – PAMELA and Ulysses observations

De Simone, N., V. Di Felice, **J. Gieseler**, M. Boezio, M. Casolino, P. Picozza, PAMELA Collaboration, and B. Heber, *Astrophys. Space Sci. Trans.*, 7, 425-434 (2011), DOI:10.5194/astra-7-425-2011

Simultaneous analysis of recurrent Jovian electron increases and galactic cosmic ray decreases

Kühl, P., N. Dresing, P. Dunzlaff, H. Fichtner, **J. Gieseler**, R. Gómez-Herrero, B. Heber, A. Klassen, J. Kleimann, A. Kopp, M. Potgieter, K. Scherer, R. D. Strauss, *Central European Astrophysical Bulletin*, 37, 643-648 (2013)

Mini neutron monitor measurements at the Neumayer III station and on the German research vessel Polarstern

Heber, B., D. Galsdorf, K. Herbst, **J. Gieseler**, J. Labrenz, C. Schwerdt, M. Walter, G. Benadé, R. Fuchs, H. Krüger, H. Moraal, *Journal of Physics: Conference Series*, 632, 1, 012057 (2015), DOI:10.1088/1742-6596/632/1/012057

Spatial gradients of GCR protons in the inner heliosphere derived from Ulysses COSPIN/KET and PAMELA measurements

Gieseler, J., and B. Heber, *Astron. Astrophys.*, 589, A32 (2016), DOI:10.1051/0004-6361/201527972

An empirical modification of the force field approach to describe the modulation of galactic cosmic rays close to Earth in a broad range of rigidities

Gieseler, J., B. Heber, and K. Herbst, *J. Geophys. Res.: Space Phys.*, 122 (2017), DOI:10.1002/2017JA024763

CONFERENCE PROCEEDINGS

The radial gradient of galactic cosmic rays: Ulysses KET and ACE CRIS Measurements

Gieseler, J., B. Heber, P. Dunzlaff, R. Müller-Mellin, A. Klassen, R. Gómez-Herrero, H. Kunow, R. Wimmer-Schweingruber, and R. A. Mewaldt, *Proc. 30th Internat. Cosmic Ray Conf. (Mérida, Mexico)*, 1, 354, 571-574 (2008)

Recurrent modulation of galactic cosmic rays: A comparative study between IMP, SOHO, STEREO, and Ulysses

Gieseler, J., N. Dresing, P. Dunzlaf, R. Gómez-Herrero, B. Heber, A. Klassen, A. Kopp, R. Müller-Mellin, M. S. Potgieter, and S. E. S. Ferreira, *Proc. 31st Internat. Cosmic Ray Conf. (Lodz, Poland)* (2009)

Inner heliosphere spatial gradients of GCR protons in the low GeV range

Gieseler, J., M. Boezio, M. Casolino, N. De Simone, V. Di Felice, B. Heber, M. Martucci, P. Picozza, and the PAMELA Collaboration, *Proc. 33rd Internat. Cosmic Ray Conf. (Rio de Janeiro, Brazil)*, 341 (2013)

Mini neutron monitor measurements at the Neumayer III station and on the German research vessel Polarstern

Heber, B., D. Galsdorf, **J. Gieseler**, K. Herbst, M. Walter, A. Stoessl, H. Moraal, H. Krüger, G. Benadé, *Proc. 34th Internat. Cosmic Ray Conf. (The Hague, The Netherlands)* (2015)

Galactic cosmic ray spectra during solar cycle 23 and 24 - Measurement capabilities of the Electron Proton Helium Instrument

Kühl, P., N. Dresing, **J. Gieseler**, B. Heber, A. Klassen, *Proc. 34th Internat. Cosmic Ray Conf. (The Hague, The Netherlands)* (2015)

CONTENTS

ACRONYMS

ACE	Advanced Composition Explorer
ACR	Anomalous Cosmic Ray
AMS-01	Alpha Magnetic Spectrometer (test mission)
AMS-02	Alpha Magnetic Spectrometer
BESS	Balloon-borne Experiment with Superconducting Spectrometer
CIR	Corotating Interaction Region
CME	Coronal Mass Ejection
COSPIN	Cosmic Ray and Solar Particle Investigation
CR	Cosmic Ray
CRIS	Cosmic Ray Isotope Spectrometer
EPHIN	Electron Proton Helium Instrument
FF	Force Field
FLS	Fast Latitude Scan
GCR	Galactic Cosmic Ray
GKS	Galaktische Kosmische Strahlung
GEANT	Geometry and Tracking
GLE	Ground Level Enhancement
GONG	Global Oscillation Network Group
HCS	Heliospheric Current Sheet
HG	Heliographic
HMF	Heliospheric Magnetic Field
IMF	Interplanetary Magnetic Field
IMP-8	Interplanetary Monitoring Platform 8
ISEE 3/ICE	International Sun-Earth Explorer 3/International Cometary Explorer

ISM	Interstellar Medium
ISS	International Space Station
KET	Kiel Electron Telescope
LIS	Local Interstellar Spectrum
MC	Monte Carlo
PAMELA	Payload for Antimatter Matter Exploration and Light-nuclei Astrophysics
RCRD	Recurrent Cosmic Ray Decrease
SOHO	Solar and Heliospheric Observatory
STEREO	Solar Terrestrial Relations Observatory
SWEPAM	Solar Wind Electron Proton Alpha Monitor
VLISM	Very Local Interstellar Medium

1

INTRODUCTION

1.1 THE SUN AND THE HELIOSPHERE

Our Sun is an active star. It emits a continuous radial stream of supersonic plasma, the so-called solar wind (see e.g. Schwenn, 2006). Embedded within is the solar magnetic field. As it is transported through the interplanetary medium, the Interplanetary Magnetic Field (IMF) – nowadays more often named Heliospheric Magnetic Field (HMF) (Owens and Forsyth, 2013) – is established. Because the HMF remains rooted at the photosphere of the rotating Sun, it forms an Archimedean or so-called Parker spiral (Parker, 1958; Owens and Forsyth, 2013). In addition, a current sheet is established as the boundary surface between the two magnetic polarity hemispheres of the Sun's dipole field. Because the magnetic field dipole axis and the solar rotation axis are tilted, this Heliospheric Current Sheet (HCS) exhibits a wavy structure (see Fig. 1).

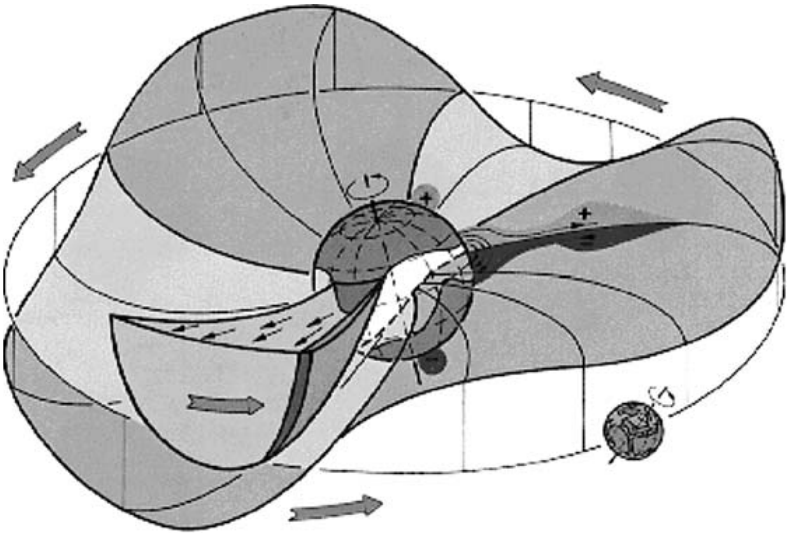

Figure 1: Sketch of the Heliospheric Current Sheet (HCS), the boundary between regions of different HMF polarities. Figure reproduced from Heber and Potgieter (2006, adapted from Schwenn, 1990) by permission of Springer, ©2007.

The heliosphere – the region of space that is dominated by the solar wind and the HMF – is embedded in the Interstellar Medium (ISM). At the termination shock the solar wind becomes subsonic, it is slowed down and deflected inside the heliosheath. The heliopause marks the boundary between the heliosheath and the Very Local Interstellar Medium (VLISM), which is also deflected. Figure 2 (from Owens and Forsyth, 2013) illustrates this scenario. The existence of the previously predicted bow shock is recently under scientific debate (McComas et al., 2012; Zank et al., 2013; Zieger et al., 2013; Scherer and Fichtner, 2014; Schwadron et al., 2015).

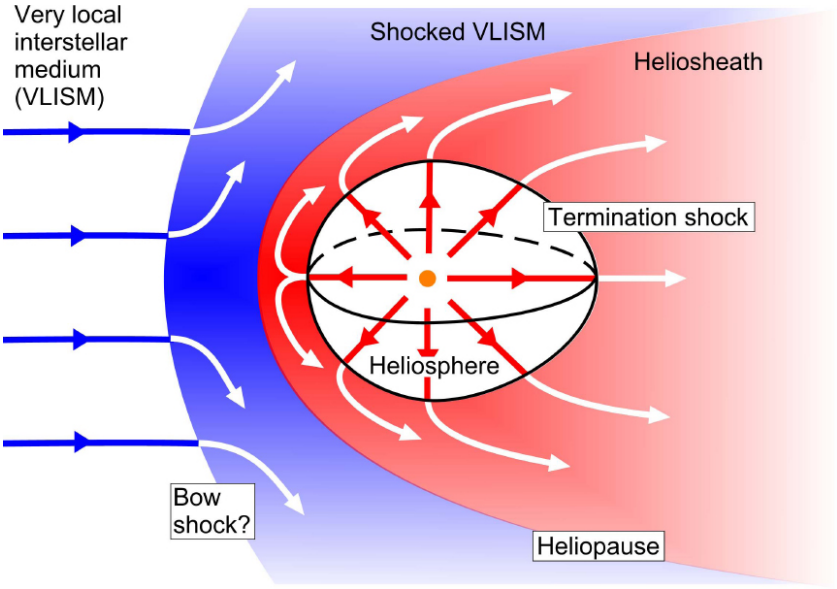

Figure 2: Sketch of the global structure of the heliosphere and its surrounding (see text for details). Figure reproduced from Owens and Forsyth (2013), available under a Creative Commons Attribution-Non-Commercial 3.0 Germany License: https://creativecommons.org/licenses/by-nc/3.0/de/ .

1.2 GALACTIC COSMIC RAYS

The discovery of Galactic Cosmic Rays (GCRs) is mostly connected to the ionization chamber observations on balloon flights by Hess (1912). Until the 1950s, various ground-based detectors like ionization chambers, Geiger counters, muon telescopes and neutron monitors were installed all over the world (see Stoker, 2009, for a historical overview). Especially neutron monitors play an important role because some of them provide more than 50 years of uninterrupted observations (e.g. Fig. 3, top). They measure the integrated GCR flux above their individual, location based vertical geomagnetic cutoff rigidity (Smart and Shea, 2009), which is in the range of 0.1–10 GV. This is due to the fact that neutron monitors do not measure the primary component of GCRs, instead they detect secondary particles produced in the Earth's atmosphere. Only since the 1960s instruments onboard spacecraft are able to measure GCRs directly and at lower energies.

When we talk about GCRs today, we mean Cosmic Rays (CRs) that are of galactic origin (or beyond) and enter the heliosphere almost isotropically and time-independent. It is widely believed that diffusive particle acceleration at supernova remnants is the main source of the bulk of these GCRs (see Blasi, 2013, for a review). Other parts of the general ensemble of CRs are Anomalous Cosmic Rays (ACRs), which are produced inside the heliosphere and connect to the GCR spectrum at lower energies. They show differences in composition, charge states and spectral slope compared to GCRs (Fichtner, 2001; Giacalone et al., 2012). Solar energetic particles that are accelerated at the Sun, are sometimes also called solar cosmic rays (e.g. McCracken and Rao, 1970). Another population of energetic particles in the heliosphere are Jovian electrons, which are accelerated at Jupiter's

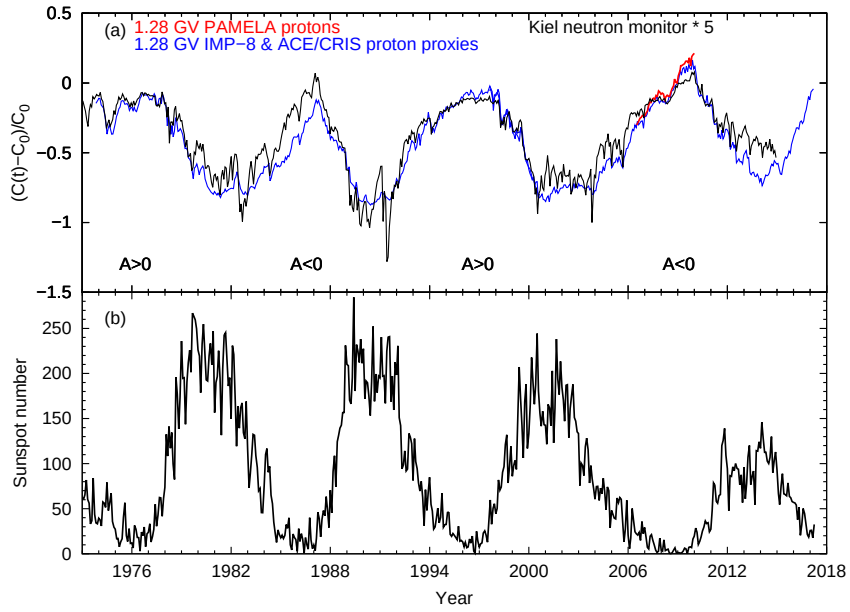

Figure 3: Top: Monthly averaged count rate variation of the Kiel neutron monitor (black curve, multiplied by 5 to match scale), intensity variation of 1.28 GV proton measurements by PAMELA (red curve), and the intensity variations of 1.28 GV "proton proxies" helium and carbon (blue curves, see Sect. 5.1.3 for details). The data have been normalized to January 2009. Bottom: Monthly sunspot number from the Royal Observatory of Belgium (http://www.sidc.be/silso/). Figure reproduced from Gieseler et al. (2017) by permission of John Wiley & Sons, Inc. ©2017 American Geophysical Union.

magnetosphere (Teegarden et al., 1974). These particles constitute the bulk of electrons between 5–30 MeV during solar quite times (Chenette, 1980).

GCRs are actually particle radiation and only historically called rays. They consist approximately of 99% fully ionized atoms, from which 90% are protons, 9% α-particles and the rest heavier elements (Gaisser and Stanev, 2006). The remaining 1% are mostly electrons, with only a small fraction of positrons and antiprotons (cf. Fig. 4, from Gaisser, 2007). GCRs range from MeVs up to TeVs. Above a few GeV they follow a power law with an index of ∼-2.7. This slope changes to ∼-3.0 at around 10^6 GeV and back to ∼-2.7 above 10^9 GeV (see Fig. 4).

1.3 SOLAR MODULATION

Outside the heliosphere is the VLISM, which is populated by GCRs. They define the Local Interstellar Spectrum (LIS), which in general is believed to be isotropic and constant over time. The Voyager 1 and 2 spacecraft passed the termination shock at 94 AU (Stone et al., 2005) and 84 AU (Richardson et al., 2008), respectively, and Voyager 1 the heliopause at 121 AU (Gurnett et al., 2013), allowing for the first direct measurements of GCRs outside the solar wind dominated space (Stone et al., 2013; Cummings et al., 2016). Previous LIS models had to rely on galactic propagation models and indirect measurements at Earth, respectively. Figure 5 (from Herbst et al., 2017) compares different LIS models from the literature that

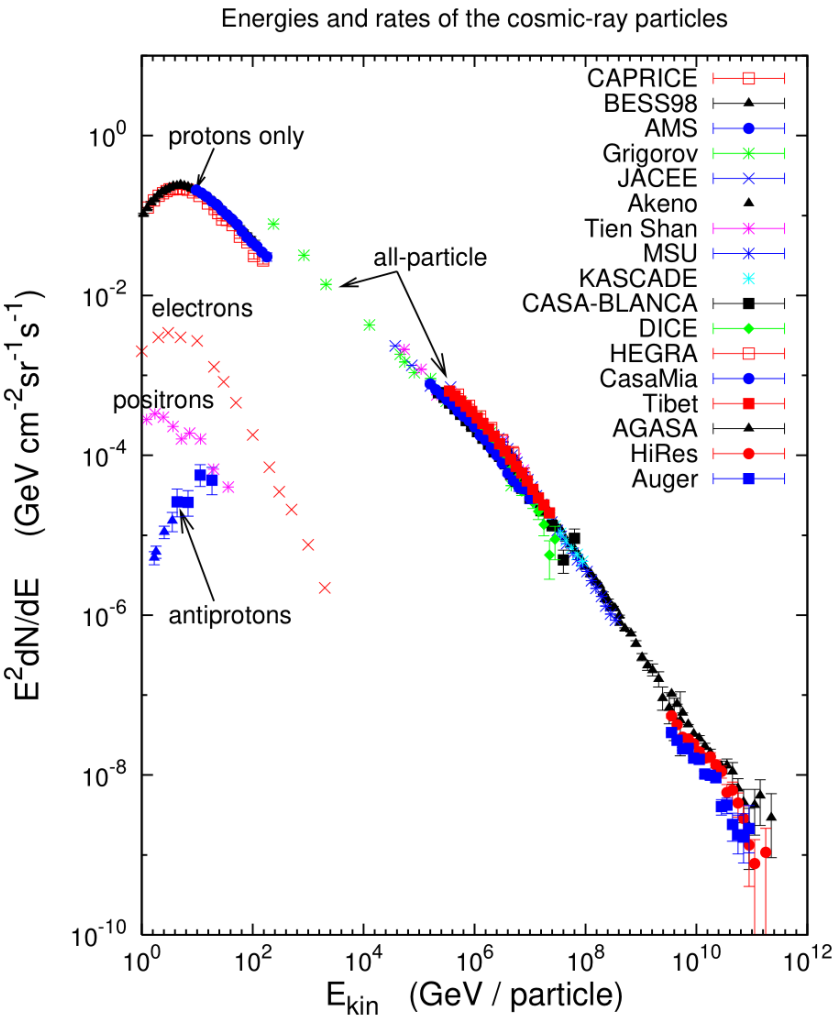

Figure 4: Spectrum of Cosmic Rays (CRs) based on various measurements. Figure reproduced from Gaisser (2007) by permission of World Scientific Publishing, ©2007.

were established prior (Garcia-Munoz et al., 1975; Webber and Higbie, 2003; Usoskin et al., 2005; Potgieter et al., 2014) and past (Bisschoff and Potgieter, 2016; Corti et al., 2016; Herbst et al., 2017) the recent Voyager 1 findings, which are also presented together with observations at Earth by PAMELA (Adriani et al., 2013) and the Alpha Magnetic Spectrometer (Alpha Magnetic Spectrometer (AMS-02), Aguilar et al., 2015). This figure illustrates that the earlier models differ quite significantly in comparison to the Voyager 1 measurements (see also Sect. 5.2).

As the GCRs enter and travel through the heliosphere, they are affected by the solar wind and the embedded HMF. This process is globally described as solar modulation (see Potgieter, 2013a, for a review). GCRs were already observed for a long time when Parker (1965) introduced a basic transport equation that for the first time incorporated the different drivers of the solar modulation of GCRs into one equation, the so-called Parker equation. This Fokker-Planck type equation, presented as Eq. 1 in the notation given by Potgieter (2013a), describes the time

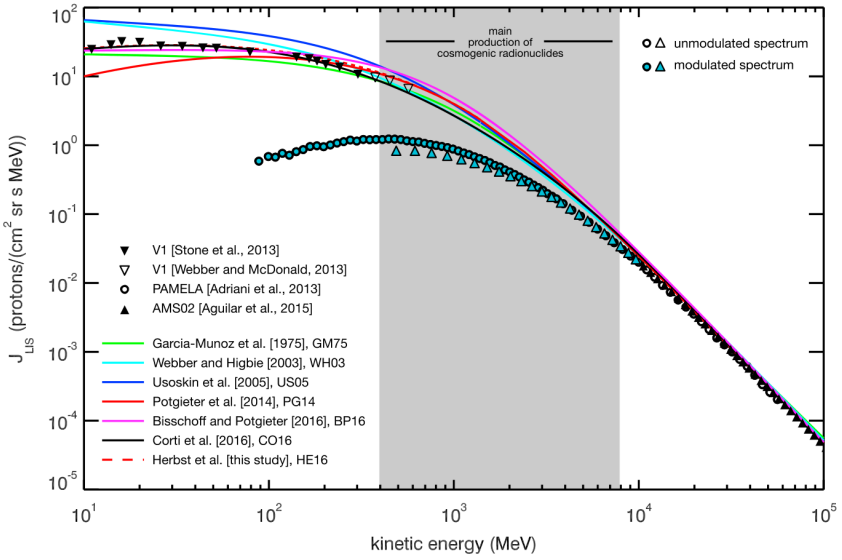

Figure 5: Comparison of different LIS models (see text for details) and observations by Voyager 1 (downward triangles), PAMELA (circles), and AMS-02 (upward triangles). Figure reproduced from Herbst et al. (2017) by permission of John Wiley & Sons, Inc. ©2016 American Geophysical Union.

evolution of the differential CR phase space distribution function $f(\mathbf{r}, P, t)$ inside the heliosphere:

$$\frac{\partial f}{\partial t} = -\Big(\underbrace{\mathbf{V}}_{\text{i}} + \underbrace{\langle \mathbf{v}_D \rangle}_{\text{ii}}\Big) \cdot \nabla f + \underbrace{\nabla \cdot (\mathbf{K_s} \cdot \nabla f)}_{\text{iii}} + \underbrace{\frac{1}{3} (\nabla \cdot \mathbf{V}) \frac{\partial f}{\partial \ln P}}_{\text{iv}} + \underbrace{Q}_{\text{v}}, \qquad (1)$$

where $\mathbf{r}$ denotes the spatial coordinates, P the particle rigidity, t the time, $\mathbf{V}$ the solar wind velocity, $\mathbf{v}_D$ the particle drift velocity, and $\mathbf{K_s}$ the symmetrical diffusion tensor. The different processes causing the solar modulation are:

(i) outward convection with the solar wind,

(ii) gradient and curvature drifts in the HMF,

(iii) diffusion due to scattering in irregularities of the HMF,

(iv) adiabatic energy changes due to the divergence of the expanding solar wind,

(v) local sources like particles accelerated at the Sun or Jupiter's magnetosphere.

An illustration of these major transport processes is shown in Fig. 6 (from Moraal, 1993).

Although almost all main processes governing the solar modulation of cosmic rays are known since 1965, detailed understanding and the relative importance of the various mechanisms are still a field of ongoing research (see e.g. Potgieter, 1998; Potgieter et al., 2001; Potgieter, 2013b, 2017). This is due to the fact that direct measurements in the heliosphere are very limited in time and especially space – the available spacecraft observations are just mere point measurements. But also because analytical solutions to the Parker equation are only available

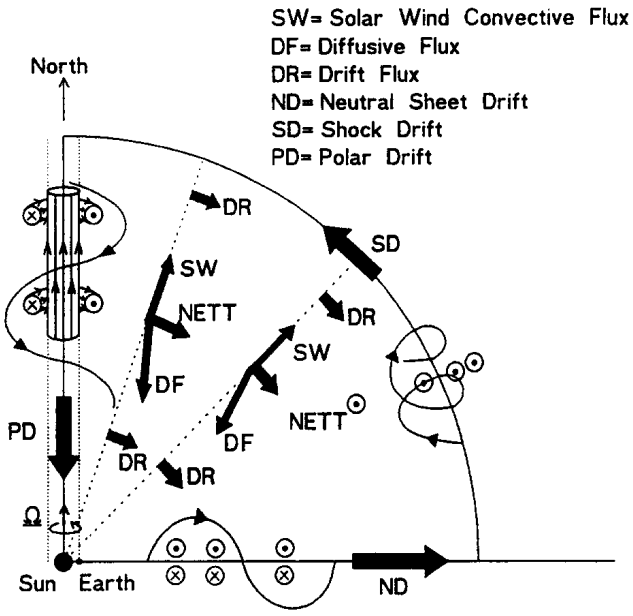

Figure 6: Side-view of a quarter heliosphere illustrating the major CR transport processes for positively charged particles in an $A > 0$ solar epoch (cf. Chap. 3 for more details). Figure reproduced from Moraal (1993) by permission of Elsevier, ©1993.

for special cases (see Quenby, 1984, and references therein for more examples). Otherwise one has to rely on numerical models (see e.g. Strauss and Effenberger, 2017, for an overview on the in recent years frequently used stochastic differential equation models), which depend heavily on computing power. While today this is no longer a severe limiting factor, it has been in the past.

Because GCRs originate outside the heliosphere and undergo as they travel through the heliosphere different modulation processes as described by Eq. 1, they show a clear radial gradient in intensity (e.g. Fujii and McDonald, 1997, 2005). Of more interest is the latitudinal gradient of GCRs, which shows a dependence on rigidity and – due to drift effects – on charge-sign and the polarity of the HMF (see Heber and Potgieter, 2006, and references therein, and Chap. 3).

The effect of GCR modulation varies with the solar activity, as can be seen in Fig. 3. The solar activity – presented in the bottom panel with the sunspot number as a proxy – shows a 11-year cycle (see Hathaway, 2015, for a review). There is a clear anti-correlation between the GCR intensity given by neutron monitor observations in the top panel and the solar activity. On top of this 11-year variation lies a 22-year cycle, which appears in GCR observations but is not seen in sunspot numbers. Every 22 years the maximum of GCRs during solar minimum conditions shows a peaked structure (around 1987 and 2010), whereas in the remaining solar minima there are more plateau-like GCR intensity maxima (around 1976 and 1997, cf. Fig. 3). This 22-year cycle is defined by the reversal of the solar magnetic field polarity (Hathaway, 2015), and its influence on drift processes (more details in Chaps. 3 and 4). If the magnetic field is pointing outward over the northern and inward over the southern solar hemisphere, it is called an $A > 0$ solar magnetic epoch, and vice versa for an $A < 0$ epoch. The solar magnetic field polarity is also responsible for an apparent charge-sign dependence in the GCR

modulation: The 22-year cycle variation shown in the upper panel of Fig. 3 reflects the time evolution of positively charged particles. Negatively charged GCRs – predominantly electrons – behave the other way around with peaked maxima during $A > 0$ and flat maxima during $A < 0$ solar cycles (e.g. Fig. 8 in Heber et al., 2009, see Chap. 4). This is due to the fact that same-rigidity particles of opposite polarity are affected differently by drift processes in the heliosphere, leading to different modulation effects (see e.g. Heber et al., 2002, 2009; Di Felice et al., 2017; and Potgieter, 2013a, for an overview).

While the 11- and 22-year cycles are the dominant periodicities in GCR observations, there are additional time scales of GCR variation. Longer cycles with time scales of centuries can be derived from cosmogenic isotopes in natural archives like tree rings or ice cores (see e.g. Usoskin, 2013, for a review). On the other hand, different short-term variations in GCR intensities can be observed (see Adriani et al., 2018, for a current short overview). The most prominent are: the long-known diurnal variation (e.g. Compton and Getting, 1935); singular and sudden so-called Forbush decreases, caused by Coronal Mass Ejections (CMEs) (first described by Forbush, 1937; see Cane, 2000, for a review); and recurrent variations with a periodicity of 27 days. The latter are connected to the occurrence of Corotating Interaction Regions (CIRs) (Simpson, 1954; see Richardson, 2004, for an overview), see also Chap. 2 for more details.

The modulation of GCRs affects only the low-energy part of the whole spectrum, below ∼50 GeV. This is demonstrated by monthly spectra measured by PAMELA from July 2006 to January 2010 (Adriani et al., 2013) shown in Fig. 7. Especially the bottom panel, which shows the ratios of the spectra normalized to that of July 2006, illustrates the energy dependence of GCR modulation: Its effect is highest at the lowest observed energies and decreases with increasing energy, until it vanishes (within the uncertainties) at around 30 GeV. This figure also demonstrates the temporal change of GCR modulation from 2006 to 2010, yielding in December 2009 the highest GCR intensities observed so far.

1.4 MOTIVATION

As already mentioned, a restricting factor for the analysis of GCR modulation has always been the lack of available observations. Although neutron monitors provide sustained GCR measurements for more than 50 years, they only give an indication of the variation over a wide range of energy above their individual geomagnetic and atmospheric cutoff, which is only known by simulations of the magneto- and atmosphere (Smart and Shea, 2009). On the other hand, instruments onboard spacecraft offered more precise (with respect to energy) measurements but usually only over a very confined energy range. Furthermore, they suffered from their in most cases limited mission time, rarely covering a whole solar cycle. This situation is illustrated in Fig. 8 (from Bindi et al., 2017), where an overview is given for most space and balloon experiments measuring GCR protons, helium and heavier ions above 0.4 GV with the respective rigidity ranges. An improvement to most of these shortcomings took place first with the launch of the PAMELA detector onboard an Earth orbiting satellite in 2006 (Picozza et al., 2007), and

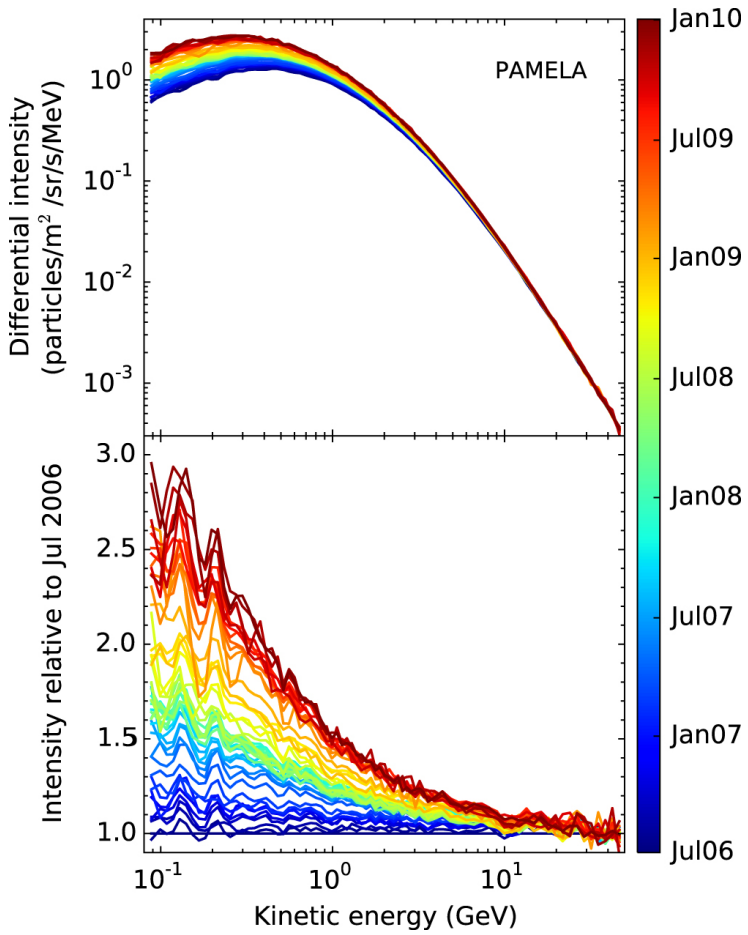

Figure 7: Top: 27-day averaged proton spectra measured by PAMELA between July 2006 (blue) and January 2010 (red) (Adriani et al., 2013). The December 2009 spectrum showed the highest intensities ever observed. Bottom: Ratios of the top spectra normalized to that of July 2006. Figure reproduced from Vos and Potgieter (2015) by permission of the AAS, ©2015.

later with the installation of AMS-02 on the International Space Station (ISS) in 2011 (Aguilar et al., 2013). The heart of the detector is in both cases a huge (compared to spacecraft instruments) permanent magnet spectrometer, which allows to detect electrons, protons and heavier ions as well as their anti-particles with unprecedented accuracy. With these tools, the whole energy spectrum of different GCR particles can be observed with very good statistics and a high energy resolution from lower energies around 0.1 GeV – where modulation is significant – up to hundreds of GeV. However, these missions are still limited in the way that they only deliver data since 2006 and that they only measure the GCR intensities at Earth. Thus, for worthwhile endeavors like the analysis of the spatial distribution of GCRs in the heliosphere or the temporal variations over longer time periods, one still depends on observations of other missions.

In order to investigate the spatial distribution of GCRs, that is, calculating their radial and latitudinal gradients, we can take advantage of the Ulysses mission with its peculiar, highly inclined orbit around the Sun. Although this mission ended in 2009, the three years of overlap with PAMELA observations give an

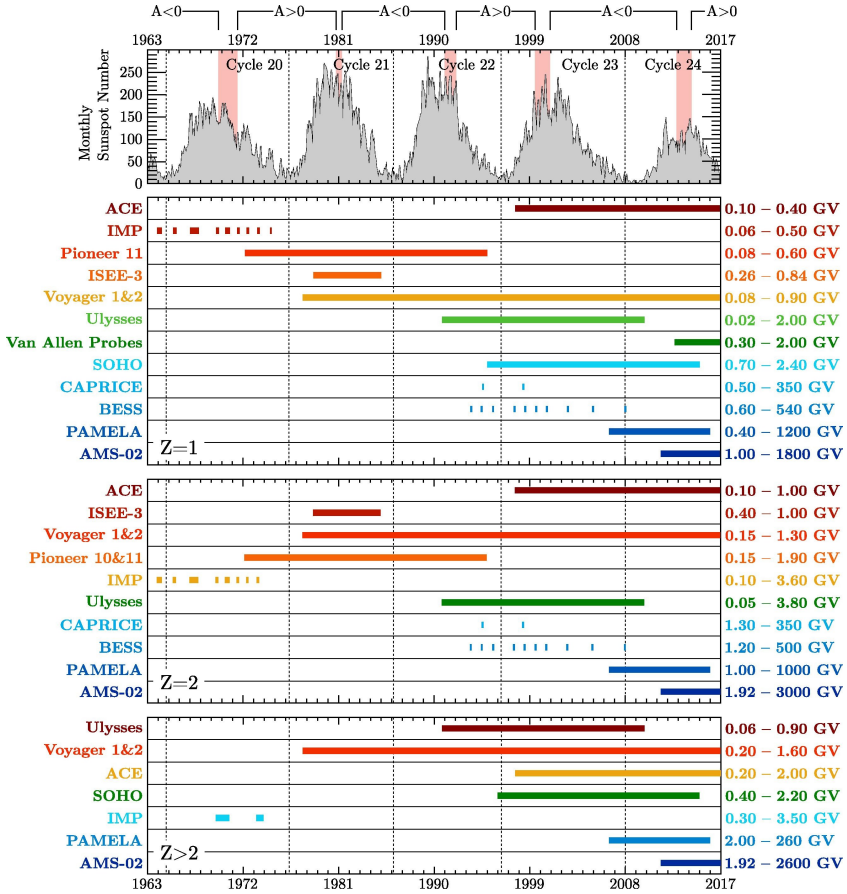

Figure 8: Overview of time periods of selected GCR observations for protons (Z=1), helium (Z=2) and heavier ions (Z>2) above 0.4 GV with the respective rigidity ranges (on the right). Note that in contrast to this picture IMP-8 actually provided continuous measurements of protons and helium from 1974 up to 2000. The corresponding solar activity is presented on top by the sunspot number; the time periods marked by red shading indicate the reversal of the solar magnetic field. Figure reproduced from Bindi et al. (2017) by permission of Elsevier, ©2017 COSPAR.

unique opportunity to calculate the gradients between Ulysses and PAMELA at 1 AU because now for the first time it is possible to compare same-rigidity proton measurements in the 2000s $A < 0$ solar minimum. This allows to re-investigate and improve previous findings. The open questions that will be addressed in Chap. 3 are:

- Are our previous findings from Heber et al. (2008) using measurements of helium from Ulysses/KET and of carbon from the Cosmic Ray Isotope Spectrometer (CRIS) onboard the Advanced Composition Explorer (ACE) confirmed?
- How does the latitudinal gradient change with rigidity?
- Does this latitudinal gradient follow the rigidity-dependence predicted by the model from Potgieter et al. (2001)?

The study of the long-term GCR modulation is another topic of this work (see Chap. 5). A part of this stuy is the connection of previous and current observations by detectors with limited energy resolution like ACE/CRIS, the IMP-8 or neutron monitors with the available precise measurements by PAMELA. Although the energy determination of the prior instruments may not be as accurate as the newest ones, their measured temporal variation can be normalized to the up-to-date observations, allowing to construct past time series of GCR intensity levels at a given rigidity. Another possibility to describe the GCR modulation is the temporal variation of the so-called force field potential, which can – together with a given LIS – reproduce the full GCR spectrum at Earth (see Chap. 5 for details). With the high-resolution rigidity spectrum provided by PAMELA, it is for the first time possible to investigate the overall validity of this force field approach and in particular its rigidity-dependence – which should be constant following its derivation. From this result the following questions:

- Can the force field approach describe the whole measured GCR proton spectra by PAMELA?
- Is the force field approach really independent of rigidity, as yielded from its derivation?
- And if not, what are the consequences?

Two other analyses are covered in this work, which were done before PAMELA or AMS-02 results were available: A study of Recurrent Cosmic Ray Decreases (RCRDs) in the time period 2007-2008 (Chap. 2), and an investigation of charge-sign dependence during the unusual solar minimum 2007-2009 (Chap. 4). Future studies re-investigating these topics using the newer observations would be worthwhile, and could build upon the here presented works.

2

SHORT-TERM GCR MODULATION

There are different time scales of GCR modulation, as already introduced in Sect. 1.3. The variation with a periodicity of 11 and 22 years, respectively, which is connected to the cycle of solar activity, is the most intense and prominent one. However, it is only known since long-term observations by neutron monitors, starting in the 1950s. Historically, after the discovery of GCRs, first diurnal and later singular as well as recurrent decreases with time scales of around 27 days were observed (Compton and Getting, 1935; Forbush, 1937; Hess and Demmelmair, 1937). Simpson (1954) located the cause of the later findings to processes in the interplanetary medium, with the 27-day periodicity originating in the synodic rotation of the Sun. The understanding is that CMEs, huge releases of plasma and magnetic fields from the Sun's corona that are connected to solar activity, can cause the singular and sudden Forbush decreases (see review by Cane, 2000). On the other hand, the recurrent decreases of GCRs are accounted to CIRs. These structures of compressed plasma emerge when a region of fast solar wind catches up with a slow wind region (see Richardson, 2004, for a review). In both cases the idea is that the CIR or CME change the propagation conditions, hindering the transport of GCRs to the inner heliosphere. The modulation effects caused by this are usually of the order of 1-5% (Richardson, 2004). Since CIRs are usually stable over several solar rotations, they cause a recurrent decrease of GCRs with the same periodicity as the solar rotation, that is, approximately 27 days at Earth. This effects all kind of charged particles propagating through the heliosphere, and can also be observed in Jovian electrons. These electrons are accelerated at Jupiter's magnetosphere (Teegarden et al., 1974) and represent the main part of electrons in the heliosphere between 5–30 MeV during solar quite times (Chenette, 1980).

In the following proceeding (Gieseler et al., 2009), a one-year period of such a recurrent decrease of GCRs and Jovian electrons is investigated in 2007–2008. While the electrons were detected as intended by the Electron Proton Helium Instrument (EPHIN) onboard the Solar and Heliospheric Observatory (SOHO), for the GCRs the guard counter surrounding this instrument was used. The resulting count rates are expected to reflect the temporal variation of about 1 GV GCRs during solar quiet times (e.g. Richardson, 2004). Particular emphasis was drawn to the investigation of differences in the modulation of GCRs compared to that of Jovian electrons. In the beginning of the observation period, the recurrent decreases of both of them are in phase, but later an offset evolves, leading to a phase difference of almost 180°. This could be explained by the fact that Jupiter acts as a point source for the Jovian electrons, while the GCRs distribution is almost isotropic. Because of that the relative longitudinal positions of Earth and Jupiter play an important role in the modulation of Jovian electrons. This analysis has later been carried out in more detail in Kühl et al. (2013).

Recurrent modulation of galactic cosmic rays: A comparative study between IMP, SOHO, STEREO, and Ulysses

Gieseler, J., N. Dresing, P. Dunzlaf, R. Gómez-Herrero, B. Heber, A. Klassen, A. Kopp, R. Müller-Mellin, M. S. Potgieter, and S. E. S. Ferreira, *Proc. 31st Internat. Cosmic Ray Conf. (Lodz, Poland)* (2009) Own contribution: 90%

Recurrent modulation of galactic cosmic rays: A comparative study between IMP, SOHO, STEREO, and Ulysses

J. Gieseler*, N. Dresing*, P. Dunzlaff*, R. Gómez-Herrero*, B. Heber*, A. Klassen*, A. Kopp*, R. Müller-Mellin*, M.S. Potgieter† and S.E.S. Ferreira†

* *Institut für Experimentelle und Angewandte Physik, Christian-Albrechts-Universität zu Kiel, Germany*
† *Unit for Space Physics, North-West University, Potchefstroom, South Africa*
Contact: gieseler@physik.uni-kiel.de

Abstract. **It is well known that the galactic cosmic ray (GCR) flux is modulated by corotating interaction regions (CIR) in the vicinity of Earth. When Ulysses first explored high latitude regions in 1996, it was found that the flux of GCRs was still modulated on the time scale of one solar rotation, although neither the solar wind nor the interplanetary magnetic field at these latitudes showed the characteristics of CIRs. This finding led to the modification of our understanding of either the heliospheric magnetic field (HMF, Fisk field) or the transport of particles perpendicular to the HMF. Now, 12 years later, Ulysses explored these high latitude regions again. From September 2007 to September 2008, the GCR flux at Earth showed a clear 27 day solar-rotation modulation. In this contribution, we show that the intensities of GCRs and Jovian electrons at the location of Earth are well modulated with the expected time periods of 27 and 26 days, respectively.**

Keywords**: corotating interaction regions - galactic cosmic rays - jovian electrons**

I. INTRODUCTION

Since 30 years, it is known that corotating interaction regions have a noticeable effect on the propagation of cosmic rays in the heliosphere, as first described in detail by Barnes and Simpson [1]. However, until today not all details in this mechanism are clearly understood. The time interval from September 2007 to September 2008 during the current, very quiet solar minimum delivers a pronounced example of such a CIR-induced recurrent cosmic ray decrease (RCRD) with solar rotation (cf. Fig. 1). Not only cosmic rays, however, can be affected by CIRs. Jovian electrons, the main population of MeV electrons in the inner heliosphere [14], undergo modulation by CIRs as well [2][3]. Both effects could be seen on different spacecraft in the time interval chosen.

II. INSTRUMENTATION

In this paper, we present first results of the investigation of this modulation period, using data from the Electron Proton Helium Instrument (EPHIN) [10] onboard the SOHO spacecraft at the Lagrange point L1 near Earth. The instrument measures electrons in the energy range from 250 keV to above 13 MeV and protons and

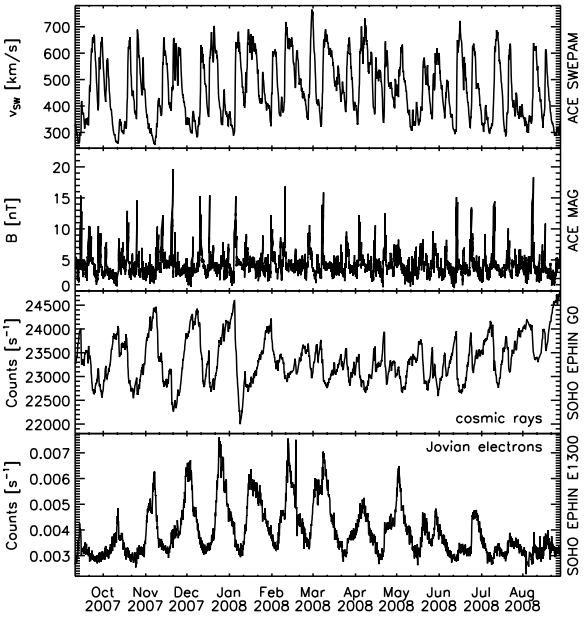

Fig. 1: 4-hours averaged solar wind speed and 1-hour averaged magnetic field strength measured by ACE, and 4-hours averaged counting rates of all particles detected (mainly cosmic rays) and 2.64-6.18 MeV electrons measured by SOHO *(from top to bottom)*.

helium in the energy range from 4 MeV/n to above 50 MeV/n. The telescope is surrounded by a plastic scintillation detector, called G0 in what follows. During quiet times, as investigated in this paper, this detector reflects mainly the temporal variation of galactic cosmic rays with a mean rigidity of about 1 GV [11]. In order to determine the temporal variation of Jovian electrons, we used the EPHIN E1300 channel, which is sensitive to electrons in the energy range from 2.64 to 6.18 MeV. Solar wind speed observations were made with the Solar Wind Electron Proton Alpha Monitor (SWEPAM) [9], magnetic field measurement were performed by the MAG instrument [13], both onboard the Advanced Composition Explorer (ACE), which is situated at L1 as well. In addition, Carrington maps provided by the Global Oscillation Network Group (GONG) are used to correlate coronal holes and observed fast wind streams.

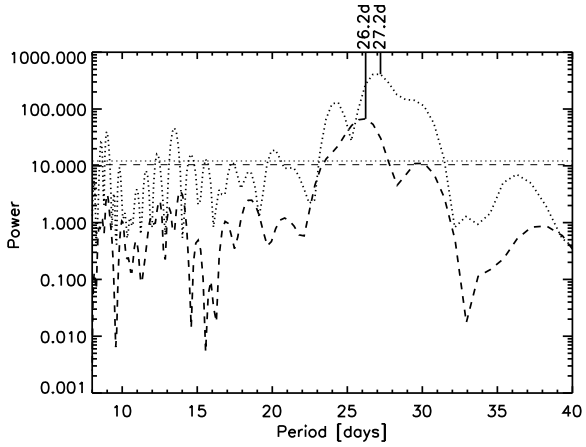

Fig. 2: Lomb periodograms for EPHIN G0 *(dotted curve)* and E1300 *(dashed curve)* for the whole time period. The horizontal lines each mark the significance level of 99%.

III. Observations

Fig. 1 displays together with the solar wind speed and the magnetic field strength the counting rates of cosmic rays (G0) and Jovian electrons (E1300), which show recurrent modulation with a period close to the rotation period of the Sun. Since Jupiter and Earth are magnetically well connected every 13 months, the intensities of Jovian electrons show in contrast to GCRs a maximum in the beginning of 2008. From Fig. 1 it is evident that the amplitude of recurrent GCR decreases is becoming smaller in 2008 while MeV electrons continue to be modulated with no major difference. In order to investigate the count rate periodicities in more detail, we applied a Lomb spectral analysis [8], as described in [5][7]. The results are shown in Fig. 2. Frequencies with powers above the corresponding horizontal line are significant on a level of 99%. While galactic cosmic rays are modulated with a period of 27.2 days, MeV electrons have a somehow shorter period of 26.2 days. In order to discuss this difference, we show in Fig. 4 and Fig. 5 the detrended counting rate variation of G0 and the E1300 counting rate together with the solar wind speed and magnetic field strength backmapped to the solar surface, as described in [4]. The detrended counting rate variation $\Delta C/C$ is calculated by using the 4-hours averaged count rates $(C(t))$ and one solar rotation averaged running means $(S(t))$:

$$\Delta C/C = (C(t) - S(t))/S(t)$$

For the purpose of comparing the in-situ data with the coronal structures, the synoptic maps from GONG are displayed on top. Stream interfaces of CIRs, which can be identified by characteristic changes of the solar wind speed and the magnetic field strength [12], are marked by dashed horizontal lines.

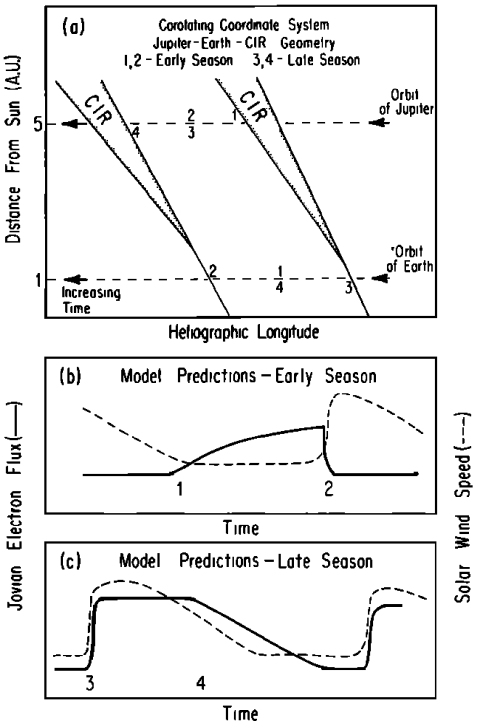

Fig. 3: Illustration of the mechanism producing the solar rotational modulation of Jovian electrons in the vicinity of the Earth (taken from [2]). *(a)* Schematic plotted are radius vs. longitude of Jovian and Earth orbit as well as two CIRs in a corotating coordinate system fixed to the Sun. The numerals 1-4 indicate different time positions of the planets, while the CIRs are fixed. *(b,c)* Model predictions of Jovian electron flux *(solid line)* and solar wind speed *(dashed line)* for early and late in a Jovian electron season at Earth, respectively.

IV. Discussion and Summary

An analysis of Fig. 4 shows that while the count rates of G0 and E1300 appear to be in phase during Carrington rotation (CR) 2061 to 2065, an offset evolves afterwards, leading to a phase difference of $\sim 180^\circ$ in CR 2066. Furthermore, in the first half of our observation period there is a significant drop in the cosmic ray intensities almost every 27 days, which occurs near the time of a stream interface, while the correlation of the electron intensity with the occurrence of the CIR is not straightforward. The reason for this is that Jupiter can be treated here as a point source and Jovian electrons are propagating mainly along field lines to reach the SOHO spacecraft [6]. Fig. 3 from [2] sketches this situation. In part *(a)* of this illustration, the numerals 1 and 2 mark two positions of Earth and Jupiter at different times in a period before the two planets are best connected along the average interplanetary magnetic field whereas 3 and 4 indicate different positions after the time of best connection. This illustrates the idea that before the time of best connection Earth enters the region

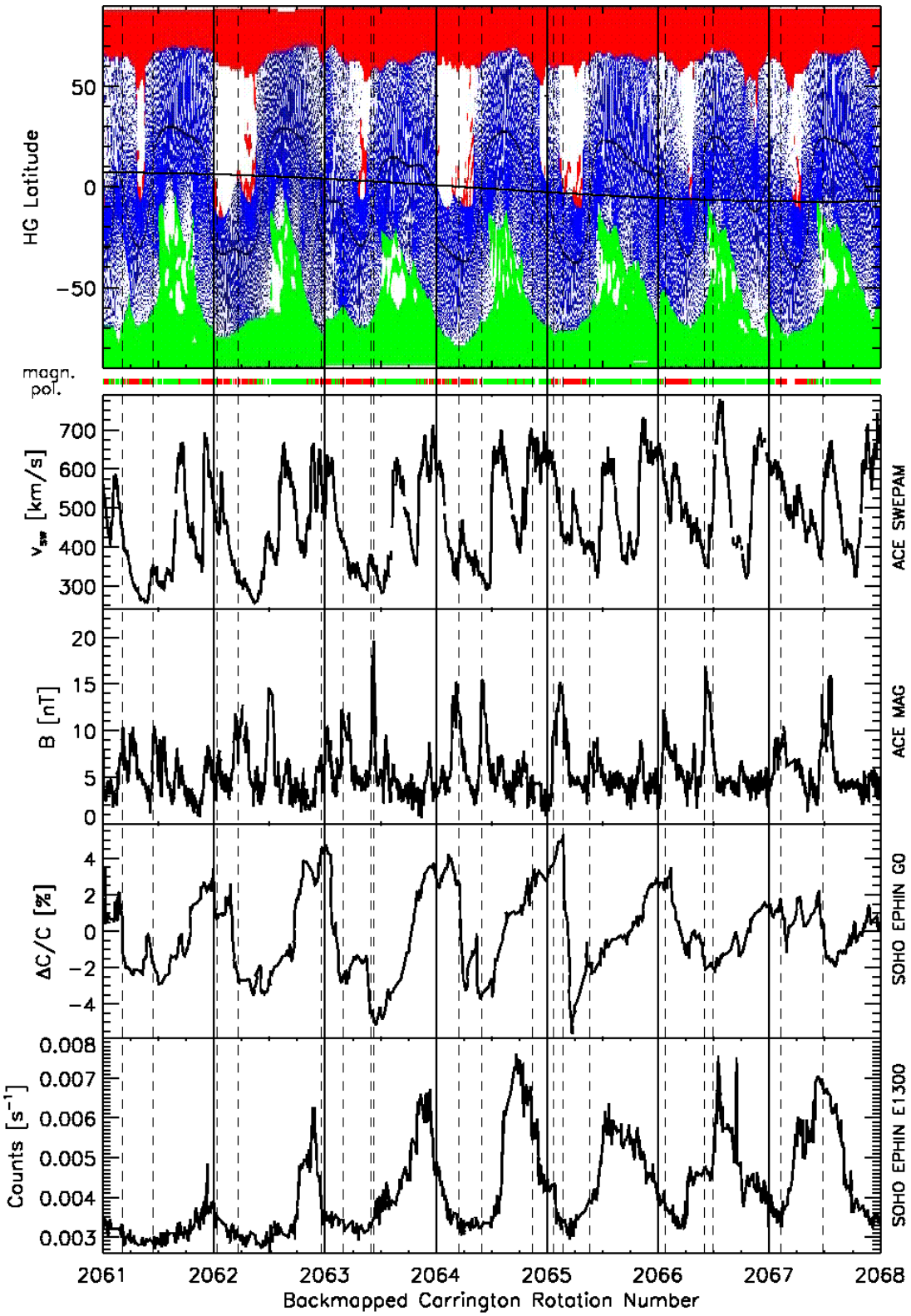

Fig. 4: Backmapped plasma and particle data for the Carrington rotations 2061 to 2067 *(from top to bottom)*: synoptic maps from GONG, magnetic polarity, 4-hours averaged solar wind speed and 1-hour averaged magnetic field strength measured by ACE, and 4-hours averaged detrended counting rate variation of all ionized particles and count rates of 2.64-6.18 MeV electrons measured by SOHO. Marked by dashed horizontal lines are stream interfaces of CIRs.

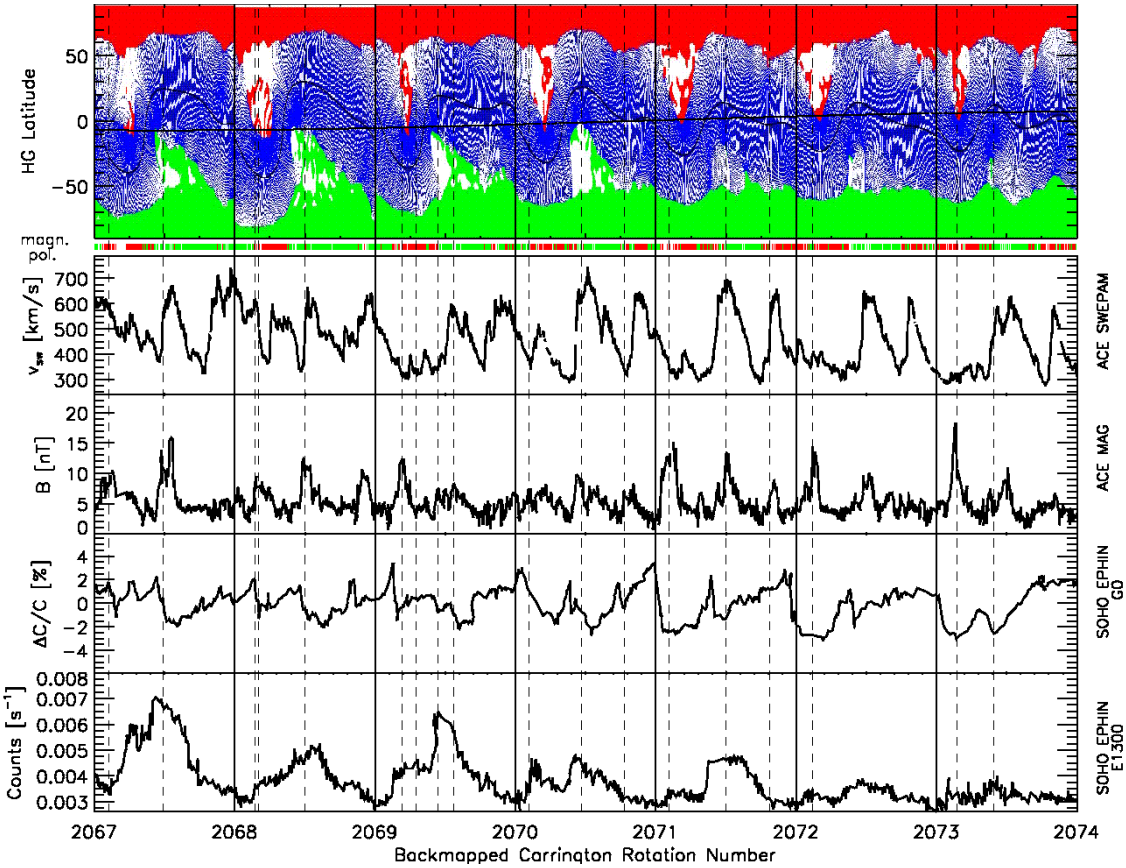

Fig. 5: Same as Fig. 4, but for Carrington rotations 2067 to 2073.

between two consecutive CIRs ahead of Jupiter while after the time of best connection the entering order is interchanged. Both times represent constellations where the field line connection between Earth and Jupiter is crossed by CIRs.

The second half of our observation period, as displayed in Fig. 5, is characterized by a smaller amplitude of the recurrent cosmic ray decrease with no obvious difference in solar wind speed and magnetic field strength time profiles. As expected, the amplitude of the MeV electrons is decreasing due to the diverging connection of Jupiter and Earth. A detailed analysis of the GONG maps shows that the extensions of the heliospheric current sheet and the coronal holes are more and more restricted to lower and higher latitudes, respectively. However, these changes do not necessarily reflect themselves in the in-situ plasma data. Because galactic cosmic rays enter the heliosphere from all directions (isotropically), these particles are affected by global changes in the configuration of the heliosphere, whereas Jovian electrons are unaffected due to their in ecliptic source.

Thus simultaneous observations of MeV electrons and GCR particles together with in-situ and remote sensing will allow us to study the importance of different propagation parameters in the future.

ACKNOWLEDGMENTS

The STEREO/SEPT and SOHO/COSTEP projects are supported under grant No. 50 OC 0105 and 50 OC 0902 by the German Bundesministerium für Wirtschaft through the Deutsches Zentrum für Luft- und Raumfahrt (DLR). MSP and SESF acknowledge the partial financial support of the SA National Research Foundation. The German - South African collaboration has been supported by the DLR under grant SUA 07/013. We thank the ACE MAG and SWEPAM instrument teams and the ACE Science Center for providing the ACE data. This work utilizes data obtained by the Global Oscillation Network Group (GONG) program, managed by the National Solar Observatory, which is operated by AURA, Inc. under a cooperative agreement with the National Science Foundation. The data were acquired by instruments operated by the Big Bear Solar Observatory, High Altitude Observatory, Learmonth Solar Observatory, Udaipur Solar Observatory, Instituto de Astrofísica de Canarias, and Cerro Tololo Interamerican Observatory.

REFERENCES

[1] Barnes, C. W., and Simpson, J. A., Astrophys. J., 207, 91, 1976.
[2] Chenette, D. L., J. Geophys. Res., 85, 2243, 1980.
[3] Conlon, T. F., J. Geophys. Res., 83, 541, 1978.
[4] Dresing, N. et al., Solar Phys., 256, 409, 2009.
[5] Dunzlaff, P. et al., Ann. Geophys., 26, 3127, 2008.
[6] Ferreira, S. E. S. et al., J. Geophys. Res., 106, 24979, 2001.
[7] Heber, B. et al., AIP Conf. Proc., Vol. 528, 357, 2000.
[8] Lomb, N. R., Astrophys. Space Sci., 39, 447, 1976.
[9] McComas, D. J. et al., Space Sci. Rev., 86, 563, 1998.
[10] Müller-Mellin, R. et al., Solar Phys., 162, 483, 1995.
[11] Richardson, I. G., Space Sci. Rev., 111, 267, 2004.
[12] Smith, E. J., and Wolfe, J. H., Reidel, 227, 1977.
[13] Smith, C. W. et al., Space Sci. Rev., 86, 613, 1998.
[14] Teegarden, B. J. et al., J. Geophys. Res., 79, 3615, 1974.

3 SPATIAL GRADIENTS OF GCRS

In order to understand the solar modulation of GCRs, it is crucial to observe and reproduce the spatial distribution of GCRs in the three-dimensional heliosphere. Parker (1965) introduced the transport equation (Eq. 1, cf. Sect. 1.3), which describes the time evolution of the differential CR phase space distribution function inside the heliosphere. During times of solar minimum conditions, when the heliosphere is not disturbed extensively by solar activity, it is a reasonable assumption to introduce a steady-state solution ($\partial f / \partial t = 0$), neglecting all short-term (shorter than one solar rotation) modulation effects (e.g. Potgieter, 2013a). This transport equation already incorporated the different physical processes influencing the GCRs: convection by the solar wind, gradient and curvature drifts in the HMF, diffusion at HMF irregularities, adiabatic energy changes, and possible local sources. But in the first years after the establishment of the Parker equation the effects of drift processes on the solar modulation were almost neglected. Until Jokipii et al. (1977) presented particle drifts as an explanation for the observed charge-sign dependent GCR modulation (see also Sects. 1.3 and 4). In the following, various numerical GCR transportation models including drift effects were established (see Burger and Visser, 2010, for an overview). From these works, drift processes are expected to be the main drivers for the GCR modulation during times of solar minimum, whereas diffusion should dominate in periods of high solar activity (e.g. Cliver et al., 2013). However, this picture was challenged by the so-called unusual solar minimum from 2006 to 2009, where in order to explain the observed record-high GCR intensities diffusion seemed to be either the primary modulation process (Cliver et al., 2013) or at least contributed to half of the modulation (with drifts being responsible for the other half, Potgieter et al., 2014). Thus, the relevance and importance of these drift processes for the solar modulation over a complete solar activity cycle has been and still is under debate.

Altogether, the following understanding of drift processes is gained. In an $A > 0$ solar cycle, when the magnetic field is pointing outwards in the northern hemisphere (see left side of Fig. 9), positively charged particles are mainly entering the inner heliosphere over the solar poles, and are drifting to lower latitudes and along the HCS outwards of the heliosphere (see also Fig. 6). The pattern is reversed during an $A < 0$ epoch (right side of Fig. 9): Here, positively charged GCRs drift in the inner heliosphere along the HCS, before they are carried outwards over the polar regions. Because of the physical nature of drift effects, particles of the opposite polarity show the opposite behavior. If the particles move inwards along the HCS, their intensity in the inner heliosphere depends on the varying tilt angle between the solar magnetic field dipole axis and its rotational axis, which determines the waviness of the HCS. A more wavy HCS leads to an elongated drift path for the particles. Thus, a larger tilt angle hinders the propagation of GCRs to the inner heliosphere. This explains the observed charge-sign dependence

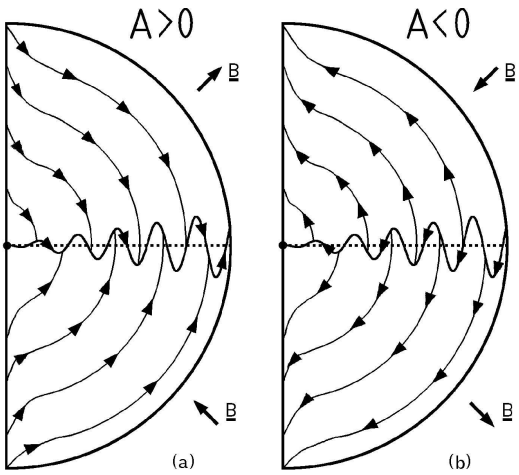

Figure 9: Illustration of the global drift pattern of positively charged GCRs in the heliosphere (side-view of the heliosphere with the wavy HCS around the ecliptic) for $A > 0$ and $A < 0$ solar cycles, respectively. Figure reproduced from Heber and Potgieter (2006, adapted from Jokipii and Thomas, 1981) by permission of Springer, ©2007.

in GCR time series (as shown in Fig. 3) with alternating peaked and plateau-like structures every 11 years. The common understanding of drift processes also predicts different kinds of spatial gradients of GCRs: In general, the radial gradient is expected to be positive, that is, the GCR intensity is increasing when moving away from the Sun towards the ISM. However, the latitudinal gradient, describing the increase of intensity with respect to heliospheric latitude, should vary depending on the charge of the respective particle and the solar magnetic epoch. It is expected that positively charged GCRs will have a large positive latitudinal gradient in an $A > 0$ magnetic epoch, when the particles drift into the inner heliosphere from high latitudes (Fig. 9, left). Whereas during $A < 0$ times a negative gradient is anticipated (Fig. 9, right). Again, the whole pattern is reversed for negatively charged particles, that is, mainly electrons.

In order to test and further improve the theoretical models, in-situ measurements at different positions in the heliosphere are indispensable. For this purpose, radial, latitudinal, and temporal variations of the measured quantities need to be disentangled. Longitudinal effects in the distribution of GCRs are in this context usually neglected by averaging the measurements over time periods of at least one solar rotation. Thus, all variations caused by short-term effects are canceled out. A common approach is to use simultaneous observations at a fixed position with respect to radius and latitude (most times at Earth orbit, often called "1 AU baseline") and on a moving spacecraft. Especially the Pioneer and Voyager missions are of interest for this because of the long time series and large distances they cover (e.g. Cummings et al., 1987; McKibben, 1989; McDonald et al., 1997). On the other hand, Ulysses with its highly inclined (80.2°) orbit around the Sun (see Fig. 10) is predestined to investigate the latitudinal distribution of GCRs (e.g. Heber et al., 1996a,b; Simpson et al., 1996, and the works presented in this chapter). By analyzing the ratio of the intensities concurrently measured at different locations, temporal variations are canceled out, leaving only the changes

due to spatial effects. Afterwards, these variations caused by observations at different radius and latitude can be disentangled. This well-established approach (e.g. McKibben et al., 1979; Cummings et al., 1987) to simultaneously calculate the radial and latitudinal gradients is presented in Sects. 3.2.3, 3.3.3 and 3.4.3. The gradients derived from such multi-point observations usually cover large regions in the heliosphere, that is, they describe a global structure. Therefore, they are sometimes called global gradients, especially when compared with theoretical calculations. Numerical models can calculate the intensities at any position in the heliosphere, which yield so-called local gradients. For better comparison, Vos and Potgieter (2016) performed numerical simulations and derived the global gradients in the same manner as presented in Sect. 3.4 of this work.

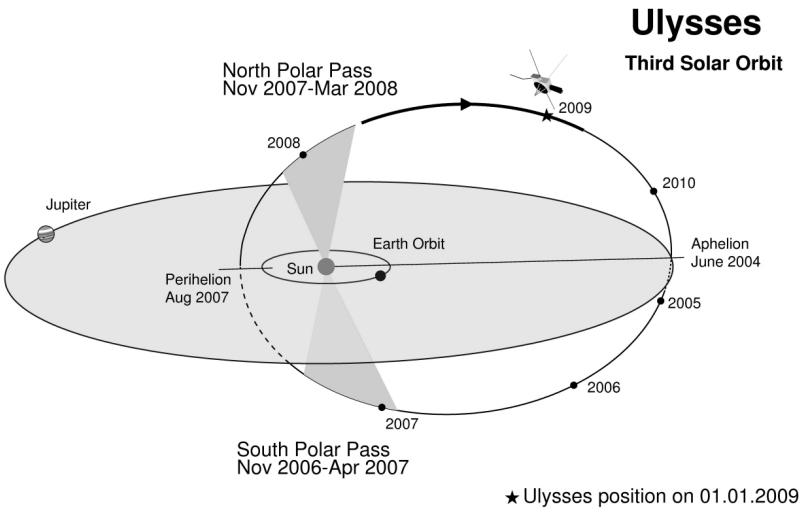

Figure 10: Sketch of Ulysses's third and last solar orbit. Figure ©2008 ESA, reproduced from http://sci.esa.int/jump.cfm?oid=41770.

The principal trend of the expectations from Fig. 9 was confirmed by measurements of the KET onboard Ulysses during the 1990s $A > 0$ solar minimum (Heber et al., 1996a,b; Simpson et al., 1996), yielding positive latitudinal gradients for protons. However, they were much smaller than expected, and they showed an unanticipated rigidity dependence below 1 GV (cf. Fig. 8 in Heber et al., 1996a). The following presented publications calculate the global radial and latitudinal gradients in the following 2000s $A < 0$ solar minimum. Because the "1 AU baseline" IMP-8 used in the previous studies involving Ulysses/KET observations was not available any more, different approaches were pursued. In Sect. 3.1 same-rigidity helium and carbon measurements from Ulysses/KET and ACE/CRIS, respectively, are compared (Heber et al., 2008). In addition, the latitudinal gradients for electrons are estimated using the electron-to-proton ratio. With the availability of the PAMELA proton measurements from 2006 to 2010, these are used as baseline together with Ulysses/KET proton observations up to its mission end in 2009 for different energy ranges, see Sects. 3.2, 3.3 and 3.4 (De Simone et al., 2011; Gieseler et al., 2013; Gieseler and Heber, 2016). The main

findings of all these publications are summarized in Fig. 11, presenting the calculated latitudinal gradients with respect to particle rigidity. Additionally shown are computed model latitudinal gradients for protons during the 1990s $A > 0$ solar minimum based on Ulysses/KET measurements (blue dashed line), and a simulation prediction for the 2000s $A < 0$ solar minimum investigated here (red dashed line) (figure adapted from Potgieter et al., 2001; more details in Burger et al., 2000). This figure demonstrates that the approach to compare same-rigidity helium and carbon measurements used in Heber et al. (2008, green data point) due to the limited availability of observations yields indeed comparable results as found in later investigations using proton measurements. All findings for positively charged particles are in agreement with each other, with small deviations that can be ascribed to changes in the analysis process and slightly updated data sets. The global trend of small negative, nonzero latitudinal gradients below 3 GV predicted by model simulations from Potgieter et al. (2001, red dashed line) is confirmed. However, the calculated values between 1 and 2 GV are smaller than expected. The derived latitudinal gradient for 2.5 GV electrons (blue data point) also shows the expected behavior, that is, it has an opposite sign and a higher value.

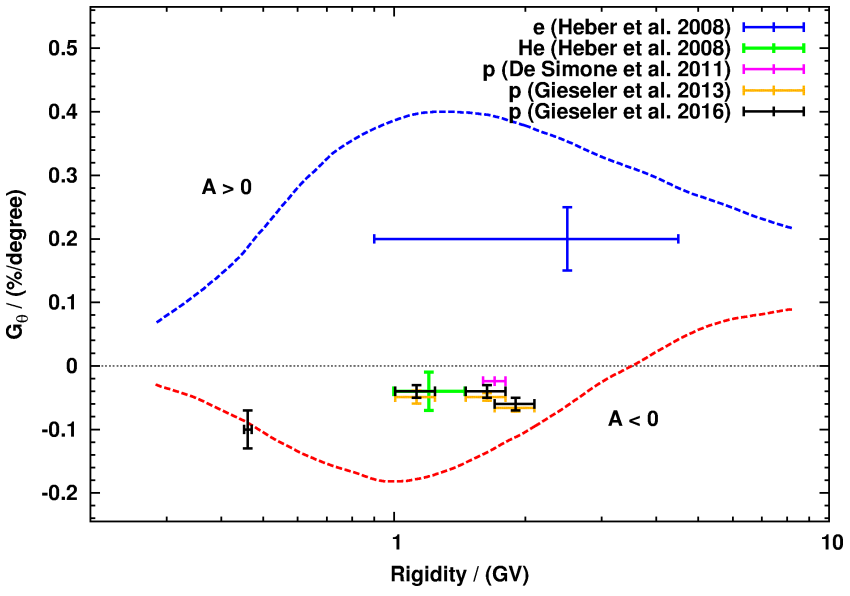

Figure 11: Results of the calculated electron, helium and proton latitudinal gradients from Sects. 3.1, 3.2, 3.3 and 3.4 with respect to rigidity. In addition, computed and predicted proton gradients for the 1990s $A > 0$ and the 2000s $A < 0$ solar minima are shown, respectively (from Potgieter et al., 2001, blue and red dashed lines).

Latitudinal gradients of galactic cosmic rays during the 2007 solar minimum

Heber, B., **J. Gieseler**, P. Dunzlaff, R. Gómez-Herrero, A. Klassen, R. Müller-Mellin, R. A. Mewaldt, M. S. Potgieter, S. E. S. Ferreira, *Astrophys. J.*, 689, 2, 1443-1447 (2008), DOI:10.1086/592596. Own contribution: 20%

Latitudinal and radial gradients of galactic cosmic ray protons in the inner heliosphere – PAMELA and Ulysses observations

De Simone, N., V. Di Felice, **J. Gieseler**, M. Boezio, M. Casolino, P. Picozza, PAMELA Collaboration, and B. Heber, *Astrophys. Space Sci. Trans.*, 7, 425-434 (2011), DOI:10.5194/astra-7-425-2011. Available under the Creative Commons Attribution 3.0 License: https://creativecommons.org/licenses/by/3.0/
Own contribution: 30%

Inner heliosphere spatial gradients of GCR protons in the low GeV range

Gieseler, J., M. Boezio, M. Casolino, N. De Simone, V. Di Felice, B. Heber, M. Martucci, P. Picozza, and the PAMELA Collaboration, *Proc. 33rd Internat. Cosmic Ray Conf. (Rio de Janeiro, Brazil)*, 341 (2013) Own contribution: 95%

Spatial gradients of GCR protons in the inner heliosphere derived from Ulysses COSPIN/KET and PAMELA measurements

Gieseler, J., and B. Heber, *Astron. Astrophys.*, 589, A32 (2016), DOI:10.1051/0004-6361/201527972. Reproduced with permission © ESO. Own contribution: 90%

The Astrophysical Journal, 689:1443–1447, 2008 December 20

LATITUDINAL GRADIENTS OF GALACTIC COSMIC RAYS DURING THE 2007 SOLAR MINIMUM

B. Heber, J. Gieseler, P. Dunzlaff, R. Gómez-Herrero, A. Klassen, and R. Müller-Mellin
Institut für Experimentelle und Angewandte Physik, Christian-Albrechts-Universität Kiel,
D-24118 Kiel, Germany; heber@physik.uni-kiel.de

R. A. Mewaldt
Space Radiation Laboratory, California Institute of Technology, Pasadena, CA 91125

and

M. S. Potgieter and S. E. S. Ferreira
Unit for Space Physics, North-West University, 2520 Potchefstroom, South Africa
Received 2008 April 8; accepted 2008 August 14

ABSTRACT

Ulysses, launched in 1990 October in the maximum phase of solar cycle 22, completed its third out-of-ecliptic orbit in 2008 February. This provides a unique opportunity to study the propagation of cosmic rays over a wide range of heliographic latitudes during different levels of solar activity and different polarities in the inner heliosphere. Comparison of the first and second fast latitude scans from 1994 to 1995 and from 2000 to 2001 confirmed the expectation of positive latitudinal gradients at solar minimum versus an isotropic Galactic cosmic ray distribution at solar maximum. During the second scan in mid-2000, the solar magnetic field reversed its global polarity. From 2007 to 2008, *Ulysses* made its third fast latitude scan during the declining phase of solar cycle 23. Therefore, the solar activity is comparable in 2007–2008 to that from 1994 to 1995, but the magnetic polarity is opposite. Thus, one would expect to compare positive with negative latitudinal gradients during these two periods for protons and electrons, respectively. In contrast, our analysis of data from the Kiel Electron Telescope aboard *Ulysses* results in no significant latitudinal gradients for protons. However, the electrons show, as expected, a positive latitudinal gradient of $\sim$0.2% per degree. Although our result is surprising, the nearly isotropic distribution of protons in 2007–2008 is consistent with an isotropic distribution of electrons from 1994 to 1995.

Subject headings: convection — cosmic rays — diffusion — solar-terrestrial relations — solar wind

Online material: color figures

1. INTRODUCTION

The ongoing *Ulysses* mission provides a unique opportunity to study the propagation and modulation of Galactic cosmic rays (GCRs) in detail by in situ measurements in the three-dimensional heliosphere. The intensity of GCRs is modulated as they traverse the turbulent magnetic field embedded in the solar wind. These particles are scattered by irregularities in the interplanetary magnetic field and undergo convection and adiabatic deceleration in the expanding solar wind. The large-scale heliospheric magnetic field, which approximates an Archimedean spiral (Parker 1965), leads to gradient and curvature drifts of cosmic rays in the interplanetary medium. Jokipii et al. (1977) pointed out that these drift effects should also be an important element of cosmic-ray modulation. Models that take such effects into account (Evenson 1998; Heber et al. 2002; Ferreira et al. 2003a; Ferreira & Potgieter 2004) predict the latitudinal distribution of GCR protons and electrons. In the 1980s, during an $A < 0$ solar magnetic epoch, i.e., when the field is directed toward the Sun in the north polar region, models predicted a negative latitudinal gradient for positively charged cosmic rays. Such gradients were found by the cosmic-ray instruments aboard the two *Voyager* satellites (Cummings et al. 1987; McDonald et al. 1997). In the 1970s and 1990s, during the $A > 0$ solar magnetic epoch, *Pioneer* and *Ulysses* measurements from 1974 to 1977 and 1994 to 1995 confirmed the expectation of positive latitudinal gradients (McKibben 1989; Heber et al. 1996b). An overview of some selected results are given in Table 1. Because the observed latitudinal gradients were much smaller than predicted by drift-dominated models (Jokipii et al. 1977), in particular at low energies, reinvestigations emphasized the importance of stochastic and systematic perpendicular transport in the heliosphere and the modification of the heliospheric magnetic field (Fisk & Jokipii 1999; Fisk 1996). It was shown that the cosmic-ray observations could be described well when such processes were included (Ferreira et al. 2003a; Ferreira & Potgieter 2004; Potgieter et al. 1997). During the second fast latitude scan in 2000–2001, no latitudinal gradients were measured (McKibben et al. 2003; Heber et al. 2002). Thus, the importance of charge sign dependence (e.g., drift) in the diffusion process varies with the solar cycle (Ferreira et al. 2003a). When *Ulysses* again reached its highest southern heliographic latitudes in 2007, solar activity was similar to the activity level in 1994, but the heliospheric magnetic field had reversed sign.

2. INSTRUMENTATION AND OBSERVATIONS

The observations were made with the Kiel Electron Telescope (KET) aboard *Ulysses* and the Cosmic Ray Isotope Spectrometer (CRIS) aboard the *Advanced Composition Explorer* (*ACE*). KET measures protons and helium in the energy range from 6 MeV to above 2 GeV per nucleon and electrons in the energy range from 3 MeV to a few GeV (Simpson et al. 1992). *Ulysses* was launched on 1990 October 6, shortly before the declining activity phase of solar cycle 22. A swing-by maneuver at Jupiter in 1992 February placed the spacecraft into a trajectory inclined by 80° with respect to the ecliptic plane.

In this paper, we compare the *Ulysses* helium 125–250 MeV nucleon^{-1} channel with the *ACE* carbon 147–198 MeV nucleon^{-1} channel. As discussed in Gieseler et al. (2007), both channels

TABLE 1
Overview of Latitudinal Gradients for Cosmic-Ray Protons and Helium Reported in the Literature

Magnetic Epoch	Energy	G_ϑ (% deg^{-1})	Reference
$A > 0$	145–255 MeV nucleon^{-1} (He)	0.21 ± 0.6	McDonald et al. 1997
	145–255 MeV nucleon^{-1} (He) at 60 AU	0.0 ± 0.4	McDonald et al. 1997
$A < 0$	145–255 MeV nucleon^{-1} (He)	-1.1 ± 0.1	McDonald et al. 1997
	140–350 MeV nucleon^{-1} (He)	-0.8 ± 0.1	Cummings et al. 1987
	130–210 MeV (H)	-0.9 ± 0.1	Cummings et al. 1987
$A > 0$	250–2000 MeV (H)	0.29 ± 0.8	Heber et al. 1996b
	250–2000 MeV nucleon^{-1} (He)	0.32 ± 0.9	Heber et al. 1996b
	>2000 MeV (H)	0.17 ± 0.02	Belov et al. 1999
	>2000 MeV nucleon^{-1} (He)	0.12 ± 0.01	Belov et al. 1999
	>70 MeV (H)	0.04 ± 0.01	McKibben 1989
	>70 MeV (H) at 5 AU	0.4 ± 0.05	McKibben 1989

sample the same mean rigidity of about 1.2 GV and therefore allow the determination of the latitudinal gradient during the fast latitude scan from 2006 to 2008. If we assume that the temporal variation and the radial gradient are the same for electrons and protons during the fast latitude scan, the electron-to-proton ratio will mainly depend on the electron latitudinal gradients.

The top panel of Figure 1 shows *Ulysses* daily averaged count rates of 38–125 MeV protons from 1990 November to 2008 February; the middle panel shows the 78 day averaged quiet-time variation of the count rate of ~1.2 GV protons (*gray line*) together with the count rates of 1.2 GV carbon at 1 AU (*thin black line*) and electrons (*thick black line*), and the bottom panel shows ~2.5 GV electrons (*black*) and protons (*gray*). The latter two are presented as percentage changes with respect to the rates C_m measured in mid-1997 at solar minimum, $[C(t) - C_m]/C_m$. Quiet-time profiles were determined by using only time periods when the 38–125 MeV proton channel showed no contribution from solar or interplanetary particles (Heber et al. 1999). The 1.2 GV carbon data represent the temporal variation in the inner heliosphere, while the 1.2 GV helium and 2.5 GV electron and proton intensities are caused by temporal and spatial variations due to *Ulysses*' trajectory.

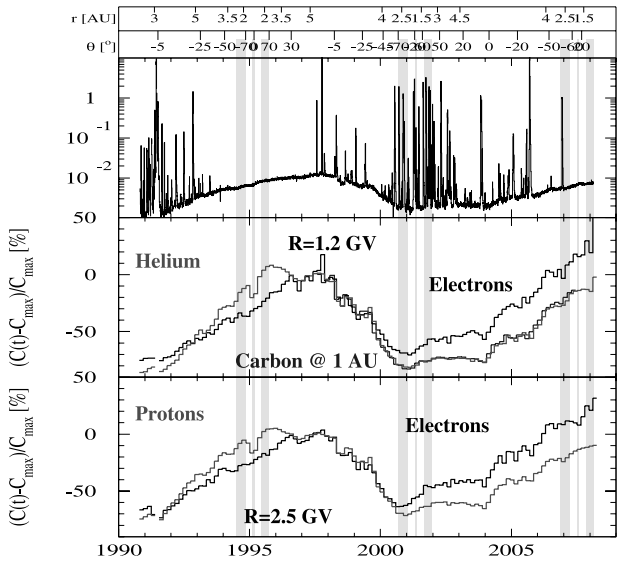

Fig. 1.—*Ulysses* daily averaged count rates of 38–125 MeV protons (*top*), 78 day averaged quiet-time variation of ~1.2 GV helium (*gray line*) compared with carbon (*thin black line*; at 1 AU) and 1.2 GV electrons (*thick black line*) (*middle*), and the ~2.5 GV electrons and protons (*bottom*) from launch in 1990 to 2008 February. *Ulysses*' distance from the Sun and its heliographic latitude are shown at the top. The three fast latitude scans are marked by shaded bands. [*See the electronic edition of the Journal for a color version of this figure.*]

While the spacecraft remained close to the ecliptic, it encountered solar maximum conditions until mid-1992, as well as from 1999 to 2004, and solar minimum conditions in 1996/1997 and from 2006 to 2008, when KET registered minimum and maximum intensities, respectively. Since electrons, as well as protons, were normalized to their maximum count rates in 1997, the middle and bottom panels of Figure 1 show the relative modulation amplitude. As expected, the amplitude decreased from about 80% for 1.2 GV particles to 65% for 2.5 GV particles. The time profiles during the 1997 solar minimum were analyzed in Heber et al. (2003) and found to be consistent with the prediction of modulation models that include drift (Ndiitwani et al. 2005).

3. DATA ANALYSIS

In order to determine the latitudinal gradient of GCRs, the temporal variation and the radial gradient in the inner heliosphere at a given rigidity have to be known. We summarize some recent results important for the current analysis:

Temporal variations.—With the loss of the *IMP* satellite in 2002, no 1 AU baseline is currently available for protons above 100 MeV. Therefore, Gieseler et al. (2007) replaced these with the 125 to 250 MeV nucleon^{-1} helium channel and found that the 147 to 198 MeV nucleon^{-1} carbon channel from the CRIS instrument aboard *ACE* (Stone et al. 1998) has nearly the same temporal variation as the *Ulysses* helium channel.

Radial gradients.—Furthermore, Gieseler et al. (2007) examined the radial intensity gradient of the 125–250 MeV nucleon^{-1} helium channel based on the measurements mentioned above. They determined a radial gradient of $G_r = 4.7\% \pm 0.6\%$ AU^{-1} for the 1998–2005 time period. This gradient is consistent with previous measurements (McDonald et al. 2003). The mean radial gradients of 1.2 and 2.5 GV electrons were found to be nearly the same as for protons during the declining phase of solar cycle 22 from 1992 to 1994 (Clem et al. 2002).

In what follows, we determine the latitudinal gradient of 1.2 GV helium and the latitudinal gradient of electrons at 2.5 GV from the electron-to-proton ratio.

3.1. *Latitudinal Gradient of* 1.2 GV *Helium*

Gieseler et al. (2007) showed that the 147–198 MeV nucleon^{-1} carbon channel of the CRIS instrument can serve as a 1 AU baseline for the 125–250 MeV nucleon^{-1} helium channel of KET

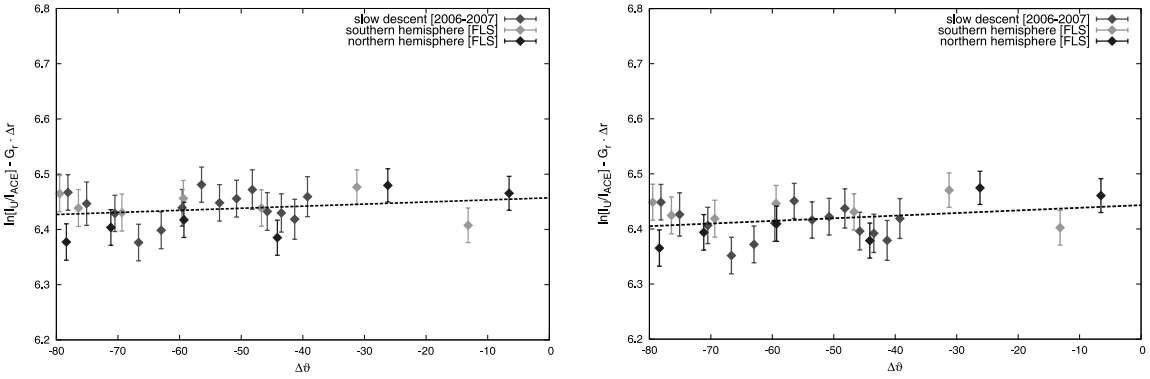

FIG. 2.—Ratio of 1.2 GV helium at *Ulysses* and 1.2 GV carbon close to Earth as a function of the latitude difference between *Ulysses* and *ACE*. Medium, light, and dark gray represent measurements during the *Ulysses* slow descend and during the fast latitude scan in the southern and northern hemisphere, respectively. *Ulysses* helium intensities have been corrected for the radial motion of the spacecraft using radial gradients of 4.1% AU^{-1} (*left*) and 5.3% AU^{-1} (*right*). [*See the electronic edition of the Journal for a color version of this figure.*]

aboard *Ulysses*. Figure 2 displays the ratio of 1.2 GV helium at *Ulysses* and 1.2 GV carbon close to Earth as a function of the latitude difference between *Ulysses* and *ACE*, $\Delta\vartheta$, assuming that the cosmic-ray distribution is symmetric around the heliographic equator. Note that we do not distinguish between northern hemisphere (*dark gray*) and southern hemisphere (*medium and light gray*) measurements. *Ulysses* helium intensities have been corrected for the radial motion of the spacecraft using radial gradients of 4.1% and 5.3% AU^{-1} as upper and lower limits on the uncertainty. It is important to note that all points are in good agreement with each other although *Ulysses* was at different locations. The lines represent the result of fitting an exponential function $I(\vartheta) = I_0 \exp(G_\vartheta \Delta\vartheta)$ to these ratios, leading to latitudinal gradients of $G_\theta = -0.04\% \pm 0.03\%$ deg^{-1} and $G_\theta = -0.05\% \pm 0.03\%$ deg^{-1}. Within the uncertainties, these gradients are consistent with zero.

This result is surprising, because a negative latitudinal gradient was expected during the *Ulysses* 2007/2008 fast latitude scan based on the *Voyager* measurements in the 1980s (Cummings et al. 1987). Although significant positive latitudinal gradients were measured during the 1994/1995 fast latitude scan for positively charged particles (Heber et al. 1996b), the analysis of Heber et al. (2003) resulted in no significant latitudinal gradients for Galactic cosmic ray electrons.

3.2. *Latitudinal Gradient of Electrons*

The determination of latitudinal gradients for electrons is less straightforward and relies on the following assumptions:

1. The radial gradients of electrons G_r^e and protons G_r^p are the same. Since the radial distance of *Ulysses* varied between 1.4 and ~2.7 AU during the fast latitude scan, a difference $G_r^e - G_r^p$ of 2% AU^{-1} would lead to an uncertainty in the latitudinal gradient of less than 0.003% deg^{-1}.
2. The temporal variations of electrons and protons are the same during the fast latitude scan. During the minimum phase of the solar cycle, the intensity time profile depends on drifts and therefore on the inclination of the heliospheric current sheet α. In the $A < 0$ solar magnetic epoch, the time profile of Galactic cosmic ray protons increases with decreasing α, while the electron intensity stays nearly constant. The Stanford group reports values between 29.4° and 33.5° using their classical line-of-sight model during the fast latitude scan.[1] Although α was constant in 2007, both time profiles of 1.2 GV electrons and protons show strong temporal variation. At slightly higher energies (2.5 GV), as displayed in the bottom panel of Figure 1 and in the top panel of Figure 3, the temporal variations are smaller. While no significant variation with latitude is observed for the 2.5 GV protons, the 2.5 GV electrons exhibit a V-shaped time profile.
3. The latitudinal gradient of 2.5 GV protons is consistent with zero. This assumption is motivated by the fact that the latitudinal gradient of 1.2 GV helium is consistent with zero and that gradients at 1.2 GV were more significant than at 2.5 GV (Cummings et al. 1987; Heber et al. 1996b).

With these assumptions, the latitudinal gradient of electrons can be estimated from the electron-to-proton ratio during the fast latitude scans around solar minimum. A latitudinal gradient of electrons should manifest itself in the electron-to-proton ratio by a V-shaped profile when the spacecraft moves from high southern to high northern latitudes (Ferreira et al. 2003b). Figure 3

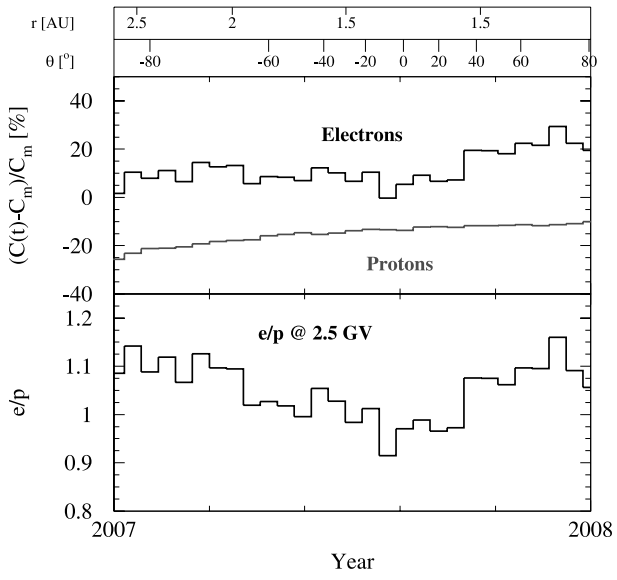

FIG. 3.—The 13 day quiet-time averages of ~2.5 GV electrons and protons (*top*) and the *e*/*p* ratio (*bottom*) in 2007. The *e*/*p* ratio is higher at polar latitudes than in the ecliptic, indicating a positive latitudinal gradient of ~2.5 GV electrons. *Ulysses*' distance from the Sun and its heliographic latitude are shown at the top. [*See the electronic edition of the Journal for a color version of this figure.*]

[1] See http://wso.stanford.edu/Tilts.html.

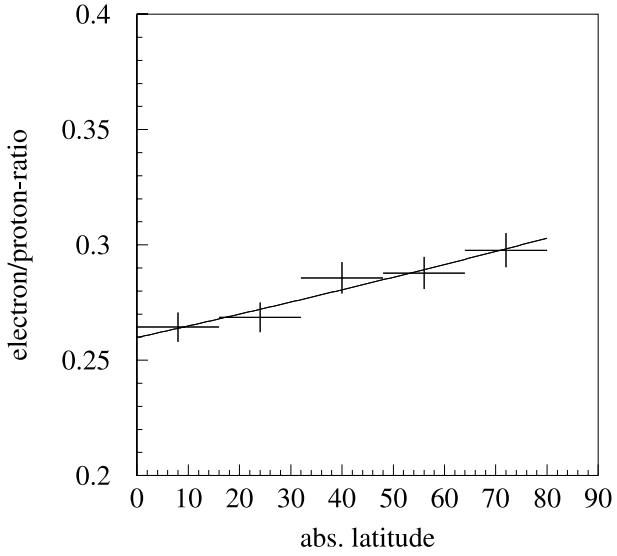

FIG. 4.—The 26 day averaged *e*/*p* ratio as a function of *Ulysses*-to-Earth latitude difference $\Delta\vartheta$, as explained in the text. The line through the data displays the fit of an exponential function with $G_\vartheta = 0.2\% \pm 0.05\%\ \mathrm{deg}^{-1}$.

displays the 13 day averaged quiet-time variation of 2.5 GV electrons and protons (*top*) and the *e*/*p* ratio (*bottom*) for 2007. The latter is lower in mid-2007, when *Ulysses* was at lower latitudes, than in early 2007 and late 2007, when the spacecraft was at southern and northern polar latitudes, confirming our expectation of a positive latitudinal gradient of electrons.

In order to determine this gradient, Figure 4 shows the *e*/*p* ratio as a function of the latitude difference, $\Delta\vartheta$, between *Ulysses* and Earth, calculated as

$$\Delta\vartheta = \left|\left|\vartheta^U\right| - \left|\vartheta^A\right|\right| \quad (1)$$

with ϑ^U and ϑ^A the latitudes of *Ulysses* and *ACE*, respectively. Thus we assume that the Galactic cosmic ray electron distribution is symmetric around the heliographic equator. In contrast to Heber et al. (1996a) and Simpson et al. (1996), the data do not us allow to investigate the north-south asymmetry found during the first fast latitude scan. In order to achieve reasonable statistical accuracy, the data in Figure 4 are binned by 15°. The solid line displays the result of a fit of the form

$$\frac{e}{p}(\Delta\vartheta) = \frac{e}{p}\exp\left(G_\vartheta \Delta\vartheta\right), \quad (2)$$

resulting in a latitudinal gradient of $G_\vartheta = 0.2\% \pm 0.05\%\ \mathrm{deg}^{-1}$ for electrons. Heber et al. (1996b) found a latitudinal gradient G_ϑ of $0.29\% \pm 0.08\%\ \mathrm{deg}^{-1}$ for 2.5 GV protons during the first fast latitude scan. Thus, the electron gradients found during the third fast latitude scan are consistent with the small gradients of protons during the first scan.

4. SUMMARY AND CONCLUSION

The large-scale heliospheric magnetic field causes gradient and curvature and current sheet drifts. When the field is directed outward from the Sun in the north polar region ($A > 0$) as in the 1990s, drift models predict that positively charged particles drift predominantly inward through the solar polar regions and then outward through the equatorial regions along the heliospheric current sheet. In contrast, electrons drift mainly into the inner heliosphere along the heliospheric current sheet and then outward through the polar regions. The vanishing and small positive latitudinal gradients for electrons and protons during the 1997 solar minimum can be understood in terms of modulation models that take into account larger perpendicular diffusion to the mean heliospheric magnetic field than previously expected. After solar magnetic field reversal, these patterns reverse. Therefore we investigated the GCR latitudinal gradients obtained in *Ulysses*' fast latitude scan during 2007. If we correct the 1.2 GV helium data with a radial gradient of $G_r = 4.7\% \pm 0.6\%\ \mathrm{AU}^{-1}$ for *Ulysses*' radial variation, we obtain a latitudinal gradient $G_\vartheta = -0.04\% \pm 0.03\%\ \mathrm{deg}^{-1}$. These values are in agreement with the vanishing gradient of electrons during the $A > 0$ solar magnetic epoch.

The determination of the electron gradient is less straightforward and relies on the assumption that the radial gradient and temporal variation of electrons and protons are nearly the same in 2007. In 2007, the temporal recovery of 1.2 GV particles was still much larger than the latitudinal variation, so we used the 2.5 GV electrons and protons instead. Our analysis results in a latitudinal gradient $G_\vartheta = 0.2\% \pm 0.05\%\ \mathrm{deg}^{-1}$ for electrons. Although the uncertainty is quite large, we can for the first time determine the latitudinal distribution of Galactic cosmic ray electrons during an $A < 0$ solar magnetic epoch. Our result is consistent with that for GCR protons in the 1990s during the $A > 0$ solar magnetic epoch. Since these gradients are much smaller than would be predicted without an enhanced perpendicular transport, we conclude that the cause of such an enhancement is present in the $A > 0$ and $A < 0$ solar magnetic epochs. Since there are two competing models to explain such particle transport, our results might help to distinguish between these numerical particle transport models.

The *Ulysses*/KET project is supported under grant 50 OC 0105 by the German Bundesministerium für Wirtschaft through the Deutsches Zentrum für Luft- und Raumfahrt (DLR). The work at Caltech was supported by NASA grant NAG 5-12929. M. S. P. and S. E. S. F. acknowledge partial financial support from the South African National Research Foundation and Centre for High Performance Computing.

REFERENCES

Belov, A. V., et al. 1999, Adv. Space Res., 23, 443
Clem, J., Evenson, P., & Heber, B. 2002, Geophys. Res. Lett., 29(23), No. 2096
Cummings, A. C., Stone, E. C., & Webber, W. R. 1987, Geophys. Res. Lett., 14, 174
Evenson, P. 1998, Space Sci. Rev., 83, 63
Ferreira, S. E. S., & Potgieter, M. S. 2004, ApJ, 603, 744
Ferreira, S. E. S., Potgieter, M. S., & Heber, B. 2003a, Adv. Space Res., 32, 645
Ferreira, S. E. S., Potgieter, M. S., Heber, B., & Fichtner, H. 2003b, Ann. Geophys., 21, 1359
Fisk, L. A. 1996, J. Geophys. Res., 101, 15547
Fisk, L. A., & Jokipii, J. R. 1999, Space Sci. Rev., 89, 115
Gieseler, J., Heber, B., & Müller-Mellin, R. 2007, Proc. 30th Int. Cosmic-Ray Conf. (Mérida), http://dpnc.unige.ch/ams/ICRC-07/icrc0354.pdf
Heber, B., Clem, J. M., Müller-Mellin, R., Kunow, H., Ferreira, S. E. S., & Potgieter, M. S. 2003, Geophys. Res. Lett., 30(19), No. 8032
Heber, B., Dröge, W., Kunow, H., Müller-Mellin, R., Wibberenz, G., Ferrando, P., Raviart, A., & Paizis, C. 1996a, Geophys. Res. Lett., 23, 1513
Heber, B., et al. 1996b, A&A, 316, 538
———. 1999, Geophys. Res. Lett., 26, 2133
———. 2002, J. Geophys. Res., 107(A10), No. 1274
Jokipii, J. R., Levy, E. H., & Hubbard, W. B. 1977, ApJ, 213, 861
McDonald, F. B., Fujii, Z., Heikkila, B., & Lal, N. 2003, Adv. Space Res., 32, 633
McDonald, F. B., et al. 1997, J. Geophys. Res., 102, 4643

McKibben, R. B. 1989, J. Geophys. Res., 94, 17021
McKibben, R. B., et al. 2003, Ann. Geophys., 21, 1217
Ndiitwani, D. C., Ferreira, S. E. S., Potgieter, M. S., & Heber, B. 2005, Ann. Geophys., 23, 1061
Parker, E. N. 1965, Planet. Space Sci., 13, 9
Potgieter, M., Haasbroek, L., Ferrando, P., & Heber, B. 1997, Adv. Space Res., 19, 917
Simpson, J. A., Zhang, M., & Bame, S. 1996, ApJ, 465, L69
Simpson, J. A., et al. 1992, A&AS, 92, 365
Stone, E. C., et al. 1998, Space Sci. Rev., 86, 285

Astrophys. Space Sci. Trans., 7, 425–434, 2011
www.astrophys-space-sci-trans.net/7/425/2011/
doi:10.5194/astra-7-425-2011

ASTRA
Astrophysics and Space Sciences Transactions

Latitudinal and radial gradients of galactic cosmic ray protons in the inner heliosphere – PAMELA and Ulysses observations

N. De Simone[1], V. Di Felice[1], J. Gieseler[3], M. Boezio[2], M. Casolino[1], P. Picozza[1], PAMELA Collaboration[†] , and B. Heber[3]

[1]INFN, Structure of Rome "Tor Vergata" and Physics Department of University of Rome "Tor Vergata", Via della Ricerca Scientifica 1, I-00133 Rome, Italy
[2]INFN, Structure of Trieste and Physics Department of University of Trieste, I-34147 Trieste, Italy
[3]Inst. für Experimentelle und Angewandte Physik, Christian-Albrechts-Universität Kiel, Leibnizstr. 11, 24118 Kiel, Germany

Received: 15 November 2010 – Revised: 7 March 2011 – Accepted: 13 April 2011 – Published: 22 September 2011

Abstract. Ulysses, launched on 6 October 1990, was placed in an elliptical, high inclined (80.2°) orbit around the Sun, and was switched off in June 2009. It has been the only spacecraft exploring high-latitude regions of the inner heliosphere. The Kiel Electron Telescope (KET) aboard Ulysses measures electrons from 3 MeV to a few GeV and protons and helium in the energy range from 6 MeV/nucleon to above 2 GeV/nucleon. The PAMELA (Payload for Antimatter Matter Exploration and Light-nuclei Astrophysics) space borne experiment was launched on 15 June 2006 and is continuously collecting data since then. The apparatus measures electrons, positrons, protons, anti-protons and heavier nuclei from about 100 MeV to several hundreds of GeV. Thus the combination of Ulysses and PAMELA measurements is ideally suited to determine the spatial gradients during the extended minimum of solar cycle 23. For protons in the rigidity interval $1.6 - 1.8$ GV we find a radial gradient of 2.7%/AU and a latitudinal gradient of -0.024%/degree. Although the latitudinal gradient is as expected negative, its value is much smaller than predicted by current particle propagation models. This result is of relevance for the study of propagation parameters in the inner heliosphere.

1 Introduction

Energetic charged particles propagating in the heliosphere are scattered by irregularities in the heliospheric magnetic field, undergo gradient and curvature drifts, convection and adiabatic deceleration in the expanding solar wind. As pointed out by Jokipii et al. (1977) these drift effects should also be an important element of cosmic ray modulation. Models taking these effects into account (Potgieter et al., 2001) predict the latitudinal distribution of galactic cosmic ray (GCR) protons and electrons. In the 1980s and in the 2000s, during an $A < 0$-solar magnetic epoch, a negative latitudinal gradient for positively charged cosmic rays is predicted. Such gradients were found by the cosmic ray instruments aboard the two Voyagers (Cummings et al., 1987; McDonald et al., 1997a). In the 1970s and 1990s, during an $A < 0$-solar magnetic epoch, Pioneer and Ulysses measurements in 1974 to 1977 and 1994 to 1995 confirmed the expectation of positive latitudinal gradients (McKibben, 1989; Heber et al., 1996a). In particular, Ulysses measurements during the previous solar minimum have been reported by Heber et al. (1996b) and Heber et al. (1999) using the measurements of the IMP 8 spacecraft as a baseline close to Earth.

In this work the data comparison with PAMELA has been carried out in the period of overlap of the two missions, between July 2006 and July 2009. Because the solar activity changes the GCR intensity in a rigidity dependent way, it is important to compare data samples at the same rigidity. Therefore, after a brief description of the two instruments in Sect. 2, we will use two different methods in Sect. 3 to define the most suitable rigidity range for comparison and we will then calculate the corresponding gradients.

2 Instrumentation

The observations presented here were made with the Cosmic and Solar Particle Investigation (COSPIN) Kiel Electron

Correspondence to: N. De Simone
(desimone@roma2.infn.it)

Published by Copernicus Publications on behalf of the Arbeitsgemeinschaft Extraterrestrische Forschung e.V.

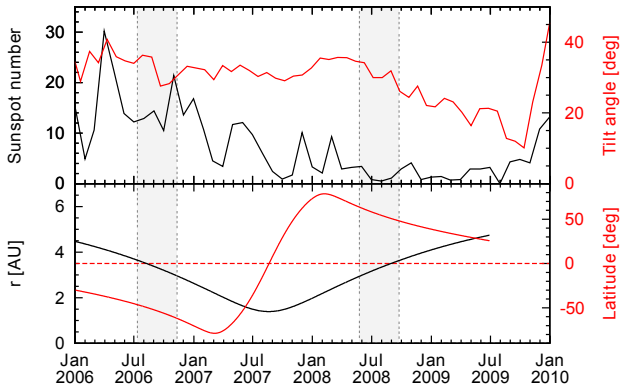

Fig. 1: As a function of time: tilt angle and sunspot number (upper panel), KET heliocentric latitude and radial distance (lower panel). Marked by shading are the comparison intervals used to investigate the temporal variation (see Sect. 3.1).

Telescope (KET) aboard Ulysses (Simpson et al., 1992) between 1.4 and 5 AU and PAMELA apparatus (Picozza et al., 2007) in low Earth orbit.

2.1 The out-of-ecliptic Ulysses mission

The main scientific goal of the joint ESA-NASA Ulysses deep-space mission was to make the first-ever measurements of the unexplored region of space above the solar poles. The GCR intensity measured along the Ulysses orbit results from a combination of temporal and spatial variations. Ulysses was launched first towards Jupiter. Following the fly-by of Jupiter in February 1992, the spacecraft has been traveling in an elliptical, Sun-focused orbit inclined at 80.2 degrees to the solar equator. The characteristics of the Ulysses trajectory after January 2006, during the declining phase of solar cycle 23, are displayed in the lower panel of Fig. 1. The upper panel of that figure shows the sunspot number (black curve) and tilt angle (red curve), respectively, indicating a period of several years of very low solar activity. Marked by shading are two periods after the launch of the PAMELA spacecraft in October 2006 and July 2008 when Ulysses was at about 3.5 AU and 50°. The polar passes are defined to be those periods during which the spacecraft is above 70 degrees heliographic latitude in either hemisphere. Beginning of 2007, the spacecraft reached a maximum southern latitude of 80°at a distance of 2.3 AU. The spacecraft then performed a whole latitude scan of 160°within 11 months. On 30 June 2009, at the minimum of the solar cycle, Ulysses was switched off on its way returning towards the heliographic equator at a radial distance of 5.3 AU.

2.2 Ulysses Kiel electron telescope

The KET measures protons and α-particles in the energy range from 6 MeV/n to above 2 GeV/n, and electrons in the

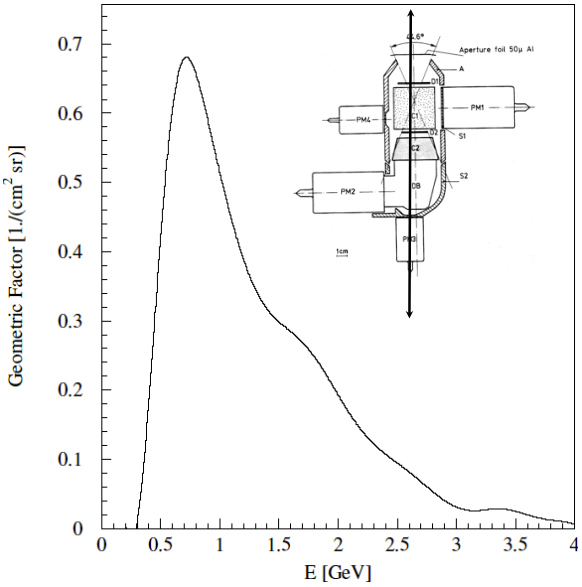

Fig. 2: Energy dependent geometric factor of one of the KET proton channels (Gieseler et al., 2010). The inset shows a sketch of the KET (from Simpson et al., 1992).

energy range from 3 MeV to some GeV. For a complete description of the KET instrument see Simpson et al. (1992). Using a GEANT-3 simulation of the Kiel Electron Telescope (Gieseler et al., 2010), its geometrical factor for different energy ranges can be determined. As an example, the energy dependent response of the channel between 500 MeV and 1400 MeV is displayed in Fig. 2 (the inset displays a sketch of the sensor). It is important to note that in the energy range of interest both forward and backward penetrating particles contribute to the measurements.

2.3 The PAMELA detector

PAMELA is designed to perform high-precision spectral measurement of charged particles of galactic, heliospheric and trapped origin over a wide energy.

PAMELA was mounted on the Resurs DK1 satellite launched on an elliptical and semi-polar orbit, with an altitude varying between 350 km and 600 km, at an inclination of 70°. At high latitudes, the low geomagnetic cutoff allows low-energy particles (down to 50 MeV) to be detected and studied.

The apparatus comprises a number of high performance detectors, capable of identifying particles through the determination of charge (Z), rigidity ($R = pc/|Z|e$, p being the momentum of a particle of charge $Z \cdot e$) and velocity ($\beta = v/c$) over a wide energy range. The device is built around a permanent magnet with a six-plane double-sided silicon micro-strip tracker, providing absolute charge information and track-deflection ($\eta = \pm 1/R$, with the sign de-

pending on the sign of the charge derived from the curvature direction) information. A scintillator system, composed of three double layers of scintillators (S1, S2, S3), provides the trigger, a time-of-flight measurement and an additional estimation of absolute charge. A silicon-tungsten imaging calorimeter, a bottom scintillator (S4) and a neutron detector are used to perform lepton-hadron discrimination. An anti-coincidence system is used off-line to reject spurious events generated by particles interacting in the apparatus. A more detailed description of PAMELA and the analysis methodology can be found in Casolino et al. (2008).

3 Data analysis

For our analysis we assume that in the inner solar system the variation of the cosmic ray flux is separable in time and space (McDonald et al., 1997b). Let $J_U(R,t,r,\theta)$ and $J_E(R,t,r_E,\theta_E)$ be the flux intensities at rigidity R and time t averaged over one solar rotation and measured by Ulysses KET along its orbit and PAMELA at Earth, respectively. Then:

$$J_U(R,t,r,\theta) = J_E(R,t,r_E,\theta_E)\cdot f(R,\Delta r,\Delta\theta) \quad (1)$$

where $f(R,\Delta r,\Delta\theta)$ is a function of the rigidity R and of the heliospheric radial (Δr) and latitudinal ($\Delta\theta$) distances between the two spacecraft. The radial distance Δr is determined by:

$$\Delta r = r_U - r_E. \quad (2)$$

Although Heber et al. (1996b) and Simpson et al. (1996) found a small asymmetry of the GCR flux with respect to the heliographic equator, we assume that the proton intensity is symmetric. Thus, the latitudinal distance $\Delta\theta$ is determined by:

$$\Delta\theta = |\theta_U| - |\theta_E|. \quad (3)$$

In both formulas U and E indicate the spatial positions of Ulysses and Earth, respectively.

Assuming that latitudinal and radial variations are separable and that the variation in r (see Eq. (2)) and θ (see Eq. (3)) can be approximated by an exponential law, Eq. (1) can be rewritten as:

$$J_U(R,t,r,\theta) = J_E(R,t,r_E,\theta_E)\exp(G_r\cdot\Delta r)\exp(G_\theta\cdot\Delta\theta) \quad (4)$$

where, G_r and G_θ are the rigidity dependent (Cummings et al., 1987; Fujii and McDonald, 1999; Heber et al., 1996a; McDonald et al., 1997a; McKibben, 1989) radial and latitudinal gradients, respectively.

3.1 Determination of the mean rigidity through temporal variation

In order to use Eq. (4) to estimate the gradients, we need to define the rigidities R for the comparison, taking into account the rigidity dependent geometric factor of the KET channel.

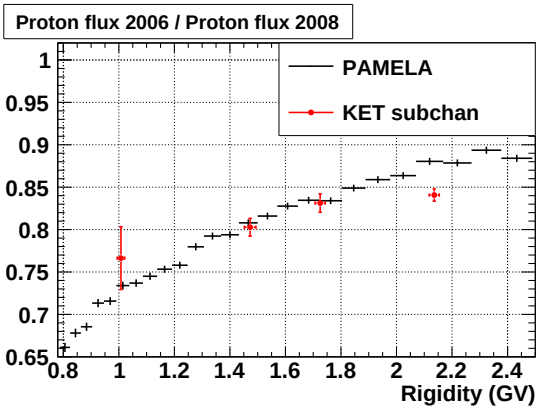

Fig. 3: Rigidity dependence of the rate of increase as defined in Eq. (5). In black the ratio between the PAMELA differential flux intensities in 2006 and in 2008 as a function of the rigidity measured by the spectrometer. The same ratio is indicated by the red symbol for the KET channels, obtained using Eq. (6), the simulated response function and the shape of the differential flux measured by PAMELA. The KET channel at rigidity ~ 1.7 GV has been selected for this analysis.

We will now discuss a method that takes advantage of the high rigidity resolution ($< 5\%$ in the region of interest) provided by the PAMELA magnetic spectrometer (Picozza et al., 2007), and we will use it as a calibration tool to find the KET channels that show a mean rigidity in good agreement with PAMELA.

Let t_1 be a time for which KET is in the southern hemisphere at a radial distance r_1 and at a latitude θ_1, and t_2, r_2, θ_2 the respective for the northern hemisphere (see periods in Fig. 1). By choosing t_1 and t_2 so that $r_1 \approx r_2$ and $\theta_1 \approx \theta_2$, and considering that, consequently, $f(R,\Delta r,\Delta\theta)$ is approximately the same at t_1 and t_2, it follows that:

$$\underbrace{\frac{J(R,t_1,r_1,\theta_1)}{J(R,t_2,r_2,\theta_2)}}_{KET} = \underbrace{\frac{J(R,t_1,r_E,\theta_E)}{J(R,t_2,r_E,\theta_E)}}_{PAMELA}. \quad (5)$$

In this way the effect of spatial gradients cancels out and the flux variation between time t_1 and time t_2 measured by KET (left side of Eq. (5)) can be compared with the flux variation measured at Earth by PAMELA (right side of Eq. (5)). Since the temporal recovery is rigidity dependent, the same flux variation can only be obtained if the mean rigidity of the KET channel is the same as the one by PAMELA. This is illustrated in Fig. 3: first we determined the proton intensities in the time intervals from 10 July 2006 to 7 November 2006 (t_1) and from 24 May 2008 to 21 September 2008 (t_2), when Ulysses was at nearly the same latitude and radial distance to the Sun. No ad hoc corrections are applied to the KET data. The black and red symbols correspond to the intensity ratios

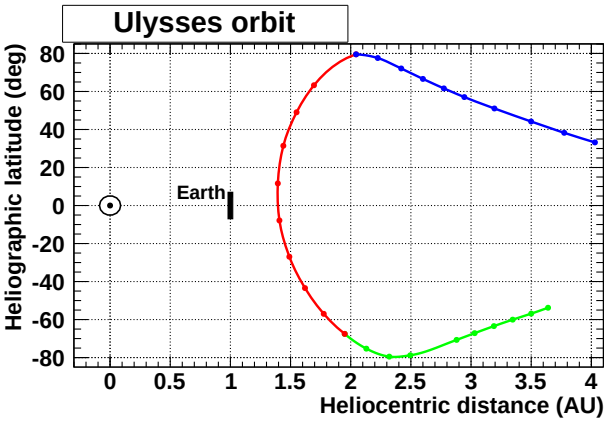

Fig. 4: Ulysses heliographic latitude as a function of radial distance. Three different phases in the trajectory have been marked by different colors: Red indicates the fast latitude scan, and green and blue the slow ascent and descent in the southern and northern hemisphere, respectively. The Earth is located between 0.98 and 1.02 AU and between $-7°$ and $7°$ with respect to the heliographic equator.

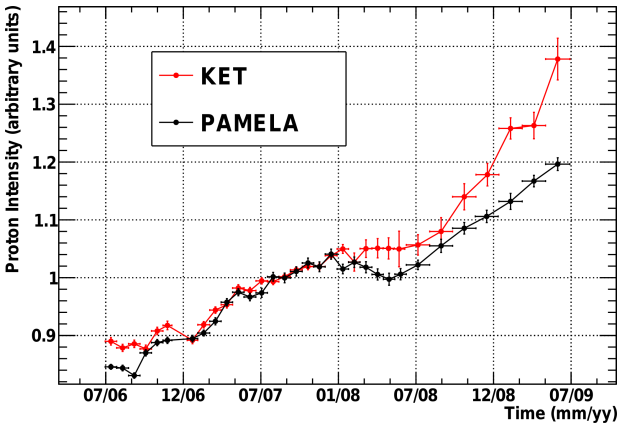

Fig. 5: 54-day averaged intensities (arbitrary units) of $\sim$ 1.7 GV protons as measured by the KET instrument aboard Ulysses (red curve) and by PAMELA (black curve). The two curves are scaled to match at the time of Ulysses' closest approach to Earth in August 2007.

between the 2006 and 2008 period using the PAMELA and KET measurements, respectively, as a function of particle rigidity. The PAMELA observation confirms the expectation that the higher the rigidity the smaller the increase in time.

The mean rigidity of a KET channel, $\langle R\rangle_{\mathrm{KET}}$, can be obtained in two ways:

– As a first approach (*method a*), we make use of the KET geometrical factor $GF_{\mathrm{KET}}(R)$, as calculated in Gieseler et al. (2010), and derive:

$$\langle R\rangle_{\mathrm{KET}}(t) = \frac{\int \mathrm{d}R \;\; J_{\mathrm{PAM}}(R,t)\cdot GF_{\mathrm{KET}}(R)\cdot R}{\int \mathrm{d}R \;\; J_{\mathrm{PAM}}(R,t)\cdot GF_{\mathrm{KET}}(R)} \quad (6)$$

where $J_{\mathrm{PAM}}(R,t)$ is the differential flux measured by PAMELA at the rigidity R and time t. We define the mean rigidity of the KET points of Fig. 3 and calculate the associated uncertainties, taking into account the variation of the proton flux due to the solar modulation, as follows:

$$\overline{\langle R\rangle_{\mathrm{KET}}} = \tfrac{1}{2}\left|\langle R\rangle_{\mathrm{KET}}(t_1)+\langle R\rangle_{\mathrm{KET}}(t_2)\right|$$

$$\delta\,\overline{\langle R\rangle_{\mathrm{KET}}} = \tfrac{1}{2}\left|\langle R\rangle_{\mathrm{KET}}(t_1)-\langle R\rangle_{\mathrm{KET}}(t_2)\right| \quad .$$

From the plot it follows that for most of the KET channels we get a reasonable agreement with PAMELA, indicating that both instruments respond to temporal variation of the same particle population.

However, the best agreement is found at a mean rigidity of (1.73 ± 0.02) GV, according to the integral average in Eq. (6).

– Alternatively (*method b*), we can also find the PAMELA rigidity interval for the comparison as the range where data from both spacecraft show a compatible variation 2006/2008. The value found for the KET channel under discussion is (1.68 ± 0.10) GV, consistent with the previous one. Both intervals will be considered in the following.

3.2 Calculation of the spatial gradients

The orbits of Ulysses and the Earth are known and provide the heliospheric radial (Δr) and latitudinal ($\Delta\theta$) distances between Ulysses and PAMELA. In Fig. 4, Ulysses latitude is shown as a function of radial distance: in red the fast latitude scan of Ulysses going from the southern to the northern hemisphere is indicated. Green and blue mark the slow ascent and descent in the southern and northern hemisphere, respectively.

In order to calculate the spatial gradients, Eq. (4) can be written in the form:

$$\log\left(\frac{J_U}{J_E}\right) = G_r\cdot\Delta r + G_\theta\cdot\Delta\theta$$

$$\underbrace{\log\left(\frac{J_U}{J_E}\right)/\Delta r}_{:=Y} = G_r + G_\theta\cdot\underbrace{\Delta\theta/\Delta r}_{:=X}$$

$$Y = G_r + G_\theta\cdot X \quad (7)$$

where $X := \Delta\theta/\Delta r$ and $Y := \log(J_U/J_E)/\Delta r$. If G_r and G_θ were independent of time and space, their values would be simply given by the offset and the slope of a straight line. It is important to recall that Eq. (7) holds only if the data from KET and PAMELA refer to the same rigidity.

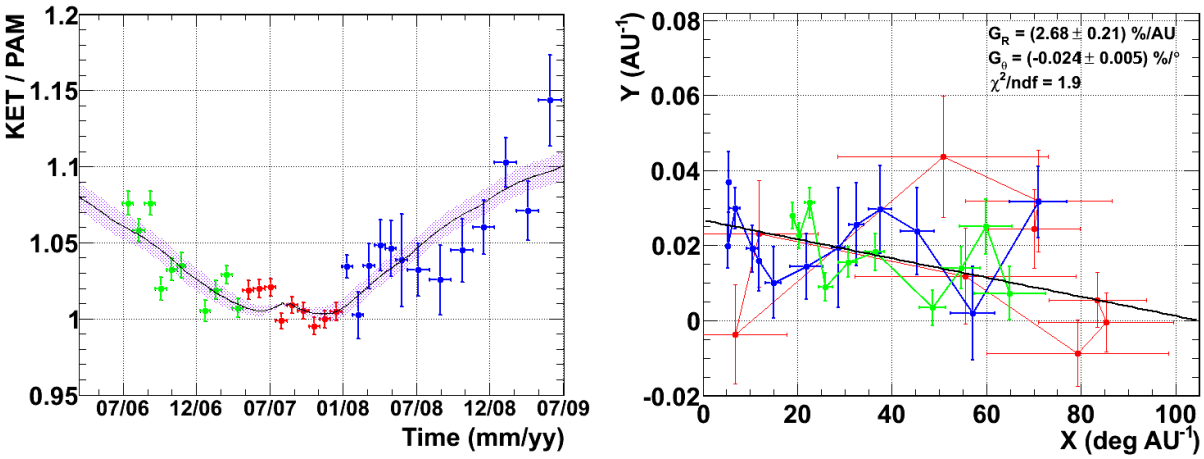

Fig. 6: Left: Ulysses (J_U) and PAMELA (J_E) intensity ratio as a function of time. PAMELA intensities have been calculated by using the measured intensity spectrum at Earth folded with the simulated response function of KET (see Fig. 2), as described in Eq. (8). The right panel displays the 54-day averaged Y as a function of X. The black line represents the result of a linear fit with a radial and latitudinal gradient of $G_r = (2.7 \pm 0.2)$%/AU and $G_\theta = (-0.024 \pm 0.005)$%/degree, respectively. As in Fig. 4, the three different phases in the trajectory have been marked by different colors.

While during the fast latitude scan X varies strongly within a 54-day averaging period, it is well defined during the slow descent and ascent period. We will make use of these colors in order to check our results for consistency in the northern and southern hemisphere, which would be reflected in the Y versus X plot.

In the following we will determine the parameters G_r and G_θ comparing the given KET channel with the PAMELA data selected using the two alternative methods described in Sect. 3.1. In order to minimize the uncertainties in the estimation of the flux intensities of the KET instrument, potentially connected to the absolute determination of the geometrical factor, we adopt a normalization of the time profiles at the closest approach of Ulysses to Earth, in August 2007. For this purpose, an iterative method has been applied, that will be described in detail in Appendix A.

Method a)

The intensity time profile at Earth, $J_E(t)$, is calculated by weighting the measured PAMELA energy spectra with the response function of the KET channel as displayed in Fig. 2:

$$J_E(t) \propto \int \mathrm{d}R \quad J_{\mathrm{PAM}}(R,t) \cdot GF_{\mathrm{KET}}(R), \tag{8}$$

where $J_{\mathrm{PAM}}(R,t)$ is the differential intensity measured by PAMELA at the rigidity R and at the time t. The time history of both the KET and the weighted PAMELA channel are shown in Fig. 5. Although in 2007 and 2008 the lowest sunspot numbers have been obtained since the beginning of space age, the cosmic ray flux in the rigidity range below 2.5 GV has not recovered (Heber et al., 2009).

The intensity time profile ratio J_U/J_E is displayed in Fig. 6 left, while Y as a function of X, as determined by Eq. (7), is displayed on the right. Accordingly to Fig. 4, the three different phases in the trajectory segments have been marked by different colors. The black line through the data points represents the linear fit which gives the latitudinal gradient G_θ as the slope and the radial gradient G_r as the intercept with the Y-axis. The iterative algorithm (see Appendix A) converges after four iteration steps, as shown by Fig. 10, independently of the starting conditions, indicating the robustness of our method.

The results are:

$$\begin{aligned} G_r &= (2.7 \pm 0.2)\ \%/\mathrm{AU} \\ G_\theta &= (-0.024 \pm 0.005)\ \%/\mathrm{degree} \quad . \end{aligned} \tag{9}$$

Method b)

The gradients can also be determined without considering the simulated response function of KET. As discussed in Sect. 3.1 and shown in Fig. 3, the intensity of the PAMELA proton flux in the rigidity range (1.68 ± 0.10) GV has the same temporal increase as the KET channel under analysis. By selecting PAMELA protons in this rigidity range, we get the gradients:

$$\begin{aligned} G_r &= (2.6 \pm 0.3)\ \%/\mathrm{AU} \\ G_\theta &= (-0.023 \pm 0.008)\ \%/\mathrm{degree} \quad . \end{aligned} \tag{10}$$

These values are consistent with the values of *method a)*, indicating that the simulated response function of the KET channel leads to systematic uncertainties smaller than the estimated errors on the gradients.

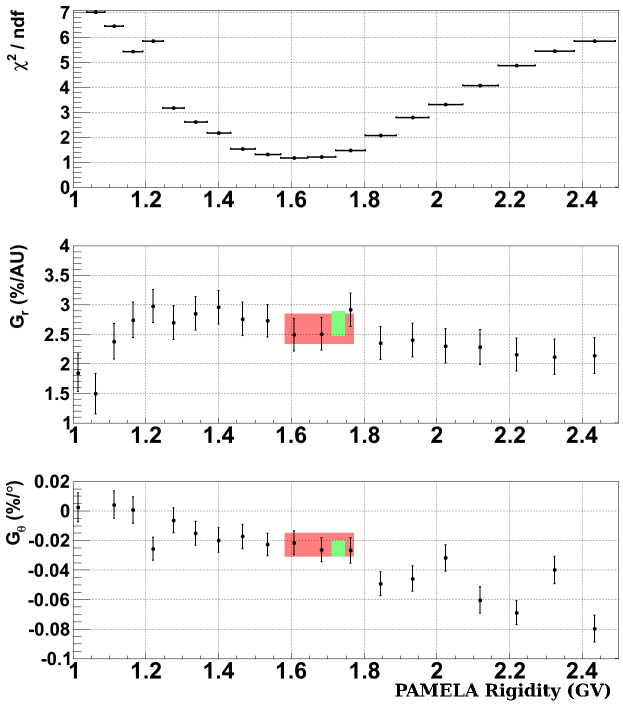

Fig. 7: χ^2 quality parameter (top panel) of the fit of Eq. (7) to the data, radial (middle panel) and latitudinal gradient (bottom panel), as a function of PAMELA rigidity R. A minimum of χ^2 is present in the rigidity interval between $R = 1.54$ GV and $R = 1.72$ GV. While the value of the radial gradient is nearly independent of the rigidity interval, the latitudinal gradient is varying from 0%/degree to -0.06%/degree. Marked by shading are the results for the radial and latitudinal gradient as described in the previous section, showing a good agreement between the two methods described in Sect. 3.2. See text for more details.

3.2.1 The χ^2-minimization

In what follows, we validate the robustness of the analysis described in the previous section: we calculate the spatial gradients by using the measurements by the PAMELA detector in several small rigidity bins. The quality of the best fit is expected to vary with rigidity. As discussed in Sect. 3.1, Eq. (4) is expected to correctly describe the $\frac{J_U(t)}{J_E(R,t)}$ only at the right mean rigidity R.

Figure 7, top panel, shows that an absolute minimum is present in the χ^2-distribution around 1.7 GV, consistent with the previous estimations. The values for the radial gradients (middle panel) and latitudinal gradients (bottom panel) are also compatible with the values in Eq. (9) (green area) and Eq. (10) (red area). Furthermore, around the minimum the values of the gradients do not significantly change for small variations in the estimated mean rigidity.

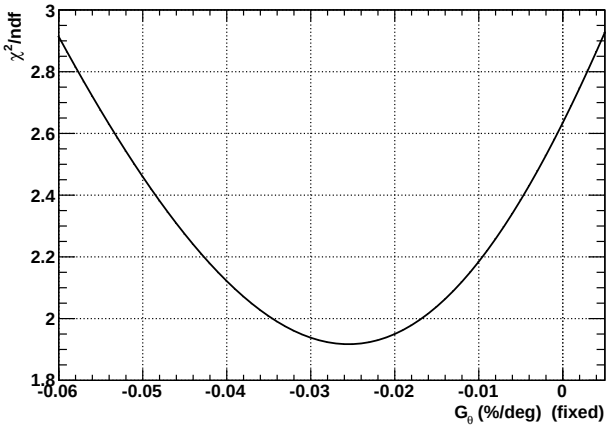

Fig. 8: χ^2/ndf of the fit obtained for different fixed value of G_θ.

4 Summary and conclusions

The Ulysses mission has contributed significantly to the understanding of the major cosmic ray observations in the inner heliosphere and at high heliolatitudes. The first major challenge was that the latitudinal gradients for cosmic ray protons at all energies, but especially at low energies (< 100 MeV), were observed significantly smaller than predicted by drift models for an $A < 0$-solar magnetic epoch. It became quickly evident that this was due to the overestimation of drifts in the polar regions of the heliosphere and to a too simple geometry for the heliospheric magnetic field. The extension of the mission and the launch of the PAMELA detector in 2006 allowed to perform the comparative analysis illustrated in this work and to determine the radial and latitudinal gradient during an $A < 0$-solar magnetic epoch.

The analysis has been proven to be robust in several ways: 1) the rate of increase from 2006 to 2008, determined by the KET and the PAMELA instrument independently, agrees very well at the considered rigidity; 2) by varying the mean rigidity between 1.0 GV and 2.5 GV, the best representation of the spatial variation leads to the smallest χ^2 if a mean rigidity about 1.7 GV is chosen; 3) both the radial and latitudinal gradient do not strongly vary with the mean rigidity in the interval of interest.

Thanks to the large geometric factor and high precision measurements of the PAMELA instrument, we could show here that:

1. the mean rigidity comes to be $1.6 - 1.8$ GV independently of the method chosen,

therefore we conclude that the simulated response function is reliable and the results of *method a)* can be taken:

2. the radial gradient during the 2000 A$<$0-solar magnetic epoch is (2.7 ± 0.2)%/AU

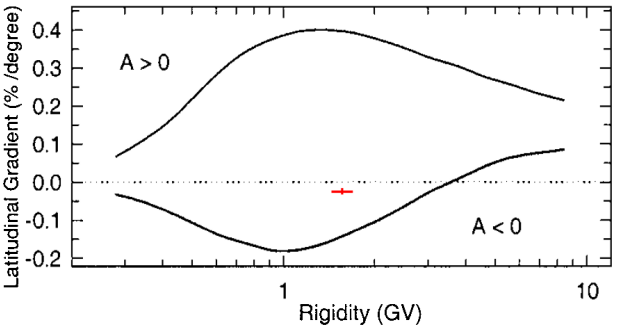

Fig. 9: Computed latitudinal gradients for protons during the past $A < 0$-solar minimum and the prediction for the current $A < 0$-solar minimum (see Potgieter et al., 2001). Marked by red point is the latitudinal gradient found in this study.

3. the latitudinal gradient during the same period is only (-0.024 ± 0.005)%/degree.

Although the absolute error of the uncertainty for the latitudinal gradients looks very small, it is about 20% of the observed value. However, the data are not statistically consistent with a null latitudinal gradient. Applying Student's t-test (Eadie et al., 1971) to the data, the hypothesis of a null latitudinal gradient is rejected at 99.6% C.L. The gradients lie within the following 95% C.L. intervals: $G_\theta = (-0.0255 \pm 0.0182)$%/degree and $G_r = (-2.68 \pm 0.42)$%/AU. In Fig. 8 we additionally report the χ^2 value of the fit obtained by changing a fixed value of the latitudinal gradient: as expected, the best fit minimizes the χ^2 at $G_\theta \approx -0.024$%/degree.

In order to estimate the impact of varying solar activity we fitted function in Eq. (7) to the ratios using the period for the slow ascend south, the fast latitude scan and the slow descend north, separately. The values are summarized in Table 1 and vary between 2.5%/AU and 3.1%/AU and -0.022%/degree and -0.039%/degree, indicating a trend with solar activity cycle to become smaller for solar minimum. However, since the deviation from the mean value of 2.7%/AU and -0.026%/degree is smaller than one sigma, we randomly chose 20 points out of the full data set of 32 points and calculated the gradients for this subset 10^5 times. The mean of all these values is given in the lowest row.

Our analysis clearly reveals that for the period from 2006 to 2009, close to solar minimum in an $A < 0$-solar magnetic epoch,

1. the radial gradient is positive as expected. However, it is smaller than previously reported values (e.g. McDonald et al., 1997a).
2. the latitudinal gradient is negative and much smaller than the ones observed in the previous $A < 0$-solar magnetic epoch (Cummings et al., 1987; McDonald et al., 1997a).

Table 1: The first four rows report the values of the gradients obtained by selecting different time periods. The last row reports the mean and standard deviation of the distribution of values obtained by randomly selecting 10^5 times a subsample of 20 points out the full data set of 32 points.

Data set	G_r (%/ AU)	G_θ (%/ deg)	χ^2/ ndf
All data	2.67 ± 0.21	-0.026 ± 0.006	1.98
South pole (green)	3.10 ± 0.38	-0.039 ± 0.011	3.32
Fast latitude scan (red)	3.01 ± 1.18	-0.026 ± 0.016	2.52
North pole (blue)	2.53 ± 0.36	-0.022 ± 0.017	1.04
Statistical sub-sampling (20 points over 32)	2.6 ± 0.3	-0.025 ± 0.006	

Figure 9 from Potgieter et al. (2001) displays the calculated rigidity dependence of the non-local latitudinal gradient. The parameters for this calculations are optimized to reproduce the measurements from Heber et al. (1996b) for the fast latitude scan in 1994 to 1995 during an $A < 0$-solar magnetic epoch (see also Burger et al., 2000). The prediction shown by the lower curve for the $A < 0$-magnetic epoch are based on the same set of parameters but opposite magnetic field polarity. In contrast to their calculations, the absolute value of the latitudinal gradient found is much lower. There are several processes which may account for the observed discrepancy:

– The measured solar wind parameters, wind pressure and magnetic field strength are much lower than in the previous solar cycle (McComas et al., 2008; Smith and Balogh, 2008). Thus the size of the modulation volume as well as the diffusion tensor will be different (e.g. Ferreira et al., 2003)

– As stated in Potgieter et al. (2001), drift effects depend on the maximum latitudinal extent of the heliospheric current sheet (tilt angle). Although the magnetic field strength was much lower than in the previous solar magnetic minima, the tilt angle was much higher (e.g. Heber et al., 2009).

– The diffusion coefficients may depend on the heliospheric magnetic field polarity (Ferreira and Potgieter, 2004).

In order to contribute to our understanding on how the Sun is modulating the galactic cosmic ray flux and especially to support theoretical studies of the propagation parameters in

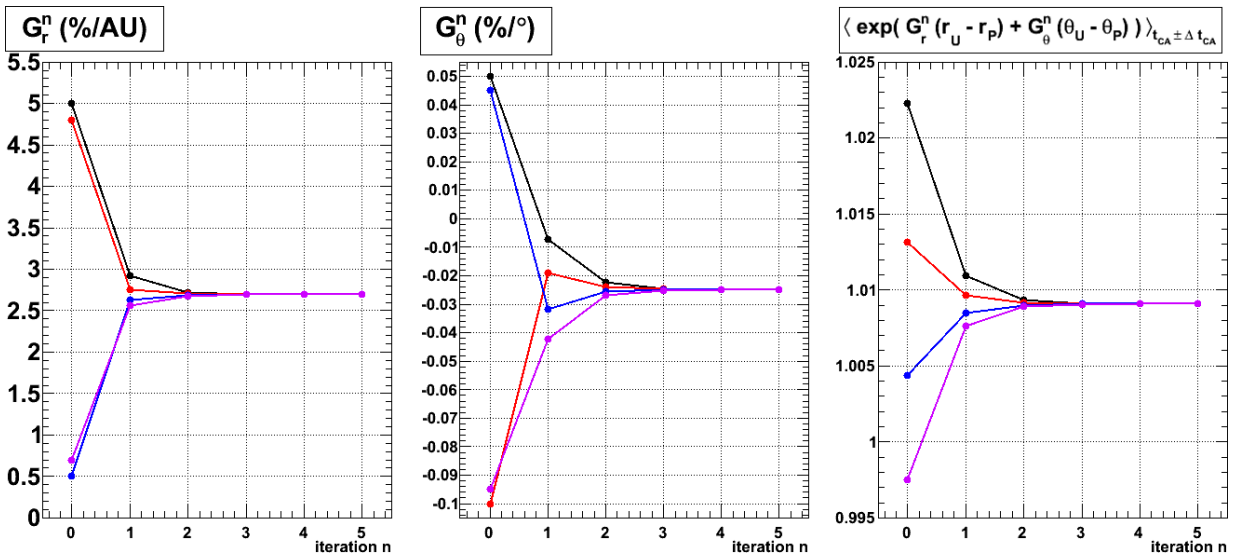

Fig. 10: Radial and latitudinal gradients as well as the normalized intensity ratio at the closest approach as a function of the number of iteration. When the radial and the latitudinal gradients change less than 0.002% from one step to the next we stop the procedure. The minimization is perfomed using the code MINUIT (James and Roos, 1975).

the inner heliosphere (Shalchi et al., 2010; Minnie et al., 2007; Burger et al., 2000), detailed calculations and further analysis of the Ulysses and PAMELA data are necessary. From the latter we will obtain the radial and latitudinal gradient at other rigidities between several 100 MV and a few GV.

Appendix A

In the following we will describe the iterative method that allows us to mininimize the uncertainties in the estimation of the ratio J_U/J_E due to the systematic in our knowledge of J_U. This is necessary for the measurement of the spatial gradients G_r and G_θ according to Eq. (7). We will show this method as applied to the rigidity range defined for the *method a)*.

We start with arbitrary spatial gradients $G_r^{k=0}$ and $G_\theta^{k=0}$ (where k is the iteration step index) chosen in the range of findings in the 1980s and 1990s (Heber et al., 2008; Fujii and McDonald, 1999). We use them to determine a normalization that is for each step k defined by:

$$\left.\frac{J_U}{J_E}\right|_N^k := \sum_{i=1}^{n} \frac{\exp\left(G_r^{k-1}\cdot\Delta r_i\right)\cdot\exp\left(G_\theta^{k-1}\cdot\Delta\theta_i\right)}{n}, \qquad \text{(A1)}$$

with $n = 27$ the number of days in the normalization interval N, in August 2007, Δr_i and $\Delta\theta_i$ the according daily values of the trajectory data. By using this in Eq. (7), we derive successive approximations of the spatial gradients. After a few iterations, this method converges and delivers the final normalization and spatial gradients. In the first step of our iterative method the normalization $\left.\frac{J_U}{J_E}\right|_N$ of KET and PAMELA intensities as a function of time has been calculated by using different radial and latitudinal gradients (see Eq. (A1)). The corresponding values for Y are calculated by using Eq. (7). By fitting Eq. (7) to the data, a new latitudinal gradient G_θ^1 as the slope and the radial gradient G_r^1 as the intercept with the X-axis are found.

Figure 10 displays in the two left panels the radial and latitudinal gradients as a function of iteration steps. As starting conditions we took two physical and two non-physical extreme cases:

1. A large radial and negative latitudinal gradient (red curve). This case would have been the one expected for the current A<0-solar magnetic epoch (Cummings et al., 1987; McDonald et al., 1997a).

2. A small radial but a positive latitudinal gradient (blue curve). This case would be the one expected for an $A <$ 0-solar magnetic epoch (Heber et al., 2008).

3. A large radial and positive latitudinal gradient (black curve).

4. A small radial and negative latitudinal gradient (magenta curve).

The iterations stop when the gradients become stable within 0.002% from one step to the next. The minimization is perfomed using the code MINUIT (James and Roos, 1975).

Acknowledgements. The ULYSSES/KET project is supported under grant No. 50 OC 0902 and SUA 07/13 by the German Bundesministerium für Wirtschaft through the Deutsches Zentrum für

Luft- und Raumfahrt (DLR). The PAMELA mission is sponsored by the Italian National Institute of Nuclear Physics (INFN), the Italian Space Agency (ASI), the Russian Space Agency (Roskosmos), the Russian Academy of Science, the Deutsches Zentrum für Luft- und Raumfahrt (DLR), the Swedish National Space Board (SNSB) and the Swedish Research Council (VR). The German - Italian collaboration has been supported by the Deutsche Forschungsgemeinschaft under grant HE3279/11-1. This work profited from the discussions with the participants of the ISSI workshop "Cosmic Rays in the Heliosphere II".

[†]**PAMELA Collaboration**

O. Adriani[1,2], G. C. Barbarino[3,4], G. A. Bazilevskaya[5], R. Bellotti[6,7], M. Boezio[8], E. A. Bogomolov[9], L. Bonechi[1,2], M. Bongi[2], V. Bonvicini[8], S. Borisov[10,11,12], S. Bottai[2], A. Bruno[6,7], F. Cafagna[7], D. Campana[4], R. Carbone[4,11], P. Carlson[13], M. Casolino[10], G. Castellini[14], L. Consiglio[4], M. P. De Pascale[10,11], C. De Santis[10,11], N. De Simone[10,11], V. Di Felice[10,11], A. M. Galper[12], W. Gillard[13], L. Grishantseva[12], P. Hofverberg[13], G. Jerse[8,15], A. V. Karelin[12], S. V. Koldashov[12], S. Y. Krutkov[9], A. N. Kvashnin[5], A. Leonov[12], V. Malvezzi[10], L. Marcelli[10], M. Martucci[10,11] A. G. Mayorov[12], W. Menn[16], V. V. Mikhailov[12], E. Mocchiutti[8], A. Monaco[6,7], N. Mori[2], N. Nikonov[9,10,11], G. Osteria[4], F. Palma[10,11], P. Papini[2], M. Pearce[13], P. Picozza[10,11], C. Pizzolotto[8], M. Ricci[17], S. B. Ricciarini[2], L. Rossetto[13], M. Simon[16], R. Sparvoli[10,11], P. Spillantini[1,2], Y. I. Stozhkov[5], A. Vacchi[8], E. Vannuccini[2], G. Vasilyev[9], S. A. Voronov[12], J. Wu[13,*], Y. T. Yurkin[12], G. Zampa[8], N. Zampa[8], V. G. Zverev[12]

[1]University of Florence, Department of Physics, I-50019 Sesto Fiorentino, Florence, Italy
[2]INFN, Sezione di Florence, I-50019 Sesto Fiorentino, Florence, Italy
[3]University of Naples "Federico II", Department of Physics, I-80126 Naples, Italy
[4]INFN, Sezione di Naples, I-80126 Naples, Italy
[5]Lebedev Physical Institute, RU-119991, Moscow, Russia
[6]University of Bari, Department of Physics, I-70126 Bari, Italy
[7]INFN, Sezione di Bari, I-70126 Bari, Italy
[8]INFN, Sezione di Trieste, I-34149 Trieste, Italy
[9]Ioffe Physical Technical Institute, RU-194021 St. Petersburg, Russia
[10]INFN, Sezione di Rome "Tor Vergata", I-00133 Rome, Italy
[11]University of Rome "Tor Vergata", Department of Physics, I-00133 Rome, Italy
[12]Moscow Engineering and Physics Institute, RU-11540 Moscow, Russia
[13]KTH, Department of Physics, and the Oskar Klein Centre for Cosmoparticle Physics
AlbaNova University Centre, SE-10691 Stockholm, Sweden
[14]IFAC, I-50019 Sesto Fiorentino, Florence, Italy
[15]University of Trieste, Department of Physics, I-34147 Trieste, Italy
[16]Universität Siegen, Department of Physics, D-57068 Siegen, Germany
[17]INFN, Laboratori Nazionali di Frascati, Via Enrico Fermi 40, I-00044 Frascati, Italy
[*]On leave from School of Mathematics and Physics, China University of Geosciences, CN-430074 Wuhan, China

Edited by: R. Vainio
Reviewed by: two anonymous referees

References

Burger, R. A., Potgieter, M. S., and Heber, B.: Rigidity dependence of cosmic ray proton latitudinal gradients measured by the Ulysses spacecraft: Implications for the diffusion tensor, J. Geophys. Res., 105, 27 447–27 456, doi:10.1029/2000JA000153, 2000.

Casolino, M., Picozza, P., Altamura, F., Basili, A., De Simone, N., Di Felice, V., Pascale, M. D., Marcelli, L., Minori, M., Nagni, M., Sparvoli, R., Galper, A., Mikhailov, V., Runtso, M., Voronov, S., Yurkin, Y., Zverev, V., Castellini, G., Adriani, O., Bonechi, L., Bongi, M., Taddei, E., Vannuccini, E., Fedele, D., Papini, P., Ricciarini, S., Spillantini, P., Ambriola, M., Cafagna, F., Marzo, C. D., Barbarino, G., Campana, D., Rosa, G. D., Osteria, G., Russo, S., Bazilevskaja, G., Kvashnin, A., Maksumov, O., Misin, S., Stozhkov, Y., Bogomolov, E., Krutkov, S., Nikonov, N., Bonvicini, V., Boezio, M., Lundquist, J., Mocchiutti, E., Vacchi, A., Zampa, G., Zampa, N., Bongiorno, L., Ricci, M., Carlson, P., Hofverberg, P., Lund, J., Orsi, S., Pearce, M., Menn, W., and Simon, M.: Launch of the space experiment PAMELA, Adv. Space Res., 42, 455–466, doi:10.1016/j.asr.2007.07.023, http://www.sciencedirect.com/science/article/B6V3S-4P9625D-1/2/7b49861564f9fa0f239fb6523df2f03a, 2008.

Cummings, A. C., Stone, E. C., and Webber, W. R.: Latitudinal and radial gradients of anomalous and galactic cosmic rays in the outer heliosphere, Geophys. Res. Lett., 14, 174–177, 1987.

Eadie, W. T., Drijard, D., James, F. E., Roos, M., and Sadoulet, B.: Statistical methods in experimental physics, North-Holland, Amsterdam, 1971.

Ferreira, S. E. S. and Potgieter, M. S.: Long-Term Cosmic-Ray Modulation in the Heliosphere, Astrophys. J., 603, 744–752, doi:10.1086/381649, 2004.

Ferreira, S. E. S., Potgieter, M. S., Heber, B., and Fichtner, H.: Charge-sign dependent modulation in the heliosphere over a 22-year cycle, Ann. Geophys., 21, 1359–1366, 2003.

Fujii, Z. and McDonald, F. B.: The radial intensity gradients of galactic and anomalous cosmic rays, Adv. Space Res., 23, 437–441, doi:10.1016/S0273-1177(99)00101-5, 1999.

Gieseler, J., De Simone, N., Heber, B., and Di Felice, V.: The response function of the Kiel Electron Telescope, re-investigated , Adv. Space Res., p. in preparation, 2010.

Heber, B., Dröge, W., Ferrando, P., Haasbroek, L., Kunow, H., Müller-Mellin, R., Paizis, C., Potgieter, M., Raviart, A., and Wibberenz, G.: Spatial variation of > 40 MeV/n nuclei fluxes observed during Ulysses rapid latitude scan, Astron. Astrophys., 316, 538–546, 1996a.

Heber, B., Dröge, W., Kunow, H., Müller-Mellin, R., Wibberenz, G., Ferrando, P., Raviart, A., and Paizis, C.: Spatial variation of > 106 MeV proton fluxes observed during the Ulysses rapid latitude scan: Ulysses COSPIN/KET results, Geophys. Res. Lett., 23, 1513–1516, 1996b.

Heber, B., Ferrando, P., Raviart, A., Wibberenz, G., Müller-Mellin, R., Kunow, H., Sierks, H., Bothmer, V., Posner, A., Paizis, C., and Potgieter, M. S.: Differences in the temporal variation of galactic cosmic ray electrons and protons: Implications from Ulysses at solar minimum, Geophys. Res. Lett., 26, 2133–2136, 1999.

Heber, B., Gieseler, J., Dunzlaff, P., Gomez-Herrero, R., Müller-Mellin, R., Mewaldt, R., Potgieter, M. S., and Ferreira, S.: Latitudinal gradients of galactic cosmic rays during the 2007 solar minimum, Astrophys. J., 1, doi:10.1086/592596, 2008.

Heber, B., Kopp, A., Gieseler, J., Müller-Mellin, R., Fichtner, H., Scherer, K., Potgieter, M. S., and Ferreira, S. E. S.: Modulation of Galactic Cosmic Ray Protons and Electrons During an Unusual Solar Minimum, Astrophys. J., 699, 1956–1963, doi:10.1088/0004-637X/699/2/1956, 2009.

James, F. and Roos, M.: Minuit - a system for function minimization and analysis of the parameter errors and correlations, Computer Physics Communications, 10, 343–367, doi:10.1016/0010-4655(75)90039-9 http://www.sciencedirect.com/science/article/B6TJ5-46FPXJ7-2C/2/58a665cfee07e122711a859fef69c955, 1975.

Jokipii, J. R., Levy, E. H., and Hubbard, W. B.: Effects of particle drift on cosmic ray transport, I. General properties, application to solar modulation , Astrophys. J., 213, 861–868, 1977.

McComas, D. J., Ebert, R. W., Elliott, H. A., Goldstein, B. E., Gosling, J. T., Schwadron, N. A., and Skoug, R. M.: Weaker solar wind from the polar coronal holes and the whole Sun, Geophys. Res. Lett., 35, 18103, doi:10.1029/2008GL034896, 2008.

McDonald, F. B., Ferrando, P., Heber, B., Kunow, H., McGuire, R., Müller-Mellin, R., Paizis, C., Raviart, A., and Wibberenz, G.: A comparative study of cosmic ray radial and latitudinal gradients in the inner and outer heliosphere, J. Geophys. Res., 102, 4643–4652, doi:10.1029/96JA03673, 1997a.

McDonald, F. B., Ferrando, P., Heber, B., Kunow, H., McGuire, R., Mller-Mellin, R., Paizis, C., Raviart, A., and Wibberenz, G.: A comparative study of cosmic ray radial and latitudinal gradients in the inner and outer heliosphere, J. Geophys. Res., 102, 4643–4652, doi:10.1029/96JA03673, 1997b.

McKibben, R. B.: Reanalysis and confirmation of positive latitude gradients for anomalous helium and Galactic cosmic rays measured in 1975-1976 with Pioneer II, J. Geophys. Res., 94, 17021–17033, 1989.

Minnie, J., Bieber, J. W., Matthaeus, W. H., and Burger, R. A.: On the Ability of Different Diffusion Theories to Account for Directly Simulated Diffusion Coefficients, Astrophys. J., 663, 1049–1054, doi:10.1086/518765, 2007.

Picozza, P., Galper, A. M., Castellini, G., Adriani, O., Altamura, F., Ambriola, M., Barbarino, G. C., Basili, A., Bazilevskaja, G. A., Bencardino, R., et al.: PAMELA-A payload for antimatter matter exploration and light-nuclei astrophysics, Astroparticle Physics, 27, 296315, 2007.

Potgieter, M. S., Ferreira, S. E. S., and Burger, R.: Modulation of cosmic rays in the heliosphere over 11 and 22 year cycles: a modelling perspective, Adv. Space Res., 27, 481–492, 2001.

Shalchi, A., Li, G., and Zank, G. P.: Analytic forms of the perpendicular cosmic ray diffusion coefficient for an arbitrary turbulence spectrum and applications on transport of Galactic protons and acceleration at interplanetary shocks, Astrophys. Space Sci., 325, 99–111, doi:10.1007/s10509-009-0168-6, 2010.

Simpson, J., Anglin, J., Barlogh, A., Bercovitch, M., Bouman, J., Budzinski, E., Burrows, J., Carvell, R., Connell, J., Ducros, R., Ferrando, P., Firth, J., Garcia-Munoz, M., Henrion, J., Hynds, R., Iwers, B., Jacquet, R., Kunow, H., Lentz, G., Marsden, R., McKibben, R., Müller-Mellin, R., Page, D., Perkins, M., Raviart, A., Sanderson, T., Sierks, H., Treguer, L., Tuzzolino, A., Wenzel, K.-P., and Wibberenz, G.: The Ulysses Cosmic-Ray and Solar Particle Investigation, Astron. Astrophys. Suppl., 92, 365–399, 1992.

Simpson, J. A., Zhang, M., and Bame, S.: A Solar Polar North-South Asymmetry for Cosmic-Ray Propagation in the Heliosphere: The ULYSSES Pole-to-Pole Rapid Transit, Astrophys. J. Lett., 465, L69, 1996.

Smith, E. J. and Balogh, A.: Decrease in heliospheric magnetic flux in this solar minimum: Recent Ulysses magnetic field observations, Geophys. Res. Lett., 35, 22 103, doi:10.1029/2008GL035345, 2008.

33rd International Cosmic Ray Conference, Rio de Janeiro 2013
The Astroparticle Physics Conference

ICRC 2013

Inner heliosphere spatial gradients of GCR protons in the low GeV range

Jan Gieseler[1], Mirko Boezio[2], Marco Casolino[3], Nicola De Simone[3], Valeria Di Felice[3], Bernd Heber[1], Matteo Martucci[3], Piergiorgio Picozza[3], and the PAMELA Collaboration.

[1] *Institute of Experimental and Applied Physics, University of Kiel*
[2] *INFN, Structure of Trieste and Physics Department of University of Trieste, Italy*
[3] *INFN, Structure of Rome "Tor Vergata" and Physics Department of University of Rome "Tor Vergata", Italy*

gieseler@physik.uni-kiel.de

Abstract: The spacecraft Ulysses was launched in October 1990 in the maximum phase of solar cycle 22, reached its final, highly inclined (80.2°) Keplerian orbit around the Sun in February 1992, and was finally switched off in June 2009. The Kiel Electron Telescope (KET) aboard Ulysses measures electrons from 3 MeV to a few GeV and protons and helium in the energy range from 6 MeV/nucleon to above 2 GeV/nucleon. Because the Ulysses measurements reflect not only the spatial but also the temporal variation of the energetic particle intensities, it is essential to know the intensity variations for a stationary observer in the heliosphere. This was accomplished in the past with the Interplanetary Monitoring Platform-J (IMP 8) until it was lost in 2006. Fortunately, the satellite-borne experiment PAMELA (Payload for Antimatter Matter Exploration and Light-nuclei Astrophysics) was launched in June 2006 and can be used as a reliable 1 AU baseline for measurements of the KET aboard Ulysses. Furthermore, we show that measurements of higher nuclei by the Advanced Composition Explorer (ACE), launched 1997 and still operating, can also be used as an extended baseline and to improve the analysis. With these tools at hand, we have the opportunity to determine the spatial gradients of galactic cosmic ray (GCR) protons between several tenth MeV to a few GeV in the inner heliosphere during the extended minimum of solar cycle 23.

Keywords: GCR, cosmic ray, gradient, Ulysses, PAMELA.

1 Introduction

Galactic cosmic rays (GCRs) enter the heliosphere isotropically and are exposed to multiple types of interactions as they traverse to the vicinity of the Earth, resulting in the so called modulation. The main effects are scattering at irregularities in the interplanetary magnetic field, gradient and curvature drifts, convection as well as adiabatic deceleration in the expanding solar wind. The importance of these particle drifts for the modulation of GCRs has been emphasized in the past [6]. Models including these effects [10] gave predictions for differently charged GCR particles which could be confirmed for both polarity solar cycles [1, 3, 7, 8]. Following these models, one expect the latitudinal gradient of positively charegd GCRs to be negative for an A<0 andpositive for an A>0 solar cycle, respecitvely, with an reversed behavior for electrons. The radial gradient should always be positive. Proton observations from Ulysses/KET have been used for such analysis in the past, using IMP 8 or ACE/CRIS as a 1 AU baseline [4, 5]. In a previous work we compared proton measurements of Ulysses/KET and PAMELA [2]. Here, we carry on with this analysis and investigate a broader energy range for protons.

2 Instrumentation

2.1 PAMELA

PAMELA (Payload for Antimatter Matter Exploration and Light-nuclei Astrophysics) is a satellite-borne spectrometer designed to study charged particles, in particular antiparticles, up to hundreds of GeV with high statistics and a sophisticated electron-proton discrimination. It was launched in June 2006 on an polar elliptical orbit around Earth with an altitude between 350 km and 600 km. During high latitude phases the low geomagnetic cutoff allows the detection of particles down to 50 MeV. A detailled description of the experiment can be found in [9].

2.2 Ulysses Kiel Electron Telescope

The Ulysses mission, launched 1990, delievered (amongst others) energetic particle measurements from February 1992 to June 2009 while on its highly inclined (80.2°) Keplerian orbit around the Sun. In particular, the Kiel Electron Telescope (KET) measured protons and α particles from 6 MeV/nucleon to above 2 GeV/nucleon and electrons from 3 MeV to a few GeV. See [12] for a full desciption of the instrument.

The trajectory information of Ulysses from 2006 to 2009 is shown in the lower panel of Fig.1. On top, the sunspot number and the tilt angle of the solar magnetic field are displayed, indicating that the investigation

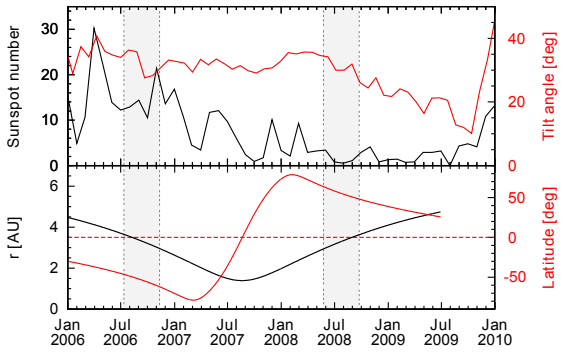

Figure 1: Time profiles of tilt angle, sunspot number (top), and Ulysses heliocentric latitude and radial distance (bottom). Shadings indicate the intervals used to investigate the temporal variation (see Sect. 3.2).

period showed very low solar activity, marking the unusual minimum of solar cycle 23. Two periods in late 2006 and mid 2008 are marked by shading when Ulysses was at nearly the same latitude and radial distance to the Sun. This has been used later for the analysis of the temporal variation.

3 Data Analysis

3.1 Mathematical Description of the Spatial Gradients

We assume that temporal and spatial variations of GCRs in the inner heliosphere can be separated [7]. It has been shown [1, 3, 7, 8] that the radial and latitudinal gradients G_r and G_θ are rigidity dependent. Thus, we compare the GCR intensities J at rigidity R and time t averaged over one solar rotation. Let $J_U(R,t,r,\theta)$ and $J_E(R,t,r_E,\theta_E)$ be the intensities measured by Ulysses/KET on its orbit and PAMELA at Earth, respectively. These intensities can be connected (at the same rigidity) with a function $f(R,\Delta r,\Delta\theta)$ that depends on the differences in heliospheric radial distance ($\Delta r = r_U - r_E$) and latitude ($\Delta\theta = |\theta_U| - |\theta_E|$) between the two observers:

$$J_U(R,t,r,\theta) = J_E(R,t,r_E,\theta_E)\cdot f(R,\Delta r,\Delta\theta) \quad (1)$$

Here, we assume a symmetric distribution of GCRs with respect to the heliographic equator, although small asymmetries have been found in the past [4, 13]. If we further make the assumption that the variations in radius and latitude are separable and can be approximated by an exponential law, Eq. 1 can be rewritten as:

$$J_U(R,t,r,\theta) = J_E(R,t,r_E,\theta_E)\cdot e^{G_r\Delta r}\cdot e^{G_\theta\Delta\theta} \quad (2)$$

with the rigidity dependent radial and latitudinal gradients G_r and G_θ.

3.2 Selection of Comparison Channels

To make sure that we compare measurements at the same rigidity, we apply the same method as in our previous analysis [2]. We use the high rigidity resolution of PAMELA as a calibration tool for the rigidity dependent geometric factors of the Ulysses/KET protons.

Channel	<E_{KET}>/GeV	<E_{PAM}>/GeV
P190.1	0.527	0.517
P190.2	0.945	0.923
P190.3	1.182	1.133

Table 1: Mean energies of selected proton measurement channel pairs of Ulysses/KET and PAMELA for which the gradients are individually calculated.

Marked by shading in Fig. 1 are the two time periods t_1 (July 2006 to November 2006) and t_2 (May 2008 to September 2008) when Ulysses was at almost the same position in the southern and northern solar hemisphere, respectively, so that $r_1 \approx r_2$ and $|\theta_1| \approx |\theta_2|$. Under the assumption that the spatial gradients do not change between t_1 and t_2, it follows that the arguments of the exponential functions from Eq. 2 are the same for both periods and the effects of spatial gradients cancel out. Thus, we can directly compare the ratios of the intensity measurements of Ulysses/KET and PAMELA of both periods:

$$\frac{J_U(R,t_1,r_1,\theta_1)}{J_U(R,t_2,r_2,\theta_2)} = \frac{J_E(R,t_1,r_E,\theta_E)}{J_E(R,t_2,r_E,\theta_E)} \quad (3)$$

The resulting time variations are shown in Fig. 2. They are plotted with respect to energy (instead of rigidity) to allow an easier differentiation between observations of protons and heavier ions. As expected, the modulation is higher at lower energies and vanishes for high energies. We can now verify that selected measurement channels of PAMELA are sensitive to the same energetic particle populations as Ulysses/KET because they show (within error limits) the same temporal variation. Since our previous work [2], the PAMELA proton data has been further investigated and refined. This process has not been finished yet for α particles. Thus, their analysis will be the topic of a future effort. For now, we end up with a selection of three proton channel pairs of Ulysses/KET and PAMELA measurements for which we individually determine the spatial gradients (cf. Tab. 1). In addition, Fig. 2 demonstrates that in principle we can use ACE/CRIS measurements of higher nuclei at Earth as a 1 AU baseline to calculate the spatial gradients of α particles detected at the Ulysses orbit. This will be done in an upcoming work.

3.3 Calculation of the Spatial Gradients

To calculate the radial and latitudinal gradients G_r and G_θ, we can rewrite Eq. 2:

$$\ln\left[\frac{J_U}{J_E}\right] = G_r\cdot\Delta r + G_\theta\cdot\Delta\theta \quad (4)$$

$$\underbrace{\frac{1}{\Delta r}\ln\left[\frac{J_U}{J_E}\right]}_{=:Y} = G_r + G_\theta\cdot\underbrace{\frac{\Delta\theta}{\Delta r}}_{=:X} \quad (5)$$

$$Y = G_r + G_\theta\cdot X \quad (6)$$

Under the assumption that the gradients are independent of time and space, they can easily be obtained by the slope and offset of a straight line which is fitted

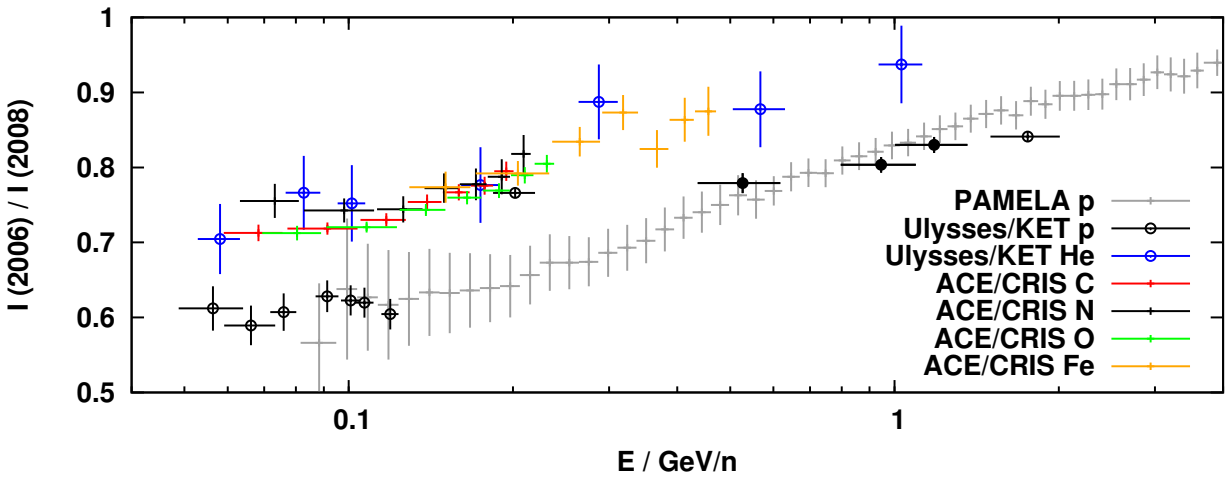

Figure 2: Time variations from 2006 to 2008 of different particle intensity measurements with respect to energy. Marked by full circles are the Ulysses/KET proton channels used here for gradient calculations.

	all data		without FLS		slow ascent (green)		slow descent (blue)	
	Fit (1)	Fit (2)	Fit (1)	Fit (2)	Fit (1)	Fit (2)	Fit (1)	Fit (2)
P190.1								
G_r	2.24±0.36	2.97±0.2	3.24±0.13	2.87±0.2	4.84±0.34	5.08±0.6	2.23±0.15	2.17±0.24
G_θ	-0.054 ±0.01	-0.044 ±0.007	-0.054 ±0.005	-0.036 ±0.007	-0.063 ±0.01	-0.073 ±0.019	-0.036 ±0.006	-0.036 ±0.011
χ^2/ndf	7.024	5.476	5.311	5.095	2.034	1.994	4.811	4.841
P190.2								
G_r	2.48±0.2	3.01±0.16	3.08±0.1	2.99±0.16	2.19±0.25	2.19±0.42	3.13±0.12	3.15±0.19
G_θ	-0.043 ±0.006	-0.055 ±0.006	-0.050 ±0.004	-0.053 ±0.006	-0.040 ±0.008	-0.041 ±0.013	-0.031 ±0.006	-0.036 ±0.009
χ^2/ndf	5.207	4.884	5.52	5.428	4.262	4.259	6.1	6.075
P190.3								
G_r	2.14±0.21	2.51±0.16	2.67±0.11	2.47±0.16	1.85±0.28	2.22±0.44	2.39±0.11	2.22±0.18
G_θ	-0.063 ±0.006	-0.069 ±0.006	-0.066 ±0.005	-0.066 ±0.006	-0.059 ±0.009	-0.07 ±0.014	-0.039 ±0.005	-0.036 ±0.009
χ^2/ndf	4.25	4.033	4.619	4.497	4.493	4.413	4.679	4.622

Table 2: Radial and latitudinal gradients (in %/AU and %/degree, respectively) and quality of fit for different selection criteria (cf. Fig. 3) and fit methods. Indicated by (1) are the values obtained by the bootstrap Monte-Carlo approach while (2) marks the fit routine using the `fitexy` algorithm. See Tab. 1 for corresponding energies.

through the data of a graph where $Y = \ln[J_U/J_E]/\Delta r$ is plotted over $X = \Delta\theta/\Delta r$. This is shown for one selected pair of Ulysses/KET and PAMELA measurements in Fig. 5. In addition, Fig. 3 and 4 show the orbit data (Δr and $\Delta\theta$) and the corresponding intensity ratio J_U/J_E, respectively. In all of these three Figures three different phases of the Ulysses trajectory are color coded: Red indicates the fast latitude scan (FLS) while the slow ascent and descent in both solar hemispheres are marked in green and blue, respectively.

In order to include the uncertainties of Fig. 5 in the fit calculation, two different methods are applied:

Minimization of the sum of squares, using the definition of χ^2 from the `fitexy` function from Numerical Recipes [11] to fit the data with errors in both x and y dimension.

Bootstrap Monte-Carlo approach. We choose for each data point randomly a value inside of its uncertainties, and calculate the fit for this ensemble of data points. This process is repeated 100 000 times. Our final values for the gradients are then the mean values over these 100 000 iterations, with the standard deviations as their error.

Because Ulysses covers such a wide latitude range during the FLS, the uncertainties in X are quite large in this interval. Therefore, the gradient calculation is carried out using the data from all times, without the FLS, and from the slow ascent and descent only, respectively. The results are shown in Tab. 2 and Fig. 6.

4 Summary and Conclusion

We investigated the spatial gradients of ~0.1-1.2 GeV GCR protons in the inner heliosphere from 2006 to 2009, during the unusual solar minimum of solar

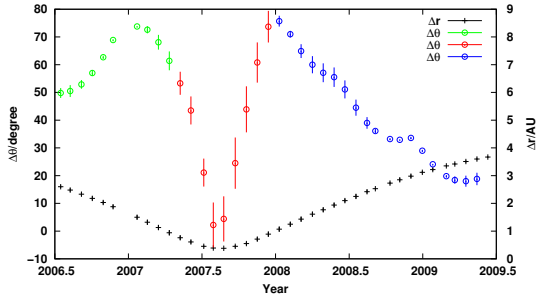

Figure 3: Differences in radial and latitudinal distance (Δr and $\Delta\theta$) between Ulysses and PAMELA for the analysis period. Marked in red is the fast latitude scan (FLS) of Ulysses while green and blue indicate its slow ascent and descent, respectively.

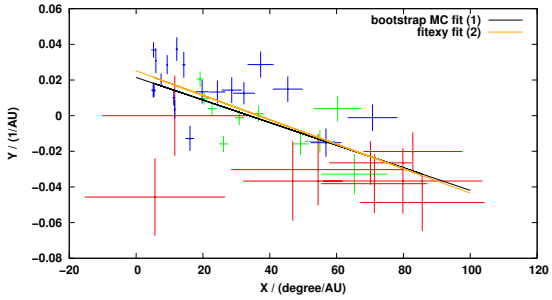

Figure 5: Y as a function of X (cf. Eq. 5) for P190.3. See Fig. 3 for color coding. The lines show the results of the two different fit methods, with $G_r = (2.14 \pm 0.21)\%/\mathrm{AU}$ and $G_\theta = (-0.063 \pm 0.006)\%/\mathrm{deg}$ for the bootstrap Monte-Carlo approach (black), and $G_r = (2.51 \pm 0.16)\%/\mathrm{AU}$ and $G_\theta = (-0.069 \pm 0.006)\%/\mathrm{deg}$ for the fit routine using the `fitexy` algorithm (orange).

cycle 23 (A<0). As expected, the radial gradients are always positive. They are also in the same range as in our previous analysis [2], the small differences can be attributed to a slightly changed analysis method and the already mentioned PAMELA data refinement. Nevertheless, our radial gradients are smaller than previous results [7]. In agreement with the expectations is the fact that our latitudinal gradients are small and negative. But they are by a factor of ∼2 bigger than previously [2]. This shows how sensitive the analysis is to small changes in the data. However, our findings are still almost zero and with that smaller than predicted by previous A<0-solar magnetic epoch observations [1, 7] and simulations [10].

Acknowledgment: The Ulysses/KET project is supported under Grant 50 OC 1302 by the German Bundesministerium für Wirtschaft through the Deutsches Zentrum für Luft- und Raumfahrt.The PAMELA mission is sponsored by the Italian National Institute of Nuclear Physics (INFN), the Italian Space Agency (ASI), the Russian Space Agency (Roskosmos), the Russian Academy of Science, the Deutsches Zentrum für Luft- und Raumfahrt (DLR), the Swedish National Space Board (SNSB) and the Swedish Research Council (VR). The German-Italian collaboration has been supported by the Deutsche Forschungsgemeinschaft under grant HE3279/11-1. Sunspot number data was obtained via the web site http://sidc.be/sunspot-data/

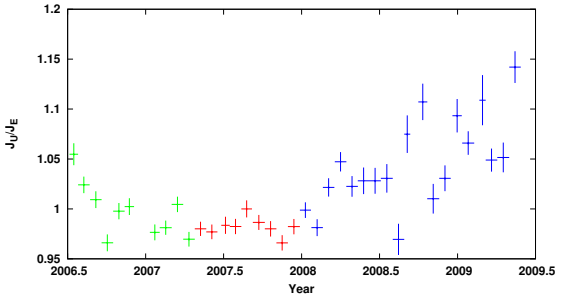

Figure 4: Intensity ratio time profile of P190.3 (cf. Tab. 1). See Fig. 3 for color coding.

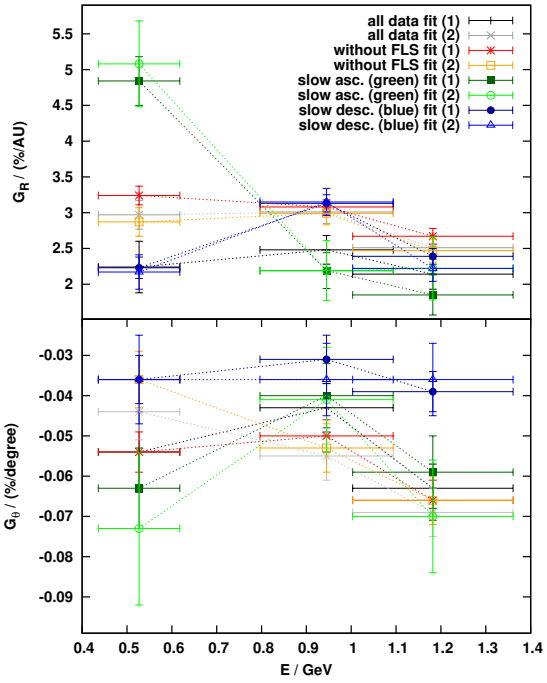

Figure 6: Radial and latitudinal gradients for different selection criteria and fit methods, as in Tab. 2.

courtesy of the SIDC-team, Royal Observatory of Belgium. Wilcox Solar Observatory data was obtained via the web site http://wso.stanford.edu courtesy of J.T. Hoeksema.

References

[1] Cummings, A.C. et al. 1987, Geophys. Res. Lett., 14, 174
[2] De Simone, N. et al. 2011, Astrophys. Space Sci. Trans., 7, 425
[3] Heber, B. et al. 1996, Astron. Astrophys., 316, 538
[4] Heber, B. et al. 1996, Geophys. Res. Lett., 23, 1513
[5] Heber, B. et al. 2008, Astrophys. J., 689(2), 1443
[6] Jokipii, J.R. et al. 1977, Astrophys. J., 213, 861
[7] McDonald, F.B. et al. 1997, J. Geophys. Res., 102, 4643
[8] McKibben, R.B. 1989, J. Geophys. Res., 94, 17021
[9] Picozza, P. et al. 2007, Astropart. Phys., 27(4), 296
[10] Potgieter, M.S. et al. 2001, Adv. Space Res., 27, 481
[11] Press, W.H. et al. 1996, Numerical Recipes in Fortran
[12] Simpson, J.A. et al. 1992, Astron. Astrophys. Suppl., 92, 365
[13] Simpson, J.A. et al. 1996, Astrophys. J. Lett., 465, L69

A&A 589, A32 (2016)
DOI: 10.1051/0004-6361/201527972

Astronomy & Astrophysics

Spatial gradients of GCR protons in the inner heliosphere derived from *Ulysses* COSPIN/KET and PAMELA measurements

J. Gieseler and B. Heber

Institute of Experimental and Applied Physics, University of Kiel, Leibnizstr. 11, 24118 Kiel, Germany
e-mail: gieseler@physik.uni-kiel.de

Received 15 December 2015 / Accepted 27 January 2016

ABSTRACT

Context. During the transition from solar cycle 23 to 24 from 2006 to 2009, the Sun was in an unusual solar minimum with very low activity over a long period. These exceptional conditions included a very low interplanetary magnetic field (IMF) strength and a high tilt angle, which both play an important role in the modulation of galactic cosmic rays (GCR) in the heliosphere. Thus, the radial and latitudinal gradients of GCRs are very much expected to depend not only on the solar magnetic epoch, but also on the overall modulation level.
Aims. We determine the non-local radial and the latitudinal gradients of protons in the rigidity range from ~0.45 to 2 GV.
Methods. This was accomplished by using data from the satellite-borne experiment Payload for Antimatter Matter Exploration and Light-nuclei Astrophysics (PAMELA) at Earth and the Kiel Electron Telescope (KET) onboard *Ulysses* on its highly inclined Keplerian orbit around the Sun with the aphelion at Jupiter's orbit.
Results. In comparison to the previous $A > 0$ solar magnetic epoch, we find that the absolute value of the latitudinal gradient is lower at higher and higher at lower rigidities. This energy dependence is therefore a crucial test for models that describe the cosmic ray transport in the inner heliosphere.

Key words. cosmic rays – interplanetary medium – Sun: heliosphere – Sun: activity

1. Introduction

Galactic cosmic rays (GCRs) that propagate in the heliosphere are affected by the solar activity. They are scattered at magnetic field irregularities, undergo convection and adiabatic deceleration in the expanding solar wind, and are exposed to gradient and curvature drifts in the large-scale heliospheric magnetic field. This results in the modulation of GCRs with solar activity, shown in Fig. 1. The upper panel displays the (normalized) count rate of the Kiel neutron monitor plotted over time. A simple comparison with the sunspot number in the panel below shows the anticorrelation between solar activity and GCR intensity. In the 1960s, 1980s and 2000, when the solar magnetic field pointed toward the Sun in the northern hemisphere (so-called $A < 0$-magnetic epoch), the time profiles were peaked, whereas they were more or less flat in the 1970s and 1990s during the $A > 0$-solar magnetic epoch, showing a correlation with the 22-year solar magnetic cycle.

To understand solar and heliospheric modulation, it is vital to reproduce the spatial distribution of cosmic rays in the three-dimensional heliosphere, that is, around solar minimum periods. Keys to fulfilling this task are measuring the cosmic ray distribution in the three-dimensional heliosphere and modeling the cosmic ray transport. An important prediction from drift-dominated modulation models is the expectation that protons will have large positive and negative latitudinal gradients in an $A > 0$- and $A < 0$-solar magnetic epoch, respectively. In agreement with expectations, the latitudinal gradients observed in the 1990s were positive (Heber et al. 1996a,b; Simpson et al. 1996). But in contrast to these expectations, Heber et al. (1996a, 2006) showed that the measured spectrum over the poles in 1994 and 1995 was still lower than the Voyager measurements at 62 AU and that it was highly modulated. Not only were the latitudinal gradients much smaller than anticipated, the energy dependence also showed an unexpected maximum at a rigidity of about 1 GV (see Fig. 8 in Heber et al. 1996a).

These investigations relied on particle measurements made by the Cosmic Ray and Solar Particle Investigation Kiel Electron Telescope (COSPIN/KET) and High Energy Telescope (COSPIN/HET) using particle measurements from the IMP 8 satellite as a baseline close to Earth. Unfortunately, in 2006 IMP 8 was lost and a new baseline only became available when the Payload for Antimatter Matter Exploration and Light-nuclei Astrophysics (PAMELA) experiment was launched in July 2006. De Simone et al. (2011) analyzed proton data at 1.6−1.8 GV from *Ulysses* COSPIN/KET and PAMELA for the period from launch of PAMELA in 2006 to the end of *Ulysses* in 2009. They showed in agreement with the model calculation that the latitudinal gradients were negative, but again in contrast to the prediction, these gradients were much smaller than expected.

The Voyager 1 spacecraft located beyond 120 AU in the outer heliosheath (Stone et al. 2013; Krimigis et al. 2013) has shown that the local interstellar spectrum for ions is known with a low uncertainty (Potgieter et al. 2014). These small uncertainties result from the fact that there might even be modulation in the outer heliosheath (Scherer et al. 2011; Herbst et al. 2012; Strauss et al. 2013). Among others, the rigidity dependence of the latitudinal gradient in the $A < 0$-solar magnetic epoch is a crucial quantity that helps to determine the propagation parameters in the heliosphere.

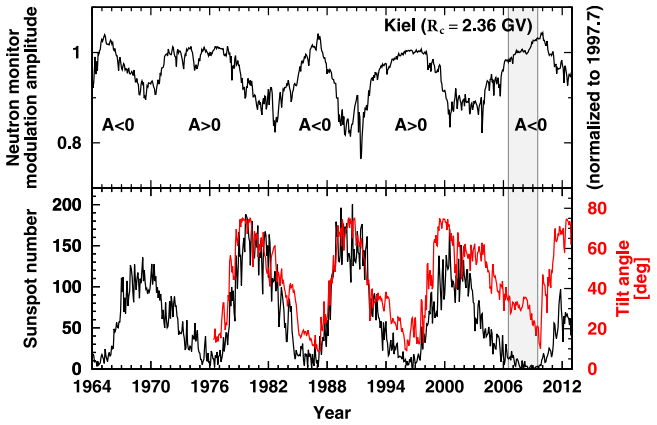

Fig. 1. *Top*: monthly Kiel neutron monitor count rate (cutoff rigidity R_c = 2.36 GV), normalized to 1997.7. *Bottom*: monthly sunspot number from the Royal Observatory of Belgium and tilt angle (classic model) from the Wilcox Solar Observatory. The period investigated in this work is shaded.

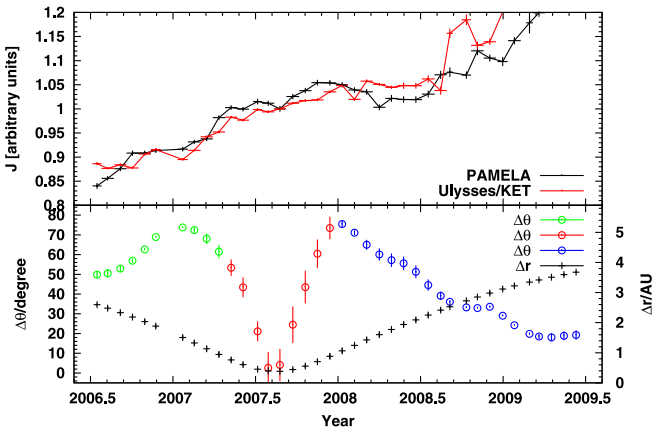

Fig. 2. *Top*: intensities of ∼1.9 GV protons measured by *Ulysses*/KET and PAMELA, normalized in August 2007 (see Sect. 3.1). *Bottom*: differences in radial and latitudinal distance (Δr and $\Delta\theta$) between *Ulysses* and PAMELA for the analysis period. The fast latitude scan of *Ulysses* is plotted in red, green and blue indicate its slow ascent and descent, respectively.

2. Instrumentation

The determination of non-local gradients relies on measurements that are well calibrated against each other. During *Ulysses*' first fast latitude scan in the 1990s, a baseline close to Earth for the *Ulysses* COSPIN/KET (see Sect. 2.1) was the University of Chicago instrument onboard the IMP 8 spacecraft. After 2006, the analysis had to rely on measurements of the PAMELA instrument (see Sect. 2.2).

2.1. Ulysses Kiel electron telescope

Ulysses was a joint ESA/NASA mission that was launched in October 1990 and was switched off in June 2009. During more then 18 years of measurements, the spacecraft performed three of its highly inclined (80.2°) orbits around the Sun, with the aphelion at Jupiter's orbit and the perihelion close to 1 AU. Part of these orbits were three so-called fast latitude scans, during which the spacecraft covered a latitude range from −80° to +80° in roughly one year. The three southern polar passes occurred from 1994-06-26 to 1994-11-05, 2000-09-06 to 2001-01-16 and 2006-11-17 to 2007-04-03, respectively. The corresponding passes of the northern polar region were from 1995-06-19 to 1995-09-29, 2001-08-31 to 2001-12-10 and from 2007-11-30 to 2008-03-15. While the second polar pass took place during solar maximum periods, the first and third polar passes were performed during solar minimum conditions during an $A > 0$ and $A < 0$-solar magnetic epoch, respectively. The time period that we analyze here is shaded in Fig. 1.

The Kiel Electron Telescope (KET) onboard *Ulysses* was part of the Cosmic Ray and Solar Particle Investigation (COSPIN) experiment and measured electrons, protons, and α-particles in the range from 2.5 MeV to above 300 MeV and from 4 MeV/n to above 2 GeV/n, respectively (see Simpson et al. 1992).

2.2. PAMELA

The ongoing experiment called Payload for Antimatter Matter Exploration and Light-nuclei Astrophysics (PAMELA) is a spectrometer onboard a Russian Resurs-DK1 satellite, launched on a polar elliptical orbit around Earth in June 2006 (Picozza et al. 2007). Its main purpose is the measurement of electrons, positrons, protons, antiprotons, and light nuclei over a very wide range of energy up to hundreds of GeV. With an altitude between 350 km and 600 km, the detection of charged particles down to 50 MeV is only possible during high-latitude phases with a low geomagnetic cutoff.

3. Gradient calculation

To calculate the rigidity-dependent (Cummings et al. 1987; Heber et al. 1996a; McDonald et al. 1997; McKibben 1989) radial and latitudinal gradients of GCR protons, $G_r(R)$ and $G_\theta(R)$, we have to make the assumption that the variations in time and space can be separated. We compared the intensity $J_U(R, t, r, \theta)$ of protons measured at *Ulysses*' position at radial distance r, latitude θ, rigidity R, and time t averaged over one solar rotation (∼27 days) with $J_E(R, t, r_E, \theta_E)$, the corresponding proton intensity detected at Earth by PAMELA at the same rigidity (Fig. 2). In comparison to the analysis in De Simone et al. (2011), the *Ulysses*/KET data were re-investigated; the response functions were updated, for instance. Additionally, we used here the improved PAMELA proton data obtained from Adriani et al. (2013) through the ASI Science Data Center (ASDC).

To validate that our measurements from PAMELA and *Ulysses*/KET are sensitive to the same particle populations, we followed the same approach as described in De Simone et al. (2011) and investigated the temporal intensity variations of both measurements. First, we chose two time periods t_1 and t_2 where *Ulysses* was at nearly the same radial distance ($r_1 \approx r_2$) and absolute latitude ($|\theta_1| \approx |\theta_2|$). Then, we built the ratios of intensity spectra measured at t_1 and t_2 by *Ulysses*/KET and PAMELA, respectively. If we assume that the spatial gradients did not change from 2006 to 2009, they cancel out and the ratio measured by *Ulysses*/KET should be equal to that of PAMELA:

$$\frac{J_U(R, t_1, r_1, \theta_1)}{J_U(R, t_2, r_2, \theta_2)} = \frac{J_E(R, t_1, r_E, \theta_E)}{J_E(R, t_2, r_E, \theta_E)}. \quad (1)$$

This is true for the six proton channels from *Ulysses*/KET and their corresponding PAMELA channels at comparable rigidities that we used in this study (cf. Table 1). Each pair of these

Table 1. Resulting radial and latitudinal gradients.

$\langle R_U \rangle$/GV	$\langle R_P \rangle$/GV	G_r / (%/AU)	G_θ / (%/degree)
0.46	0.46	3.6 ± 0.7	-0.10 ± 0.03
1.13	1.11	3.4 ± 0.3	-0.04 ± 0.01
1.63	1.61	3.3 ± 0.2	-0.04 ± 0.01
1.90	1.85	2.8 ± 0.2	-0.06 ± 0.01

Notes. Proton mean rigidities as measured by *Ulysses*/KET and PAMELA that are used to calculate the corresponding gradients. Radial and latitudinal gradients for the whole investigation period, estimated by the arithmetic mean of the corresponding gradients for the two different fit routines (see Table A.1 for detailed results).

measurements J_U and J_E at rigidity R is connected with a function $f(R, \Delta r, \Delta\theta)$ depending on the differences in radial distance and absolute latitude, $\Delta r = r_U - r_E$ and $\Delta\theta = |\theta_U| - |\theta_E|$, respectively:

$$J_U(R, t, r, \theta) = J_E(R, t, r_E, \theta_E) \cdot f(R, \Delta r, \Delta\theta). \quad (2)$$

Although some asymmetries have been reported (e.g. Heber et al. 1996b; Simpson et al. 1996), we assumed a symmetric distribution of GCRs along the heliographic equator. By separating the variations in radial distance and latitude (Bastian et al. 1980; McKibben et al. 1979) and approximating them with an exponential function (e.g. Cummings et al. 2009), Eq. (2) can be rewritten as

$$J_U(R, t, r, \theta) = J_E(R, t, r_E, \theta_E) \cdot e^{G_r \cdot \Delta r} \cdot e^{G_\theta \cdot \Delta\theta}. \quad (3)$$

To estimate the rigidity-dependent radial and latitudinal gradients $G_r(R)$ and $G_\theta(R)$, we followed the approach by Paizis et al. (1995) and further transformed Eq. (3):

$$\ln\left[\frac{J_U(R)}{J_E(R)}\right] = G_r(R) \cdot \Delta r + G_\theta(R) \cdot \Delta\theta \quad (4)$$

$$\underbrace{\frac{1}{\Delta r} \ln\left[\frac{J_U(R)}{J_E(R)}\right]}_{=:Y} = G_r(R) + G_\theta(R) \cdot \underbrace{\frac{\Delta\theta}{\Delta r}}_{=:X} \quad (5)$$

$$Y(R) = G_r(R) + G_\theta(R) \cdot X. \quad (6)$$

If we assume that the radial and latitudinal gradients are constant over the observed time interval and in space, we can calculate their values from the slope and offset by fitting a straight line to the data, as shown for example in Fig. 3, where $Y = \ln[J_U/J_E]/\Delta r$ is plotted with respect to $X = \Delta\theta/\Delta r$.

In this figure three different phases of *Ulysses*' orbit (cf. Fig. 2) are indicated by different colors: red shows the fast latitude scan, green and blue indicate the slow ascent and descent over the two solar poles, respectively. The large uncertainties in X and Y for the fast latitude scan data points originate in the wide latitude ranges and the small radial distances, respectively, during this period. We therefore omitted the two data points of *Ulysses*' closest approach to Earth (the two red data points far left in Fig. 3) in our analysis. In addition, we estimated the gradients not only for the whole time period, but also separately for the slow ascent (including the first two fast latitude scan data points) and for the slow descent (including the last three fast latitude scan data points) (cf. Table A.1).

Because there are uncertainties in the X and Y dimension, we used two different methods to calculate the fits according to Eq. (6) including the uncertainties:

1. Fit the data by minimizing the sum of squares using the χ^2 from the `fitexy` function from Numerical Recipes (Press et al. 1996), which includes ΔX and ΔY.

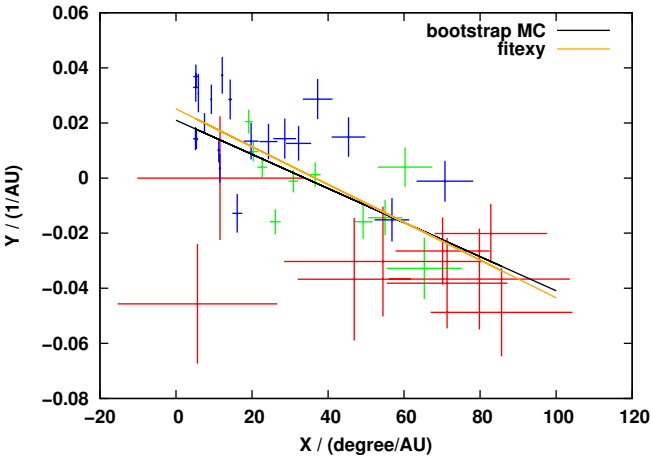

Fig. 3. Y as a function of X (cf. Eq. (5)) for ~1.9 GV protons. See Fig. 2 for color coding. The lines show the results of the two different fit methods, with $G_r = (2.14 \pm 0.21)$%/AU and $G_\theta = (-0.063 \pm 0.006)$%/deg for the bootstrap Monte Carlo approach (black), and $G_r = (2.51 \pm 0.16)$%/AU and $G_\theta = (-0.069 \pm 0.006)$%/deg for the fit routine using the `fitexy` algorithm (orange).

2. Perform a bootstrap Monte Carlo approach where we take one random value inside of its uncertainties for each data point of Fig. 3. Afterward, a standard minimization was applied to the corresponding ensemble of data points. The whole procedure was carried out 100 000 times, resulting in mean values over all iterations as the gradients, with the standard deviations as their error.

3.1. Normalization

Because of non-neglectable uncertainties in the calculation of the absolute intensity values measured by *Ulysses*/KET, we normalized the measured intensity ratios J_U/J_E using a 25-day measurement interval in August 2007. During this time, *Ulysses* was closest to Earth (cf. Fig. 2), resulting in the smallest gradient effects. Following Eq. (3), we expect for all rigidities a ratio J_U/J_E close to 1. The normalized value $\langle J_U(R)/J_E(R) \rangle_N$ at a given rigidity is determined by the following iterative process:

$$\left\langle \frac{J_U(R)}{J_E(R)} \right\rangle_N^k = \frac{1}{n} \sum_{i=1}^{n=25} e^{G_r^{k-1} \cdot \Delta r_i} \cdot e^{G_\theta^{k-1} \cdot \Delta\theta_i} \quad (7)$$

for iteration step k and the 25 daily values of Δr_i and $\Delta\theta_i$. We started with extreme but realistic values for $G_r^{k=0}$ and $G_\theta^{k=0}$ that covered different scenarios (see Fig. 4). With these starting values for the gradients, we first calculated the intensity normalization $\langle J_U(R)/J_E(R) \rangle_N^{k=1}$ in August 2007 according to Eq. (7). This normalization factor was then inserted in Eq. (5) to adjust the intensity ratio:

$$\underbrace{\frac{1}{\Delta r} \ln\left[\left\langle \frac{J_U(R)}{J_E(R)} \right\rangle_N^{k=1} \cdot \frac{J_U(R)}{J_E(R)}\right]}_{=:Y} = G_r(R) + G_\theta(R) \cdot \underbrace{\frac{\Delta\theta}{\Delta r}}_{=:X}. \quad (8)$$

With Eq. (8) we can calculate the spatial gradients $G_r(R)$ and $G_\theta(R)$. These were then used in Eq. (7) as $G_r^{k=1}$ and $G_\theta^{k=1}$ for the next iteration $k = 2$. This process was repeated until the value for the normalization and thus the spatial gradients converged. Figure 4 exemplarily shows the analysis for ~1.9 GV

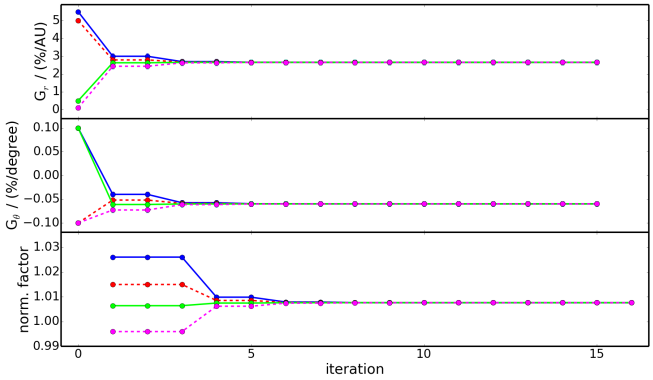

Fig. 4. Iterative normalization of J_U/J_E. *The top and middle panels* show the spatial gradients we used to calculate the normalization factor of J_U/J_E (*bottom panel*). Shown here are four different iteration runs for ~1.9 GV protons using the `fitexy` fit (cf. Sect. 3.1 for more details).

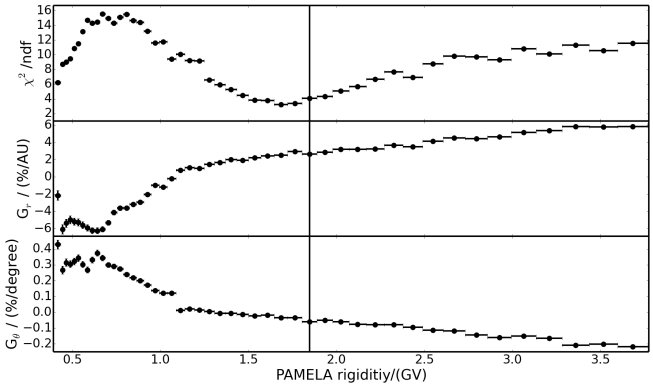

Fig. 5. *Top*: χ^2 of the fit to Eq. (8) using the `fitexy` function for protons measured at *Ulysses*/KET at ~1.9 GV as a function of PAMELA proton measurements at varying rigidities used in Eq. (8). *Middle and bottom*: corresponding radial and latitudinal gradients, respectively. The PAMELA rigidity bin closest to the theoretical mean rigidity of *Ulysses*/KET is indicated with the vertical line.

protons. For every channel pair, this procedure converges after a few iterations, independently of the starting values for the spatial gradients.

3.2. Rigidity identification

We have already mentioned that the radial and latitudinal gradients are both rigidity dependent. Furthermore, our analysis and especially Eq. (8), from which we obtain the gradients by a fit routine, are only valid if we compare intensities at the same rigidity. Because of this, the quality of the fits is expected to vary if we compare *Ulysses*/KET measurements at a fixed rigidity with PAMELA measurements at varying rigidities (and vice versa). We used this to check the reliability of our analysis by calculating the different χ^2 of the fits to Eq. (8) for PAMELA measurements at varying rigidities. As an example, the results for protons that are measured by *Ulysses*/KET at ~1.9 GV are shown in Fig. 5 (top panel) together with the resulting radial (middle) and latitudinal (bottom) gradients. The PAMELA rigidity bin closest to the theoretical mean rigidity of *Ulysses*/KET is indicated by the vertical line. This data point is very close to the absolute χ^2 minimum for the fit, indicating once again that

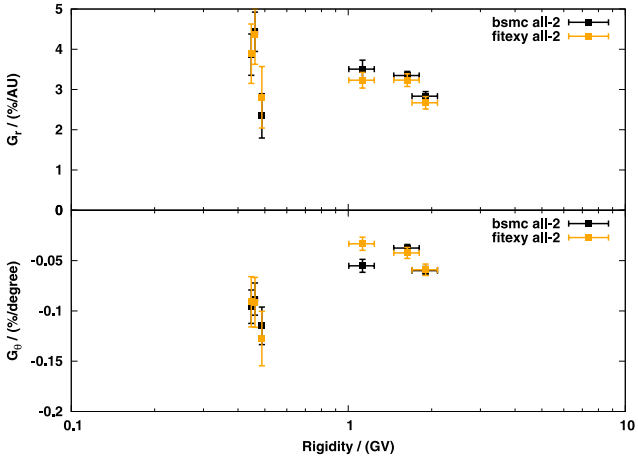

Fig. 6. Calculated radial (*top*) and latitudinal (*bottom*) gradients for the whole investigation period. Shown are the gradients resulting from the bootstrap Monte Carlo fit approach in black and using the `fitexy` function in orange. For all three rigidities below 1 GV the same PAMELA channel is used (see Sect. 3.2).

we compare measurements at the same rigidity. In addition, both resulting gradients show only small variations around the rigidity of the χ^2 minimum. The two other proton measurements at rigidities above 1 GV show similar results.

However, the three low-rigidity measurements have all the lowest χ^2 at the same comparison rigidity, meaning that they are all sensitive to the same PAMELA rigidity channel. All three have adjacent mean rigidities estimated by *Ulysses*/KET. If we perform our analysis using the nominal rigidity channels of PAMELA, the corresponding radial and latitudinal gradients show strong variations and are inconsistent in some parts, even within the errors (see Table A.1), whereas they agree reasonably well if we use the very same PAMELA rigidity channel for all three *Ulysses*/KET channels (see Fig. 6 and Table A.1). This can be mainly attributed to low counting statistics compared to the higher rigidities. We therefore estimated a mean radial and latitudinal gradient for the three low-rigidity measurements by calculating the arithmetic means of the corresponding gradients that use the same PAMELA channel.

4. Conclusions

Our results for the radial and latitudinal gradients for GCR protons during the unusual $A < 0$ solar minimum between solar cycle 23 and 24 are summarized in Table 1 and Fig. 6 (and in more detail in Table A.1).

The radial gradients vary from $G_r = 2.8 \pm 0.2$%/AU for 1.9 GV to $G_r = 3.6 \pm 0.7$%/AU for 0.46 GV, showing values similar to those found in previous studies (Cummings et al. 1987; McKibben et al. 1975; McKibben 1975; Heber et al. 1996b). The values are always positive and show the expected trend of having smaller gradients at higher rigidities. We note that the values agree very well with the one given by Cummings et al. (1987) for the Voyagers.

In agreement with the prediction of calculations solving the Parker transport equation (PTE) for an $A < 0$-solar magnetic epoch, the measured latitudinal gradients are negative (see, e.g., Potgieter et al. 2001, 2014, and references therein), with values from $G_\theta = -0.04 \pm 0.01$%/degree for 1.13 GV and 1.63 GV to $G_\theta = -0.1 \pm 0.03$%/degree for 0.46 GV. In contrast to the radial gradients, the latitudinal gradient for protons is much smaller

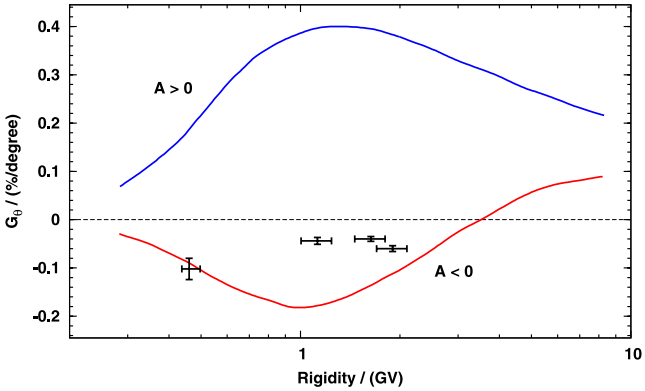

Fig. 7. Computed latitudinal gradients for protons during the last $A > 0$ solar minimum based on *Ulysses*/KET measurements (blue line), and a model prediction for the $A < 0$ solar minimum investigated here (red line) (figure adapted from Potgieter et al. 2001; more details in Burger et al. 2000). The mean latitudinal gradients found in this study are plotted in black.

than the values reported by Cummings et al. (1987) for the last $A < 0$-solar magnetic epoch. The absolute magnitude, however, is smaller for protons above 1 GV and significantly larger for protons below 0.5 GV if compared to *Ulysses*/KET measurements during the declining phase of solar cycle 23 (Fig. 7 in Heber et al. 1996a). Updated data sets and minor changes in the analysis procedures allowed us to obtain slightly larger latitudinal gradients than De Simone et al. (2011), who reported a gradient $G_\theta = -0.024 \pm 0.005$%/deg for ~1.7 GV protons.

Potgieter et al. (2001) performed calculations solving the PTE by adapting the transport parameters in a way that the rigidity dependence of the maximum latitudinal gradient measured by *Ulysses*/KET during the declining phase of solar cycle 23 (Fig. 7 in Heber et al. 1996a) is well reproduced. We note that this measured maximum latitudinal gradient shows the same rigidity dependency as the mean latitudinal gradient with only a constant offset. The results of these calculations are summarized by the blue curve in Fig. 7. Assuming that *Ulysses* were to perform its third orbit under similar conditions as the first orbit but with opposite solar magnetic polarity, the authors found a rigidity dependence of the latitudinal gradient as given by the red curve in Fig. 7. It is important to note that in agreement with our measurements, the predictions give lower values for the $A < 0$-solar magnetic epoch and a maximum of the gradient towards lower rigidities. In contrast to the prediction, this maximum either does not exist or a maximum is present at even lower rigidities. Because the gradients at rigidities above 1 GV do not resemble the predicted rigidity dependence, it seems to us unlikely that the gradient may become positive at even higher values.

Since the very local interstellar spectrum has been determined by recent Voyager, PAMELA, and AMS observations (Potgieter et al. 2014), the results reported here are crucial for evaluating the transport parameters in the heliosphere.

Acknowledgements. The *Ulysses*/KET project is supported under Grant 50 OC 1302 by the German Bundesministerium für Wirtschaft through the Deutsches Zentrum für Luft- und Raumfahrt (DLR). PAMELA proton data obtained via the web site http://tools.asdc.asi.it/cosmicRays.jsp from the Italian Space Agency (ASI) Science Data Center. *Ulysses* and PAMELA orbit data obtained via the web site http://omniweb.gsfc.nasa.gov/coho/helios/heli.html from NASA's Space Physics Data Facility (SPDF). We acknowledge the NMDB database (www.nmdb.eu), founded under the European Union's FP7 program (contract no. 213007) for providing the Kiel neutron monitor data. Sunspot number data used in this study was obtained via the web site http://sidc.be/sunspot-data/ courtesy of the SIDC-team, World Data Center for the Sunspot Index, Royal Observatory of Belgium. Wilcox Solar Observatory data used in this study was obtained via the web site http://wso.stanford.edu courtesy of J. T. Hoeksema.

References

Adriani, O., Barbarino, G. C., Bazilevskaya, G. A., et al. 2013, ApJ, 765, 91
Bastian, T. S., McKibben, R. B., Pyle, K. R., & Simpson, J. A. 1980, Int. Cosmic Ray Conf., 12, 318
Burger, R. A., Potgieter, M. S., & Heber, B. 2000, J. Geophys. Res., 105, 27447
Cummings, A. C., Stone, E. C., & Webber, W. R. 1987, Geophys. Res. Lett., 14, 174
Cummings, A. C., Tranquille, C., Marsden, R. G., Mewaldt, R. A., & Stone, E. C. 2009, Geophys. Res. Lett., 36, 18103
De Simone, N., Di Felice, V., Gieseler, J., et al. 2011, Astrophys. Space Sci. Trans., 7, 425
Heber, B., Dröge, W., Ferrando, P., et al. 1996a, A&A, 316, 538
Heber, B., Dröge, W., Kunow, H., et al. 1996b, Geophys. Res. Lett., 23, 1513
Heber, B., Fichtner, H., & Scherer, K. 2006, Space Sci. Rev., 125, 81
Herbst, K., Heber, B., Kopp, A., Sternal, O., & Steinhilber, F. 2012, ApJ, 761, 17
Krimigis, S. M., Decker, R. B., Roelof, E. C., et al. 2013, Science, 341, 144
McDonald, F. B., Ferrando, P., Heber, B., et al. 1997, J. Geophys. Res., 102, 4643
McKibben, R. B. 1975, Rev. Geophys. Space Phys., 13, 1088
McKibben, R. B. 1989, J. Geophys. Res., 94, 17021
McKibben, R. B., Pyle, K. R., Simpson, J. A., Tuzzolino, A. J., & Ogallagher, J. J. 1975, Int. Cosmic Ray Conf., 4, 1512
McKibben, R. B., Pyle, K. R., & Simpson, J. A. 1979, ApJ, 227, L147
Paizis, C., Heber, B., Raviart, A., et al. 1995, Int. Cosmic Ray Conf., 4, 756
Picozza, P., Galper, A. M., Castellini, G., et al. 2007, Astropart. Phys., 27, 296
Potgieter, M. S., Burger, R. A., & Ferreira, S. E. S. 2001, Space Sci. Rev., 97, 295
Potgieter, M. S., Vos, E. E., Boezio, M., et al. 2014, Sol. Phys., 289, 391
Press, W. H., Teukolsky, S. A., Vetterling, W. T., & Flannery, B. P. 1996, Numerical Recipes in Fortran 90, 2nd edn.: The Art of Parallel Scientific Computing (New York, NY, USA: Cambridge University Press)
Scherer, K., Fichtner, H., Strauss, R. D., et al. 2011, ApJ, 735, 128
Simpson, J. A., Anglin, J. D., Balogh, A., et al. 1992, A&AS, 92, 365
Simpson, J. A., Zhang, M., & Bame, S. 1996, ApJ, 465, L69
Stone, E. C., Cummings, A. C., McDonald, F. B., et al. 2013, Science, 341, 150
Strauss, R. D., Potgieter, M. S., Ferreira, S. E. S., Fichtner, H., & Scherer, K. 2013, ApJ, 765, L18

Appendix A: Detailed gradient results

Table A.1. Detailed gradient results for different selection criteria and fit methods, respectively.

$\langle R_U \rangle$	$\langle R_P \rangle$		All data		Slow ascent (green)		Slow descent (blue)	
			Fit (1)	Fit (2)	Fit (1)	Fit (2)	Fit (1)	Fit (2)
0.45	0.44							
		G_r =	3.8 ± 0.7	3.3 ± 0.9	5.4 ± 1.5	3.5 ± 2.2	3.5 ± 0.7	3.2 ± 0.9
		G_θ =	−0.17 ± 0.02	−0.14 ± 0.03	−0.17 ± 0.04	−0.13 ± 0.07	−0.17 ± 0.03	−0.14 ± 0.04
		χ^2/ndf =	0.8	0.7	0.5	0.4	1.	1.
0.45	0.46							
		G_r =	3.9 ± 0.6	3.9 ± 0.8	4.2 ± 1.2	3.6 ± 1.9	3.8 ± 0.6	3.9 ± 0.8
		G_θ =	−0.01 ± 0.02	−0.09 ± 0.03	−0.09 ± 0.04	−0.08 ± 0.06	−0.1 ± 0.03	−0.09 ± 0.04
		χ^2/ndf =	0.6	0.6	0.3	0.2	0.9	0.9
0.46	0.46							
		G_r =	4.4 ± 0.5	4.4 ± 0.8	4.4 ± 1.2	3.8 ± 2.	4.3 ± 0.6	4.5 ± 0.8
		G_θ =	−0.09 ± 0.02	−0.09 ± 0.03	−0.09 ± 0.04	−0.08 ± 0.06	−0.1 ± 0.02	−0.09 ± 0.04
		χ^2/ndf =	0.8	0.8	0.3	0.3	1.2	1.2
0.49	0.46							
		G_r =	2.3 ± 0.6	2.8 ± 0.8	2.5 ± 1.3	2.8 ± 2.1	2.4 ± 0.6	2.8 ± 0.9
		G_θ =	−0.12 ± 0.02	−0.13 ± 0.03	−0.13 ± 0.04	−0.14 ± 0.06	−0.13 ± 0.03	−0.13 ± 0.04
		χ^2/ndf =	0.8	0.8	0.3	0.3	1.2	1.1
0.49	0.49							
		G_r =	1.6 ± 0.6	2.7 ± 0.8	1.8 ± 1.3	2.9 ± 2.	1.6 ± 0.6	2.7 ± 0.9
		G_θ =	−0.09 ± 0.02	−0.12 ± 0.03	−0.11 ± 0.04	−0.14 ± 0.06	−0.10 ± 0.03	−0.12 ± 0.04
		χ^2/ndf =	1.1	1.	0.6	0.6	1.5	1.4
1.13	1.11							
		G_r =	3.5 ± 0.3	3.2 ± 0.2	4.9 ± 0.4	5.3 ± 0.6	3.2 ± 0.2	2.8 ± 0.3
		G_θ =	−0.06 ± 0.01	−0.03 ± 0.01	−0.04 ± 0.01	−0.05 ± 0.02	−0.06 ± 0.01	−0.05 ± 0.01
		χ^2/ndf =	5.3	5.	1.8	1.8	5.	4.8
1.63	1.61							
		G_r =	3.3 ± 0.2	3.2 ± 0.2	2.2 ± 0.3	2.2 ± 0.4	3.6 ± 0.2	3.4 ± 0.2
		G_θ =	−0.04 ± 0.01	−0.04 ± 0.01	−0.03 ± 0.01	−0.03 ± 0.02	−0.04 ± 0.01	−0.03 ± 0.01
		χ^2/ndf =	5.1	4.9	3.6	3.6	5.7	5.7
1.90	1.85							
		G_r =	2.8 ± 0.2	2.7 ± 0.2	2.1 ± 0.3	2.3 ± 0.4	3.1 ± 0.2	2.7 ± 0.2
		G_θ =	−0.06 ± 0.01	−0.06 ± 0.01	−0.06 ± 0.01	−0.06 ± 0.02	−0.05 ± 0.01	−0.04 ± 0.01
		χ^2/ndf =	4.5	4.4	3.7	3.7	4.5	4.2
0.46[†]	0.46							
		G_r =	3.5 ± 0.6	3.7 ± 0.8	3.7 ± 1.3	3.4 ± 2.	3.5 ± 0.6	3.7 ± 0.9
		G_θ =	−0.1 ± 0.02	−0.10 ± 0.03	−0.11 ± 0.04	−0.10 ± 0.06	−0.11 ± 0.03	−0.10 ± 0.04

Notes. Proton mean rigidities $\langle R_U \rangle$ and $\langle R_P \rangle$ (both in GV) as measured by *Ulysses*/KET and PAMELA, respectively, that are used to calculate the corresponding gradients. Radial and latitudinal gradients (in %/AU and %/degree, respectively), and quality of fit for different selection criteria (cf. Fig. 2) and fit methods. Indicated by (1) are the values obtained by the bootstrap Monte Carlo approach; while (2) marks the fit routine using the `fitexy` algorithm. [(†)] Note that each gradient in the last row is calculated by the arithmetic mean of the corresponding gradients of rows 2, 3, and 4 (see Sect. 3.2 for details).

Unfortunately, since the end of the Ulysses mission in mid-2009 we lack a spacecraft varying significantly in latitude and measuring the GCRs of interest. Spatial gradients of GCR proton and helium were determined over various phases of the Ulysses mission. However, electron gradients have not been investigated that much, and if so, often only indirectly using the electron-to-proton ratio (e.g. Heber et al. 2008, see Sect. 3.1). Because PAMELA is measuring electrons in the same energy range as the KET onboard Ulysses, it should be possible to directly derive their gradients with the same routine presented in the last section. However, there are some pitfalls. First of all, PAMELA electron observations are so far only available for accumulated measurement intervals of six months or more for the time period from 2006 to 2010 (Adriani et al., 2015). During such a period, Ulysses is varying too much in latitude to obtain significant results, especially during its Fast Latitude Scans (FLS). This can already be seen for example in Fig. 3 in Sect. 3.4.3. The ranges of values covered by the data points are already for these monthly intervals quite large. Another problem is the fact that the electron measurements of Ulysses/KET have to be used with care only. Their instrumental response is more complex as for example that of protons, thus, there are only a few publications with selected electron intensities available. Additionally, in contrast to PAMELA Ulysses/KET cannot distinguish between electrons and positrons, and is only measuring the summed count rate of both. Depending on energy and time, the positron fraction ($e^+/(e^+ + e^-)$) can be above 15% (Adriani et al., 2016), thus altering the results. Note that for Ulysses/KET the inseparability of protons and antiprotons is also valid. However, due to the extreme low fraction of antiprotons (Aguilar et al., 2016), this effect is negligible.

4 CHARGE-SIGN DEPENDENCE OF GCR MODULATION

The charge-sign dependence of the solar modulation of GCRs has already been introduced in Sects. 1.3 and 3. Its effect on the time profile of positively charged GCRs can be seen in Fig. 3 with peaked maxima during $A < 0$ (around 1987 and 2010) and plateau-like maxima during $A > 0$ solar minima (around 1976 and 1997), respectively. For negatively charged GCRs, predominantly electrons, the behavior is expected to be interchanged (e.g. Ferreira et al., 2003). This 22-year cycle is attributed to the changing solar magnetic field polarity and its influence on drift processes, which are the only drivers in the Paker equation (Eq. 1 Parker, 1965) that show a polarity dependence. This allows to gain further insights on the solar modulation of GCRs by comparing different-polarity measurements at the same rigidity.

In the following publication (Heber et al., 2009) this has been carried out during the two consecutive $A < 0$ solar minima in the 1980s and 2000s. For the first period, 1.2 GV electron and helium measurements at Earth from the International Sun-Earth Explorer 3/International Cometary Explorer (ISEE 3/ICE) and IMP-8 were utilized, respectively. The second solar minimum was investigated using 2.5 GV electron and proton measurements by Ulysses/KET. Due to its peculiar orbit (cf. Chap. 3 and Fig. 10), the latter observations have been corrected for radial and latitudinal gradients, using, among others, the results from Heber et al. (2008) presented in Sect. 3.1. By comparing the behavior of oppositely charged GCR particles in the two same-polarity solar minima together with measurements of the strength of the HMF and the tilt angle (cf. Sect. 1.3), the importance of the different modulation processes during the so-called unusual solar minimum in the late 2000s (e.g. Chowdhury et al., 2016; Potgieter, 2017, and references therein) was analyzed. This led to the conclusion that the tilt angle around 2009 was still at unusual high values, resulting in gradient and curvature drifts to prevent proton intensities to rise as much as expected in comparison with previous and same-rigidity electron observations. Based on this the prediction was made that if the tilt angle drops to common solar minimum values, due to the weak HMF the proton intensities would reach record setting values – which was later confirmed (e.g. Mewaldt et al., 2010; Adriani et al., 2013).

MODULATION OF GALACTIC COSMIC RAY PROTONS AND ELECTRONS DURING AN UNUSUAL SOLAR MINIMUM

Heber, B., A. Kopp, **J. Gieseler**, R. Müller-Mellin, H. Fichtner, K. Scherer, M. S. Potgieter, S. E. S. Ferreira, *Astrophys. J.*, 699, 2, 1956-1963 (2009), DOI:10.1088/0004-637X/699/2/1956. Own contribution: 10%

The Astrophysical Journal, 699:1956–1963, 2009 July 10 doi:10.1088/0004-637X/699/2/1956

MODULATION OF GALACTIC COSMIC RAY PROTONS AND ELECTRONS DURING AN UNUSUAL SOLAR MINIMUM

B. Heber[1], A. Kopp[1], J. Gieseler[1], R. Müller-Mellin[1], H. Fichtner[2], K. Scherer[2], M. S. Potgieter[3], and S. E. S. Ferreira[3]
[1] Institut für Experimentelle und Angewandte Physik, Christian-Albrechts-Universität zu Kiel, 24118 Kiel, Germany; heber@physik.uni-kiel.de
[2] Theoretische Physik IV, Ruhr-Universität Bochum, Bochum, Germany
[3] Unit for Space Physics, North-West University, 2520 Potchefstroom, South Africa
Received 2009 January 18; accepted 2009 May 6; published 2009 June 26

ABSTRACT

During the latest *Ulysses* out-of-ecliptic orbit the solar wind density, pressure, and magnetic field strength have been the lowest ever observed in the history of space exploration. Since cosmic ray particles respond to the heliospheric magnetic field in the expanding solar wind and its turbulence, the weak heliospheric magnetic field as well as the low plasma density and pressure are expected to cause the smallest modulation since the 1970s. In contrast to this expectation, the galactic cosmic ray (GCR) proton flux at 2.5 GV measured by *Ulysses* in 2008 does not exceed the one observed in the 1990s significantly, while the 2.5 GV GCR electron intensity exceeds the one measured during the 1990s by 30%–40%. At true solar minimum conditions, however, the intensities of both electrons and protons are expected to be the same. In contrast to the 1987 solar minimum, the tilt angle of the solar magnetic field has remained at about 30° in 2008. In order to compare the *Ulysses* measurements during the 2000 solar magnetic epoch with those obtained 20 years ago, the former have been corrected for the spacecraft trajectory using latitudinal gradients of 0.25% deg^{-1} and 0.19% deg^{-1} for protons and electrons, respectively, and a radial gradient of 3% AU^{-1}. In 2008 and 1987, solar activity, as indicated by the sunspot number, was low. Thus, our observations confirm the prediction of modulation models that current sheet and gradient drifts prevent the GCR flux to rise to typical solar minimum values. In addition, measurements of electrons and protons allow us to predict that the 2.5 GV GCR proton intensity will increase by a factor of 1.3 if the tilt angle reaches values below 10°.

Key words: cosmic rays – interplanetary medium – Sun: magnetic fields

Online-only material: color figures

1. INTRODUCTION

The intensity of galactic cosmic rays (GCRs) is modulated as they traverse the turbulent magnetic field embedded into the solar wind. Figure 1 displays in the upper panel the time history of the GCR intensity as measured by the Oulu neutron monitor since 1964. The lower panel shows the monthly averaged sunspot number during the same time period. Already a simple inspection of Figure 1 shows the well known anti-correlation between the sunspot number and the cosmic ray intensity. Since these particles are scattered by irregularities in the heliospheric magnetic field and undergo convection and adiabatic deceleration in the expanding solar wind, changes in the heliospheric conditions, as imprinted by the Sun's activity, will obviously lead to the observed overall variation in GCR intensities. Jokipii et al. (1977) pointed out that gradient and curvature drifts in the large-scale heliospheric magnetic field, approximated by a three-dimensional Archimedean spiral (Parker 1958), should also be an important element of cosmic ray modulation. In a so-called $A < 0$ magnetic epoch like in the 1960s, 1980s, and 2000s a more peaked time profile for positively charged particles is expected compared with an $A > 0$ solar magnetic epoch like in the 1970s and 1990s. During the $A > 0$ solar magnetic epoch the magnetic field is pointing outward over the northern and inward over the southern hemisphere, and positively charged particles drift into the inner heliosphere over the poles and out of it along the heliospheric current sheet (HCS). The maximum latitudinal extent of the HCS with the inclination or tilt angle α has been calculated by Hoeksema (1995) by using two different magnetic field models. (1) The "classical" model uses a line-of-sight boundary condition at the photosphere. (2) The newer model uses a radial boundary condition at the photosphere and has a higher source surface radius (3.25 compared with 2 solar radii). Ferreira & Potgieter (2004) could demonstrate that the tilt angle corresponding to the classical model is a better modulation parameter for periods of decreasing solar activity as being investigated in this work, so that we will use the classical model in the following.

The time-dependent cosmic ray transport equation derived by Parker (1965) has been solved numerically with increasing sophistication and complexity (Jokipii & Kóta 1995; Burger et al. 2000; Ferreira & Potgieter 2004; Scherer & Ferreira 2005; Alanko-Huotari et al. 2007). The intensity profile as a function of the tilt angle α is displayed in Figure 2 (left) for positively charged particles for three different energies (Potgieter et al. 2001). As expected, the intensity is sensitive to the variation of the tilt angle α in an $A < 0$ solar magnetic epoch if α is low. In contrast, in an $A > 0$ solar magnetic epoch it becomes sensitive to α above a threshold of about 60°. These models also predict that the intensity around solar minimum, when the tilt angle is small, for high energies is higher during the $A < 0$ than during the $A > 0$ magnetic epochs (see the upper panel of Figure 2 (left)). The opposite is true at higher tilt angles and lower energies. Note that similar tilt dependences are observed when using different ions (α particles) than proton and rigidity instead of the kinetic energy (Webber et al. 2005).

These predictions from the propagation models including drifts have been proven to be correct when simultaneous measurements of GCR electrons and helium became available in the 1980s for solar cycle 21. The intensity time profiles of 1.2 GV electrons (red curve) and 1.2 GV helium

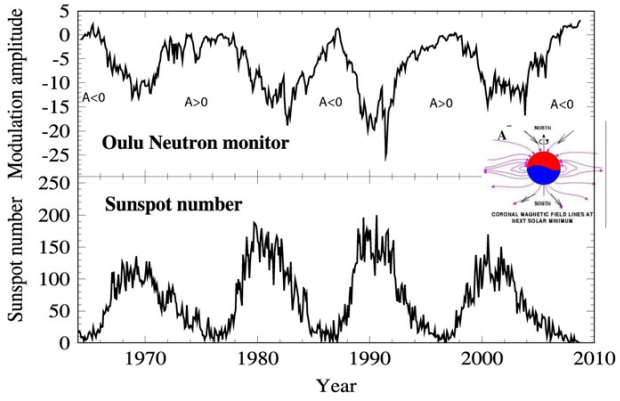

Figure 1. GCR intensity variation as measured by the Oulu neutron monitor (upper panel). The sunspot number is displayed in the lower panel of the figure (SIDC Team 2009, http://sidc.oma.be). From that figure it is evident that the intensities of GCRs and solar activity are anticorrelated. The inset sketches the Sun's magnetic field configuration during an $A < 0$ solar magnetic epoch.

(A color version of this figure is available in the online journal.)

(black curve) for 1980s solar cycle are displayed in the upper panel of Figure 2 (right). The helium and electron measurements are from the MEH (Meyer et al. 1978) and Goddard Medium Energy Experiment (GME; http://spdf.gsfc.nasa.gov/imp8_GME/GME_instrument.html) aboard *ICE* and *IMP-8*, respectively. While the electrons recovered to solar minimum values in 1986, the helium intensity increased until 1987 and decreased with solar activity, as shown in the lower panel, where sunspot number and tilt angle α are displayed. Because electrons drift for $A < 0$ into the inner heliosphere over the poles and out along the HCS, they do not experience variations in α when the latter is below $\sim 25^\circ$ (Heber et al. 2002). Since all other propagation parameters are independent of the charge of the particles, the differences in the time profiles of two consecutive solar cycles with opposing polarities can be attributed to charge-dependent drifts. In the 1990s $A > 0$ solar magnetic epoch, similar measurements have been reported (Heber et al. 2002).

The current solar minimum is remarkable in many ways. Recently, both the *Ulysses* Team observing the solar wind as well as the radio wave instrument team reported the lowest solar wind densities ever measured (McComas et al. 2008; Issautier et al. 2008). In addition, the magnetic field strength was found to be lower than in the previous solar minimum (Smith & Balogh 2008). Although the sunspot number has been decreasing over the last three years, Figure 1 shows that the GCR intensities do not rise as steep as expected. In order to interpret this "unusual" modulation, we investigate the GCR intensity time profiles of protons and electrons simultaneously during the current solar minimum using *Ulysses* Cosmic ray and Solar Particle INvestigation/Kiel Electron Telescope (COSPIN/KET) data and compare it with the observations during the 1980s solar cycle.

2. INSTRUMENTATION AND OBSERVATIONS

Ulysses was launched on 1990 October 6, closely before the declining activity phase of solar cycle 22. A swing-by maneuver at Jupiter in 1992 February placed the spacecraft into a trajectory inclined by 80° with respect to the ecliptic plane (Wenzel et al. 1992). Since then the spacecraft is orbiting the Sun with an inclination of about 80.2. The radial distance and heliographic latitude of the spacecraft are shown in the lower panel of Figure 3. From late 1990 to early 1992 the radial distance r to the Sun is increasing from 1 AU to 5.3 AU while the heliographic latitude ϑ is lower than 10°. After the swing by at Jupiter r is again decreasing while ϑ is increasing. *Ulysses* reached its highest heliographic latitude of 80.2 south in 1994 September. Within one year the spacecraft scanned the region from highest southern to northern latitudes and was at 80.2 north in 1995 August. These so-called fast latitude scans have since then repeated from 2000 to 2001 and 2006 to 2007 and are marked by shadings in Figure 3.

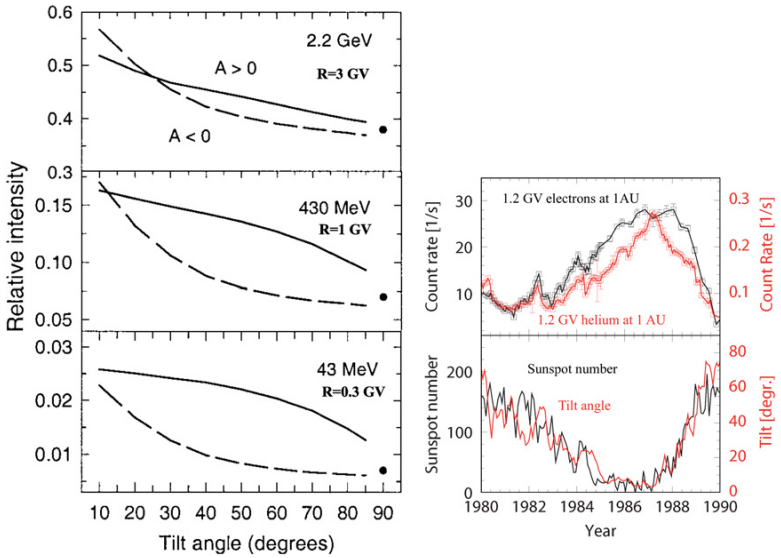

Figure 2. Left: cosmic ray proton intensities at Earth as a function of tilt angle at 2.2 GeV, 430 MeV, and 43 MeV, computed with a steady-state drift model for $A > 0$ (solid lines) and $A < 0$ (dashed lines) cycles, respectively (Potgieter et al. 2001). Right: 26-day averaged count rates of 1.2 GV GCR electrons from the MEH experiment onboard *ICE* (black curve) and helium from the GME (red curve) aboard *IMP-8* from 1980 to 1990. The sunspot number (black) and the tilt angle (red) of the solar magnetic field are displayed in the lower panel of the figure.

(A color version of this figure is available in the online journal.)

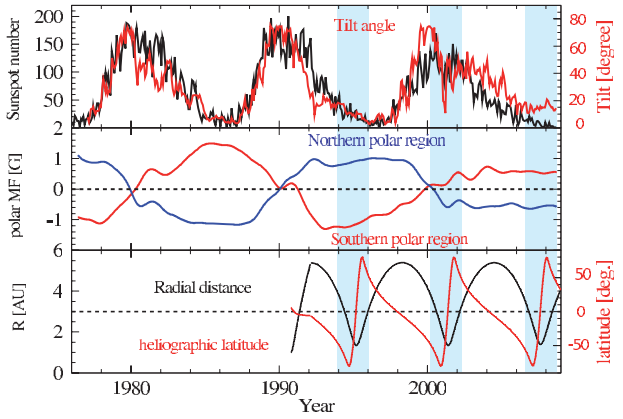

Figure 3. From top to bottom are shown the sunspot number, tilt angle α, the solar polar magnetic field strength of the northern and southern polar cap, and the radial distance and heliographic latitude of *Ulysses*. Marked by shading are the three *Ulysses* fast latitude scans. The first and third one took place at solar minimum and the second one under solar maximum conditions.

(A color version of this figure is available in the online journal.)

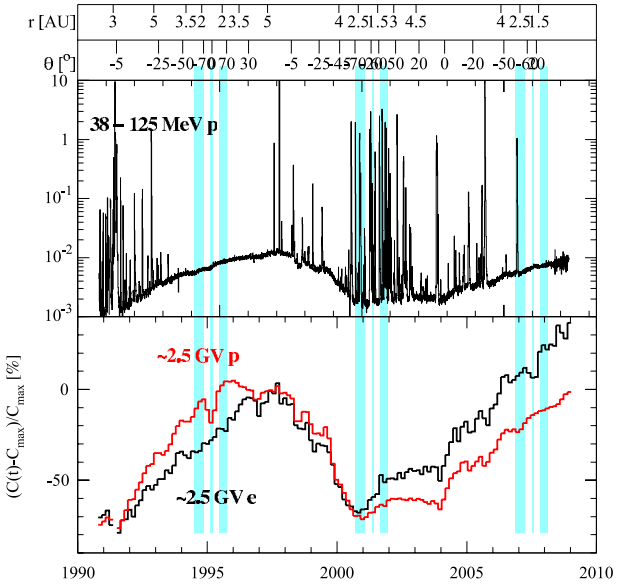

Figure 4. From top to bottom are shown the daily averaged count rates of 38–125 MeV protons from 1990 to 2009 and the 52-day averaged quiet time count rates, given as percental changes, of ~2.5 GV electrons and protons (red curve). *Ulysses* radial distance and heliographic latitude are shown on top. Marked by shadings are the three fast latitude scans as defined in Figure 3.

(A color version of this figure is available in the online journal.)

The upper two panels display the sunspot number (black curve) together with the tilt angle α of the HCS (red curve) and the solar polar magnetic field strength over the northern (blue curve) and southern (red curve) polar regions of the Sun. In the 1990s the field strength is positive over the northern and negative over the southern polar regions and vice versa in the 1980s and 2000s. Thus, *Ulysses* first and third fast latitude scans took place at solar minimum conditions during $A > 0$ and $A < 0$ solar magnetic epochs, respectively.

According to the in situ measurements the absolute magnetic polar field strengths were by a factor of 1.5 (north) and 2.2 (south) larger in 1994/1995 compared with 2006/2007. The second fast latitude scan took place during solar maximum when the sunspot number and tilt angle were high and the magnetic field strength over both poles was close to 0.

The observations were made with the KET aboard *Ulysses*. It measures protons and helium in the energy range from 6 MeV nucleon^{-1} to above 2 GeV nucleon^{-1} and electrons in the energy range from 3 MeV to a few GeV (Simpson et al. 1992). The following three particle channels from the KET will be used in this paper.

1. Protons from 0.038 to 0.125 GeV (0.194–0.367 GV).
2. Electrons from 0.9 to 4.6 GeV (0.9–4.6 GV).
3. Protons from 0.25 to 2 GeV (0.549–2.43 GV).

The latter two channels roughly correspond to the same average characteristic rigidity (cf. Rastoin 1995, and values in brackets above) and will be abbreviated as "2.5 GV electrons" and "2.5 GV protons" (see also Heber et al. 1999).

Thus, when comparing *Ulysses* GCR measurements with those in the 1980s (see Figure 1) we need to take into account that

1. KET measurements have to be corrected for a radial gradient and possible latitudinal gradient,
2. due to the reduced data coverage in 2008 the statistics in the 1.2 GV electron channel is low. Since the 2.5 GV electron channel corresponds to a broad energy range, we will use this channel.

Figure 4 shows *Ulysses* daily averaged count rates of 38–125 MeV protons (top panel), and 52 day averaged quiet time variation of the count rates of ~2.5 GV protons (black curve) together with those of 2.5 GV electrons (red curve) from 1990 November to 2008 December. The latter two are presented as percental changes with respect to the rates C_m, 0.36 counts s^{-1} for protons and 6.9×10^{-4} counts s^{-1} for electrons, measured in mid-1997 at solar minimum, $(C(t) - C_m)/C_m$. Quiet time profiles have been determined by using only time periods in which the 38–125 MeV proton channel showed no contribution of solar or heliospheric particles (Heber et al. 1999). The observed variations in the 2.5 GV particle intensity are caused by temporal as well as spatial variations due to *Ulysses*' trajectory. Thus, before discussing the significance of the temporal variation in Figure 4 in detail it is important to understand the role of spatial variations along the *Ulysses* trajectory. Marked by shadings are again the three different fast latitude scans. These periods will be discussed in more detail in the following section.

3. DATA ANALYSIS

The changes caused by solar activity, latitude, and radial distance presented in Figure 4 do not occur in phase, the *Ulysses* observation will allow us to draw conclusions about the differences in the time profiles of electrons and protons.

Radial gradients. We have shown in previous studies (Heber et al. 1996, 1999, 2002, 2008; Clem et al. 2002; Gieseler et al. 2007) that we can determine mean latitudinal and radial gradients of protons and electrons by either comparing with Earth orbiting experiments or investigating of the electron-to-proton ratio.

1. The radial proton gradient varies from about 2.2% AU^{-1} for the period up to early 1998 to 3.5% AU^{-1} thereafter (Heber et al. 2002).
2. The radial for electrons and protons has been nearly the same from 1992 to 1994 (Clem et al. 2002).

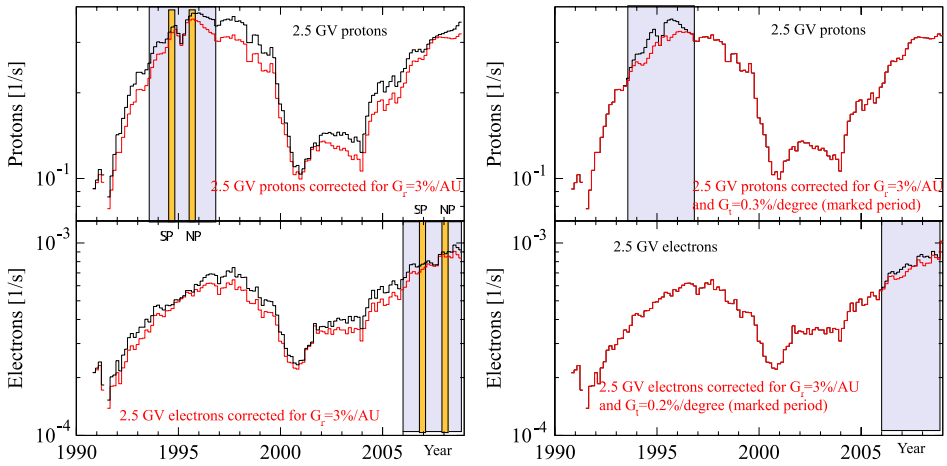

Figure 5. Upper and lower panels display 52 day averaged quiet time count rates of 2.5 GV protons and electrons, respectively. The left panels show the uncorrected data (black curves) and those corrected by the radial variation of *Ulysses* with a radial gradient of 3% AU^{-1} (red curve). The right panels show the latter curves (red, becoming black within the shadings) together with (red curves within the shadings) the count rates being additionally corrected by the latitudinal variation of the spacecraft with latitudinal gradients of 0.3% deg^{-1} and 0.2% deg^{-1} for protons and electrons (Heber et al. 1996, 2002, 2008). Marked by blue shading are the two *Ulysses* solar minimum latitude scans, the yellow shading within these regions indicate time periods in which the count rates show dependences on latitude.

(A color version of this figure is available in the online journal.)

We assume that at a given time the radial gradients of 2.5 GV electrons and protons are approximately the same. Since Chen & Bieber (1993) have shown for GV protons that there is no evidence for a strong variation of the radial gradient with solar magnetic polarity, we will use a mean radial gradient of about $G_r = 3\%$ AU^{-1} for both solar magnetic epochs. Thus, the gradient is somehow over and underestimated during the $A > 0$ and $A < 0$ solar magnetic epochs, respectively. Figure 5(left) displays, in the upper and lower panels, the variation of the 2.5 GV proton and electron count rate. The red curves result from correcting *Ulysses* proton and electron measurements for radial variation with $G_r = 3\%$ AU^{-1}.

Latitudinal gradients. In order to compare the electron with the proton time profiles we have to correct the 2.5 GV proton and electron count rates for latitudinal gradients during the $A > 0$ and $A < 0$ solar magnetic epochs, respectively. While the corrected 2.5 GV proton rates show a clear dependence with latitude from 1993 to 1997 (cf. yellow regions in Figure 5 (left)), no correlation during the 2006–2007 solar minimum fast latitude scan was found (Gieseler et al. 2007; Heber et al. 2008). Electrons in contrast show no variation during the 1994/1995 fast latitude scan but a dependence during that in 2006/2007 as again marked by the yellow regions in Figure 5 (left) (Heber et al. 2008). In previous studies, Belov et al. (2001) and Heber et al. (2002, 2003, 2008) found the following.

1. The variations of the proton intensity with latitude until mid-1999 are consistent with a vanishing latitudinal gradient in the streamer belt and an average gradient of about 0.25% deg^{-1} for latitudes above about $\pm 25^\circ$.
2. In contrast to this behavior the latitudinal gradient decreases markedly to small values after mid-1999, leading to a spherically symmetric intensity distribution around solar maximum conditions and during the $A < 0$ solar magnetic epoch.
3. The variation of the electron intensity with latitude is consistent with a zero latitude gradient until 2003. During the third fast latitude scan Heber et al. (2008) found an average gradient of about 0.19% deg^{-1}.

The time profiles shown in Figure 5 (right) were corrected for a latitudinal gradient $G_t = 0.25\%$ deg^{-1} and $G_t = 0.19\%$ deg^{-1} for protons and electrons, respectively. While the proton gradient has only been applied during the 1990 solar minimum, when the spacecraft was above 25° latitude, the electron gradient was used only during the same conditions in the 2000 solar minimum. Figure 6 shows in the middle panel the radial distance and heliographic latitude of *Ulysses*. The upper and lower panels display the uncorrected and corrected 2.5 GV electron and proton (red curve) variations, respectively. The calculation of these variations will be explained in the next paragraph. However, the figure also gives a summary of our corrections, showing no obvious intensity variation with *Ulysses*' latitude or radius in the lower panel. Like the Oulu neutron monitor (see Figure 1), the recent recovery toward solar minimum values occurred in four modulation steps: the increase in the GCR intensities starts after the solar activity period in October to 2003 November (Klassen et al. 2005) and reaches again a plateau in late 2004 before the ground level event in 2005 January (Simnett 2006). Similar step-like time profiles were observed in 2005 and 2007. Therefore, the corrected proton and electron fluxes as derived in this section will be referenced as the "1 AU equivalent" count rate.

Temporal modulation. The third panel of Figure 6 shows the "1 AU equivalent" normalized count rates of 2.5 GV electrons (black curve) and protons (red curve). The "1 AU equivalent" normalized count rate $\xi(t)$ and modulation amplitudes ζ are given by the expressions

$$\xi(t) = \frac{C(t) - C_{\min}}{C_{\min}} \text{ and} \tag{1}$$

$$\zeta = \frac{C_{\max} - C_{\min}}{C_{\min}}, \text{ respectively,} \tag{2}$$

where $C(t)$, $C_{\min}$, and $C_{\max}$ are the count rates being time averaged over 52 days at time t, the periods of solar minimum and maximum as defined below, respectively. Thus, the modulation amplitude for the two solar minima and maxima have

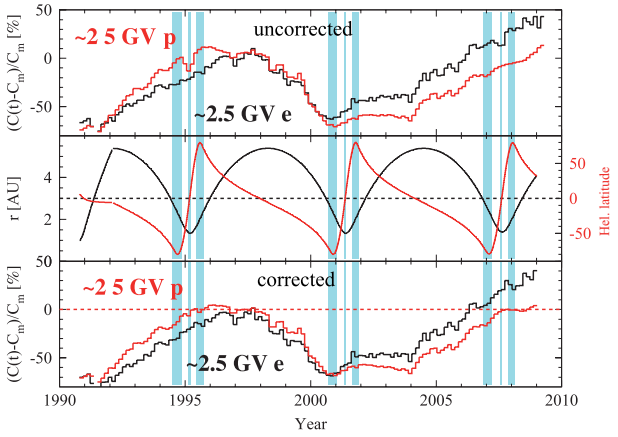

Figure 6. Top and bottom panels display the 52-day averaged quiet time uncorrected (top) and corrected 2.5 GV electrons (black) and proton count rates (red) from Figure 5. The middle panel shows the radial distance (black) and the latitude (red) of *Ulysses*.

(A color version of this figure is available in the online journal.)

been determined by

$$\zeta_{+}^{(1)} = \frac{(C_{2000} - C_{1997})}{C_{1997}}, \tag{3}$$

$$\zeta_{+}^{(2)} = \frac{(C_{1990} - C_{1997})}{C_{1997}}, \tag{4}$$

$$\zeta_{-} = \frac{(C_{2000} - C_{2008})}{C_{2008}}. \tag{5}$$

For the time periods we choose C_{1990} from day of year (DOY) 300 1990 to DOY 35 1991, C_{1997} from DOY 43 1997 to DOY 243 1997, C_{2000} from DOY 198 2000 to DOY 348 2000, and C_{2008} from DOY 26 2008 to DOY 226 2008. Although these periods are chosen somehow arbitrarily, the uncertainty of the values summarized in Table 1 is less than 5% when using fits to the data for slightly different time intervals. During the $A > 0$ solar magnetic epochs the modulation amplitudes are larger for protons (70% and 67%) than for electrons (64% and 62%). The difference is, however, larger than expected from the calculation, presented in Figure 2 (left). The reason for this discrepancy is the count rate of electrons in 1997. Heber et al. (1999) showed in their Figure 3 that electrons increased for only short periods in 1997 to solar minimum values. When we normalize the electrons to this time period, values of 69% and 67% are found. These values are given in brackets in Table 1. Thus, the electron amplitude and the proton amplitude become the same as predicted by modulation models (Potgieter et al. 2001).

In contrast to the last solar minima in 1987 (see Figure 2 (right)) and 1996/1997 protons and electrons are not recovering to the same values by the end of 2008. Not only does the intensity of 2.5 GV electrons exceed the proton intensity by about 30%, but also the "1 AU equivalent" normalized electron count rate is exceeding the 1997 value by approximately the same amount. In what follows, we show that this observation can be interpreted in the context of the compound model by Ferreira & Potgieter (2004) using a complex dependence of the diffusion tensor and the drift term on the heliospheric field strength and the tilt angle of the HCS.

Table 1
Modulation Amplitude for Protons and Electrons with Mean Rigidities of 2.5 GV

Period	Amplitude Protons (%)	Amplitude Electrons (%)
$\zeta_{+}^{(1)}$	70	64 (69)
$\zeta_{+}^{(2)}$	67	62 (67)
ζ_{-}	70	92

Notes. The number in brackets are the result when using a shorter period in 1997 as reference. For details see the text.

4. DISCUSSION

By solving Parker's transport equation numerically, Potgieter & Ferreira (2001) and Ferreira & Potgieter (2004) showed that the variation in the GCR intensity can be described by a diffusion coefficient along the heliospheric magnetic field which varies as

$$\kappa_{\parallel} \propto \frac{B_0}{B(t)^{n(\alpha,P)}}, \tag{6}$$

with $n(\alpha, P)$ being a number depending on the particle rigidity P (momentum per charge) and the tilt angle α (Potgieter & Ferreira 2001; Ferreira & Potgieter 2004), $B(t)$ and B_0 the magnetic field strength at time t and at solar minimum, respectively. $n(\alpha, P) = \alpha(t)/\alpha_0$ where $\alpha(t)$ is the observed time-varying tilt angle and α_0 is a "constant" for a given rigidity. The results from Potgieter & Ferreira (2001) and Ferreira & Potgieter (2004) are presented in Figure 7. The Figure demonstrates that a good reproduction of the 22 year cycle for 1.2 GV helium and electrons could be achieved for α_0 between 7° and 15°. Note that, as described in Ferreira & Potgieter (2004), the tilt is propagated out into the heliosphere with a solar wind velocity of 400 km s^{-1} and that using α as a time-dependent factor in the exponent of n, modulation barriers are taken into account. For $\kappa_{\perp}$ the same values have been used as in Ferreira & Potgieter (2004). However, at neutron monitor rigidities the authors could demonstrate that in agreement with Wibberenz et al. (2002) n becomes 1. In addition to the model used by Wibberenz et al. (2002), the models by Ferreira & Potgieter (2004), Ferreira & Scherer (2006), and Ferreira et al. (2008a, 2008b) take into account drifts and are therefore better suited to describe the particle transport in the heliosphere around solar minimum conditions.

In Figure 8, we compare the normalized count rates of 1.2 GV electrons and helium for the 1980s $A < 0$ solar magnetic epoch (left) with the "1 AU equivalent" normalized 2.5 GV electron and proton count rate (right) during the 2000s $A < 0$ solar magnetic epoch. 1.2 GV particles have been normalized by using values (0.2 counts s^{-1} for helium and 20 counts s^{-1} for electrons) so that the solar maximum value in 1991 reached −70% (not shown here). Using this normalization, the count rates of both helium and electrons reach a value of 35%–40% in 1986. During the same time the heliospheric field strength decreased from about 8 nT around solar maximum to 5 nT at solar minimum. While the tilt angle α was below 10° from 1985 to 1987, the electron count rate was more or less constant and the helium count rate increased from 0% to 30% from 1986 to 1987, only. Solar activity increased again in early 1987 with first the tilt angle increasing to values of 25°–30° in 1988. In agreement with the model calculation by Ferreira & Potgieter (2004) the normalized count rate of helium decreased again to 0%. Later, both the heliospheric magnetic field strength and the

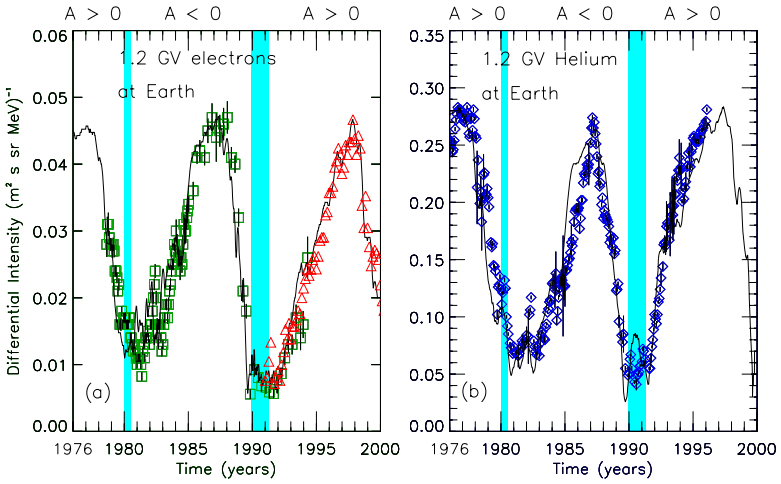

Figure 7. Charge-sign-dependent simulation over two solar cycles using the compound model from Ferreira & Potgieter (2004). Left: computed 1.2 GV electron intensity at Earth compared with observations from *ISEE 3/ICE* (Clem et al. 2002) and *Ulysses* (Heber et al. 2003). Right: computed 1.2 GV helium intensity at Earth compared with *IMP-8* measurements (McDonald et al. 1998).

(A color version of this figure is available in the online journal.)

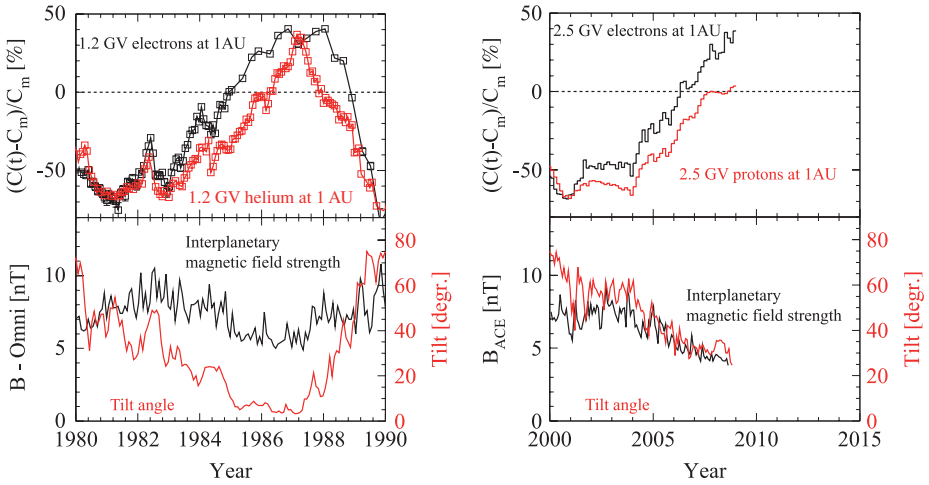

Figure 8. Left: long-term averaged normalized count rates of 1.2 GV GCR electrons (black curve) and helium (red curve) from 1980 to 1990. The count rates have been normalized so that a value of −70% are determined in 1991 (not shown here). Right: 56 day averaged normalized count rates of 2.5 GV electrons and protons from 2000 to 2009. The heliospheric magnetic field strength from the Omni tape and the *ACE* spacecraft (Stone et al. 1998) as well as the tilt angle (red curve) are displayed in the lower panels. As discussed in detail by Heber et al. (2002) the tilt angle has been shifted by 78 days in order to account for the time to establish the propagation conditions in the inner heliosphere.

(A color version of this figure is available in the online journal.)

tilt angle increased and also both electrons and helium were decreasing until 1990 when solar maximum was reached.

The right part of Figure 8 shows the same parameters, but 20 years later. As mentioned above, 1.2 GV electrons and helium have been substituted by the "1 AU equivalent" normalized 2.5 GV electron and proton count rate channels due to the low statistics in the 1.2 GV electron channel in 2008. Note that at these slightly higher rigidities the modulation amplitude is expected to become smaller. Thus, the absolute values should not be compared between the two solar cycles. The lower panel displays the long-term averages of the heliospheric magnetic field strength and the tilt angle α. As 20 years ago the heliospheric magnetic field strength B was at about 8 nT around solar maximum. From 2005 onward B decreased to values of about 4 nT, i.e., about 1 nT lower than in 1986. The tilt angle α, however, decreased from about 60° to 30° and reached up to now never a value below 20°. During the same period both proton and electron fluxes increased from −50% and −30% to 0% and 30%, respectively.

Comparing the left part with the right part of Figure 8, it is interesting to note that at the end of 1985 and the beginning of 1986 similar differences have been observed. At that time the tilt angle α was still above 20° and the magnetic field strength around 6–7 nT. The normalized helium and electron count rates reached values of about −35% and 0%, respectively. Due to the decrease in B the normalized count rates of both electrons and helium increased. Since the tilt angle quickly decreased from 25° to values below 10°, the increase was much larger for helium than for electrons, reaching the same values in 1987. Thus, we expect the protons to increase to

the electron level as far as the tilt angle will become lower than 10°. If the heliospheric magnetic field strength will stay around 4 nT we predict that the GCR proton count rate will increase until they reach the same modulation amplitude than the electrons, resulting in a factor of about 1.3. Since no continuous electron measurements at neutron monitor rigidities have been performed, the intensity variation of the Oulu neutron monitor is more difficult to interpret. By the end of 2008 the intensities of the neutron monitor were higher than those during the 1987- and the 1997 solar minima, although the intensities at 2.5 GV reached only the same values than in the latter. However, if we assume that the diffusion coefficient is the same during both solar magnetic epochs, then it is obvious from Figure 3 (left) that with increasing rigidity the tilt angle when the intensities during $A > 0$ equals the intensities during the $A < 0$ solar magnetic epoch moves to higher values. Because the break-even intensity is at about 12° for 1 GV and 25° for 3 GV the intensity for low and high rigidities will be lower and higher when the tilt is between these break-even values. The intensities are in addition depending on the magnetic field strength as discussed above. Thus, the intensities are expected to be larger during the current solar minimum, compared with the other solar minima, as observed by the Oulu neutron monitor. Since no measurements of 2.5 GV are available to us for the 1987 solar minimum, the absolute variation between these cycles should not be compared. Thus, we would expect to observe the highest GCR intensities ever measured in heliospheric space.

5. SUMMARY AND CONCLUSION

Based on COSPIN/KET measurements obtained with *Ulysses* from launch in 1990 October to the end of 2008, we present in this paper electron and proton count rates for a rigidity of ≈2.5 GV. The data set covers the recovery phases of solar cycles 22 and 23 as well as other phases of solar cycle 23. We obtain the "1 AU equivalent" count rates by disentangling variations related to solar activity and the varying radial distance and latitude along the *Ulysses* orbit, using radial and latitudinal gradients determined by Heber et al. (1996, 1999, 2002), Clem et al. (2002), Gieseler et al. (2007), and recently Heber et al. (2008). In detail

1. The radial gradient can be approximated for electrons and protons by about 3% AU^{-1}.
2. The variation of proton intensity with latitude is consistent with a vanishing latitude gradient in the streamer belt and an average gradient of about 0.25% deg^{-1} for latitudes above about ±25° until mid-1999. The latitudinal gradient decreases markedly to small values after mid-1999, leading to a spherically symmetric intensity distribution since then.
3. Based on the observed latitudinal proton intensity variations, the corresponding gradient of electrons could be determined from 2005 to 2008. A gradient of 0.19% deg^{-1} has been applied.

The comparison of the corrected proton count rates with neutron monitor observations resulted in the same modulation features. Thus, the corrected measurements can be used as "1 AU equivalent" electron and proton count rates. Although the sunspot number and the heliospheric magnetic field strength reached solar minimum values in 2008 the count rate of electrons exceeded the proton count rate by about 30%. During the 1980s, when first long-term charge-sign-dependent measurements became available, both electron and proton count rates reached the same level at solar minimum early 1987. In contrast to the period in 2008, the tilt angle, i.e., the maximum latitudinal extent of the HCS, was in 1986 below 10°. This leads us to the conclusion that curvature and gradients drifts, as predicted by Ferreira & Potgieter (2004), prevent the proton count rates to reach real solar minima level, because the particles have to drift into the heliosphere along the HCS, while the electrons already reached their solar minimum intensities. Therefore, the proton intensity is still lower than expected. Another important conclusion for the current solar cycle 23 minimum is that the proton intensity will increase by ∼30% and will reach the highest intensities ever measured in heliospheric space, if the tilt angle will decrease below 10°. This work also shows the importance of simultaneous measurements of protons and electrons in order to understand the modulation of GCRs in the heliosphere. On the other hand, the work by Ferreira & Potgieter (2004) implies that such measurements could be interpreted correctly only if our model takes into account all physical transport processes in the heliosphere.

The *Ulysses*/KET project is supported under grant 50 OC 0105 and 50 OC 0902 by the German Bundesministerium für Wirtschaft through the Deutsches Zentrum für Luft- und Raumfahrt (DLR). M.S.P. and S.E.S.F. acknowledge the partial financial support of the SA National Research Foundation and the SA Centre for High Performance Computing. The German–South African Collaboration has been supported by the DLR under grant SUA 07/013. This work profited from the discussions with the participants of the ISSI Team meeting "Transport of Energetic Particles in the Inner Heliosphere." Wilcox Solar Observatory data used in this study was obtained via the Web site http://wso.stanford.edu, courtesy of J. T. Hoeksema.

REFERENCES

Alanko-Huotari, K., Usoskin, I. G., Mursula, K., & Kovaltsov, G. A. 2007, J. Geophys. Res. (Space Phys.), 112, 8101
Belov, A., et al. 2001, in Proc. 27th ICRC (Hamburg), 3996
Burger, R. A., Potgieter, M. S., & Heber, B. 2000, J. Geophys. Res., 105, 27447
Chen, J., & Bieber, J. W. 1993, ApJ, 405, 375
Clem, J., Evenson, P., & Heber, B. 2002, Geophys. Res. Lett., 29, 2096
Ferreira, S. E. S., & Potgieter, M. S. 2004, ApJ, 603, 744
Ferreira, S. E. S., Potgieter, M. S., & Scherer, K. 2008a, in AIP Conf. Ser. 1039, Particle Acceleration and Transport in the Heliosphere and Beyond, ed. G. Li et al. (Melville, NY: AIP), 355
Ferreira, S. E. S., & Scherer, K. 2006, ApJ, 642, 1256
Ferreira, S. E. S., Scherer, K., & Potgieter, M. S. 2008b, Adv. Space Res., 41, 351
Gieseler, J., Heber, B., & Müller-Mellin, R. 2007, in Proc. 30th ICRC (Mexico City), 571
Heber, B., Clem, J. M., Müller-Mellin, R., Kunow, H., Ferreira, S. E. S., & Potgieter, M. S. 2003, Geophys. Res. Lett., 30, 6
Heber, B., Gieseler, J., Dunzlaff, P., Gomez-Herrero, R., Müller-Mellin, R., Mewaldt, R., Potgieter, M. S., & Ferreira, S. 2008, ApJ, 689, 1443
Heber, B., et al. 1996, A&A, 316, 538
Heber, B., et al. 1999, Geophys. Res. Lett., 26, 2133
Heber, B., et al. 2002, J. Geophys. Res., 107, 1274
Hoeksema, J. T. 1995, Space Sci. Rev., 72, 137
Issautier, K., Le Chat, G., Meyer-Vernet, N., Moncuquet, M., Hoang, S., MacDowall, R. J., & McComas, D. J. 2008, Geophys. Res. Lett., 35, 19101
Jokipii, J. R., & Kóta, J. 1995, Space Sci. Rev., 72, 379
Jokipii, J. R., Levy, E. H., & Hubbard, W. B. 1977, ApJ, 213, 861
Klassen, A., Krucker, S., Kunow, H., Müller-Mellin, R., Wimmer-Schweingruber, R., Mann, G., & Posner, A. 2005, J. Geophys. Res. (Space Phys.), 110, 9
McComas, D. J., Ebert, R. W., Elliott, H. A., Goldstein, B. E., Gosling, J. T., Schwadron, N. A., & Skoug, R. M. 2008, Geophys. Res. Lett., 35, 18103
McDonald, F., Lal, N., & McGuire, R. 1998, J. Geophys. Res., 10, 373
Meyer, P., & Evenson, P. 1978, IEEE Trans. Geosci. Electron., 16, 180
Parker, E. N. 1958, ApJ, 128, 664

Parker, E. N. 1965, Planet. Space Sci., 13, 9
Potgieter, M. S., Burger, R. A., & Ferreira, S. E. S. 2001, Space Sci. Rev., 97, 295
Potgieter, M. S., & Ferreira, S. E. S. 2001, Adv. Space Res., 27, 481
Rastoin, C. 1995, PhD thesis, Saclay CEA
Scherer, K., & Ferreira, S. E. S. 2005, A&A, 442, L11
Simnett, G. M. 2006, A&A, 445, 715
Simpson, J., et al. 1992, A&AS, 92, 365
Smith, E. J., & Balogh, A. 2008, Geophys. Res. Lett., 35, L22103
Stone, E. C., et al. 1998, Space Sci. Rev., 86, 357
Webber, W. R., Heber, B., & Lockwood, J. A. 2005, J. Geophys. Res. (Space Phys.), 110, 12107
Wenzel, K. P., Marsden, R. G., Page, D. E., & Smith, E. J. 1992, A&AS, 92, 207
Wibberenz, G., Richardson, I. G., & Cane, H. V. 2002, J. Geophys. Res., 107, 1353

The analysis of charge-sign effects in the modulation of GCRs was in the past primarily inhibited by the lack of precise and simultaneous measurements of oppositely charged particles with the same rigidity. Especially electron observations were quite scarce, and if available they mostly incorporated the caveat that electrons and positrons were combined into one single measurement (see e.g. Webber et al., 2005). This situation improved with the launch of the PAMELA and AMS-02 missions in 2006 and 2011, respectively. These instruments have the capability to detect and distinguish electrons, positrons, protons, anti-protons and heavier nuclei from about 100 MeV to several hundreds of GeV (Picozza et al., 2007; Aguilar et al., 2013). For PAMELA, first time series (with multiple months intervals) of proton and electron observations in the same rigidity range are already available (Adriani et al., 2013, 2015). Recently, Di Felice et al. (2017) investigated the temporal variations from 2006–2009 in more detail.

In the future, more observation results by AMS-02 and PAMELA are expected. While PAMELA operated until 2016 (Galper et al., 2017), the AMS-02 mission is planned to continue until 2024 (Bindi et al., 2017). Altogether, this would cover from 2006 on a complete $A < 0$ solar minimum, the solar maximum, and the following $A > 0$ solar minimum (expected around 2020) with precise energy resolution, allowing for further investigations of charge-sign modulation effects.

5

MODIFICATION OF THE FORCE FIELD APPROACH

Parker (1965) introduced the widely used transport equation for GCRs in the heliosphere (Eq. 1, cf. Sect. 1.3). A more rigorous derivation resulting in the same equation was given by Gleeson and Axford (1967), who also presented an approximate solution, the so-called force field approach (Gleeson and Axford, 1968). This approach reduces the full transport equation to a simple quasi-analytical model which modulates a given LIS depending only on one parameter (aside from the particle type), the so-called modulation potential (or force field parameter) ϕ. The principle derivation of this first-order approximation is given in Sect. 5.1.2, see Caballero-Lopez and Moraal (2004) and Moraal (2013) for more details.

As already mentioned in Sect. 1.3, analytical solutions to the Parker equation are only available under special assumptions, and in general numerical models have to be used. This is one reason why simple models like the force field approach were commonly used in the past. Another still valid reason is the fact that with its single parameter it is a really handy and easy to use tool to describe the level of solar modulation of GCRs. This is especially true for users from adjacent scientific fields, like cosmogenic radionuclids, who are not well versed on GCR transport models. However, the force field approach has serious limitations, as laid out e.g. by Caballero-Lopez and Moraal (2004) and later in this chapter.

A common approach is to define the solar modulation potential ϕ for a given time period by choosing that potential which best reflects a given set of GCR observations. Widely used are the findings of Usoskin et al. (2005, 2011), who utilize the LIS from Burger et al. (2000) and measurements of neutron monitors and ionization chambers to determine a time series of monthly ϕ values describing the solar modulation level since 1936. While neutron monitors provide a long-lasting time series of GCR observations, they lack direct energy information and only give a count rate integrated over the whole energy (respectively rigidity) range above their individual, location based and time-dependent vertical geomagnetic cutoff rigidity (Smart and Shea, 2009; Herbst et al., 2013). With the launch of the PAMELA mission (Picozza et al., 2007) in 2006, we have access to precise measurements of different GCR species over a wide energy range with very good statistics and a high energy resolution. This allows us to determine the solar modulation potential accurately, and – together with intercalibrated past GCR measurements onboard spacecraft – to derive a time series of GCR measurement at lower energies, compared to neutron monitor observations. In addition, the PAMELA measurements give us the opportunity to further investigate the energy dependence of the solar modulation potential. This analysis has been carried out in the following publication (Gieseler et al., 2017) in Sect. 5.1.3. We show that this energy dependence has significant consequences, and provide in Sect. 5.1.4 a straightforward and – in its limitations – effective work-around. This two-parameter force field approach allows to calculate a rigidity-dependent solar

modulation potential $\phi(P)$ based on the ϕ values of Usoskin et al. (2005, 2011) and derived from our intercalibrated spacecraft measurements. These ϕ values are listed in Appendix A. Together with Eqs. (4) and (10) and the LIS from Burger et al. (2000) they provide a simple method to calculate the monthly GCR intensity at a given energy for the last four solar cycles.

The solar modulation potential is often used for the calculation of the production rates of cosmogenic radionuclids (Muscheler et al., 2016). Because of that, in Sect. 5.1.5 we demonstrate the significant implications on the production rates of ^{10}Be which arise due to our modified force field method.

An empirical modification of the force field approach to describe the modulation of galactic cosmic rays close to Earth in a broad range of rigidities

Gieseler, J., B. Heber, and K. Herbst, *J. Geophys. Res.: Space Phys.*, 122 (2017), DOI:10.1002/2017JA024763. Reproduced with permission of John Wiley & Sons, Inc. © 2017 American Geophysical Union. Own contribution: 90%

AGU PUBLICATIONS

JGR

Journal of Geophysical Research: Space Physics

RESEARCH ARTICLE

10.1002/2017JA024763

Key Points:
- We demonstrate significant rigidity dependence of force field approach
- We introduce two-parameter modification as simple and sufficient work-around
- We provide rigidity-dependent solar modulation potential for 1973-2016

Supporting Information:
- Supporting Information S1
- Data Set S1

Correspondence to:
J. Gieseler,
gieseler@physik.uni-kiel.de

Citation:
Gieseler, J., Heber, B., & Herbst, K. (2017). An empirical modification of the force field approach to describe the modulation of galactic cosmic rays close to Earth in a broad range of rigidities. *Journal of Geophysical Research: Space Physics*, *122*, 10,964–10,979. https://doi.org/10.1002/2017JA024763

Received 13 SEP 2017
Accepted 30 OCT 2017
Accepted article online 6 NOV 2017
Published online 20 NOV 2017
Corrected 27 DEC 2017

This article was corrected on 27 DEC 2017. See the end of the full text for details.

An Empirical Modification of the Force Field Approach to Describe the Modulation of Galactic Cosmic Rays Close to Earth in a Broad Range of Rigidities

J. Gieseler[1], **B. Heber**[1], **and K. Herbst**[1]

[1]Institute of Experimental and Applied Physics, University of Kiel, Kiel, Germany

Abstract On their way through the heliosphere, galactic cosmic rays (GCRs) are modulated by various effects before they can be detected at Earth. This process can be described by the Parker equation, which calculates the phase space distribution of GCRs depending on the main modulation processes: convection, drifts, diffusion, and adiabatic energy changes. A first-order approximation of this equation is the force field approach, reducing it to a one-parameter dependency, the solar modulation potential ϕ. Utilizing this approach, it is possible to reconstruct ϕ from ground-based and spacecraft measurements. However, it has been shown previously that ϕ depends not only on the local interstellar spectrum (LIS) but also on the energy range of interest. We have investigated this energy dependence further, using published proton intensity spectra obtained by PAMELA and heavier nuclei measurements from IMP-8 and ACE/CRIS. Our results show severe limitations at lower energies including a strong dependence on the solar magnetic epoch. Based on these findings, we will outline a new tool to describe GCR proton spectra in the energy range from a few hundred MeV to tens of GeV over the last solar cycles. In order to show the importance of our modification, we calculate the global production rates of the cosmogenic radionuclide ^{10}Be which is a proxy for the solar activity ranging back thousands of years.

1. Introduction

During the last years major progress has been achieved concerning the modulation of galactic cosmic rays (GCRs) due to several facts:

1. Voyager 1 and 2 passed the termination shock at 94 AU (Stone et al., 2005) and 84 AU (Richardson et al., 2008), respectively, and Voyager 1 the heliopause at 121 AU (Gurnett et al., 2013), setting the boundary of the modulation volume that is directly influenced by the Sun's activity.
2. The local interstellar spectra (LIS) of ions and electrons are now much better known than ever before (Bisschoff & Potgieter, 2016; Corti et al., 2016; Ghelfi et al., 2016; Herbst et al., 2017; Potgieter et al., 2015; Vos & Potgieter, 2015) thanks to the Voyager measurements (Cummings et al., 2016; Stone et al., 2013) in the outer heliosheath and the precise measurements by the PAMELA (Adriani et al., 2011a; 2011b) and AMS-02 (Aguilar et al., 2015) investigations.
3. The particle-wave interaction in the solar wind that leads to particle scattering, described in the transport equation of Parker (1965) by diffusive processes (Burger et al., 2000; Shalchi, 2015; Tautz et al., 2014), is now better understood.
4. Modeling the background heliosphere (e.g., Scherer et al., 2011) and the particle propagation (Potgieter, 2013) has seen a significant progress thanks to increasing computing power.

However, another line of research contributed much in our current understanding of GCRs. Cosmogenic radionuclides are the only window to the Sun's activity history over more than a few thousand years. Thus, tremendous effort has been undertaken in order to analyze the different data sets in order to determine the modulation parameter during the Holocene (Herbst et al., 2010; Steinhilber et al., 2008, 2012; Vonmoos et al., 2006). For such studies the first-order force field approximation depending only on one parameter, the force field parameter or solar modulation potential ϕ, is utilized in order to describe the energy spectra at Earth. Commonly, these ϕ values are determined using the count rates of neutron monitors (Ghelfi et al., 2017; Usoskin et al., 2005, 2011, 2017). The energy-dependent response of such ground-based stations at sea level

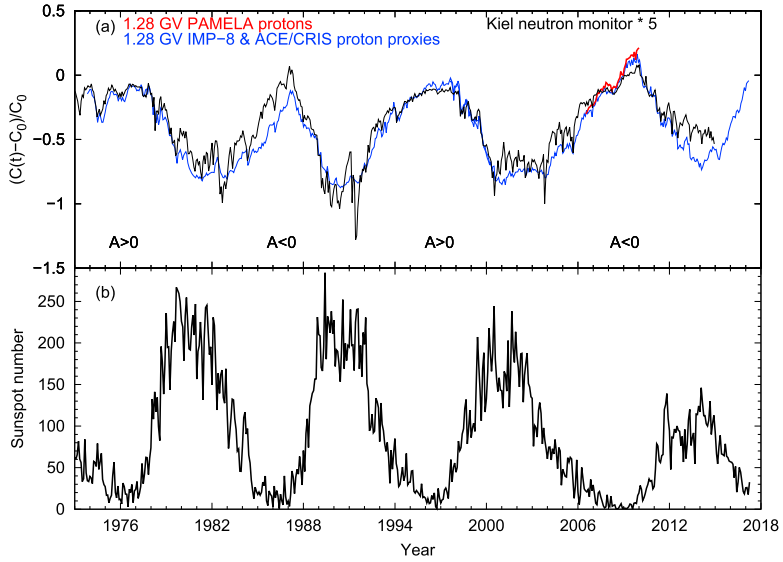

Figure 1. (a) Monthly averaged count rate variation of the Kiel neutron monitor (black curve, multiplied by 5 to match scale), intensity variations of 1.28 GV proton measurements by PAMELA (red curve), and the intensity variations of 1.28 GV proton proxies (blue curves, cf. section 3.1). The data have been normalized to January 2009. (b) Monthly sunspot number from the Royal Observatory of Belgium.

to protons and α particles has recently be investigated by Mishev et al. (2013). Their Figure 3 shows that the response is decreasing with decreasing energy, with significantly small contributions below a few GeV. Taking into account that the GCR spectra of protons and α particles are not strongly energy dependent in this energy range, neutron monitors are marginally sensitive to energies below a few GeV. However, note that during a ground level enhancement the energy spectrum of solar energetic particles in the range above 700 MeV is $\propto E^{-3}$ (Kühl et al., 2017; Mewaldt et al., 2012), leading to the fact that in these cases an enhancement is usually measurable (Thakur et al., 2016). Like most spacecraft measurements that are only sensitive to energies below a few GeV, the production of cosmogenic radionuclides is sensitive to particles with smaller energies (Webber & Higbie, 2003, 2010). Figure 1a shows the count rate variation of the Kiel neutron monitor (black curve, multiplied by 5 to match scale) and the intensity variations of 1.28 GV proton measurements by PAMELA (red curve) and 1.28 GV proton proxies (blue curve). All variations have been normalized to January 2009. Figure 1b displays the sunspot number from the Royal Observatory of Belgium. The solar magnetic epoch is indicated by $A < 0$ and $A > 0$, respectively. In an $A > 0$ solar magnetic epoch the magnetic field is pointing outward over the northern and inward over the southern hemisphere, vice versa for an $A < 0$ solar magnetic epoch. Note that here and in the following we move from the energy to the rigidity frame in order to compare measurements of different particle species. A more detailed description is given in section 3.1 where the derivation of the 1.28 GV proton proxies is described. From Figure 1 it is evident that

1. the GCR intensity is antiproportional to the sunspot number (i.e., the intensity is high when the sunspot number is low and vice versa),
2. the amplitude of the variation is much larger for the lower rigidities than for the higher rigidities (about a factor of 5 when comparing 1.28 GV protons and their proxies with the Kiel neutron monitor), and
3. there is an rigidity-dependent difference for an $A > 0$ and $A < 0$ solar magnetic epoch minimum, that is, the intensities are larger for the Kiel neutron monitor in 1987 compared to 1976 and 1997 and vice versa for the 1.28 GV proton proxies (omitting the unusual minimum 2009).

The latter effect is only understood when taking into account gradient and curvature drifts: Cosmic ray proton spectra are softer during an $A > 0$ cycle so that below 500 MeV the $A > 0$ solar minima spectra are always higher than the corresponding $A < 0$ spectra (Beatty et al., 1985; Kota & Jokipii, 1983; Potgieter & Moraal, 1985). This means that the adiabatic energy losses that cosmic rays experience are somewhat different in both cycles (Strauss et al., 2011) and also cause the proton spectra for two consecutive solar minima to cross at a few GeV

(Reinecke & Potgieter, 1994). Thus, it is questionable to apply the commonly used energy spectra, derived from neutron monitor measurements utilizing the force field solution, to phenomena that are predominantly caused by lower energy ions. Recently, Corti et al. (2016) performed a similar approach as laid out in this work, utilizing a force field modification with two ϕ parameters to describe GCR spectra measured over a large energy range by BESS, PAMELA, and AMS-02 but only for single selected time periods from 1993 to 2011. Cholis et al. (2016) presented a rigidity-dependent modulation parameter that is not derived from direct GCR measurements but instead of measurements of the heliospheric current sheet tilt angle and the magnetic field amplitude.

In what follows we will briefly recall the derivation of the force field solution following the work by Moraal (2013). In the following section it is shown that helium and carbon measurements at 1.27 GV aboard IMP-8 and ACE, respectively, are a good proxy for the temporal variation of protons at the same rigidity. Normalizing these count rates to the proton intensities at 1.28 GV measured by PAMELA, we can derive a solar modulation potential at these rigidities. Following the arguments from Herbst et al. (2010, 2017), this solar modulation potential, however, does not necessarily have to be in agreement with the one derived by Usoskin et al. (2005, 2011) but also not with those given by Gil et al. (2015) and Usoskin et al. (2017) because it is derived at a different rigidity range. In order to ascribe the full spectrum, we perform a detailed analysis of the rigidity dependence of the solar modulation potential using the high-precision PAMELA measurements and show that a weighted combination of two modulation potentials is capable to describe the rigidity spectra for a full Hale cycle.

2. Cosmic Ray Transport in the Heliosphere

The transport of cosmic rays inside the heliosphere was first described by Parker (1965):

$$\frac{\partial f}{\partial t} = -\Big(\underbrace{\mathbf{V}}_{\text{i}} + \underbrace{\langle \mathbf{v}_D \rangle}_{\text{ii}}\Big) \cdot \nabla f + \underbrace{\nabla \cdot \Big(\overleftrightarrow{\kappa} \cdot \nabla f\Big)}_{\text{iii}} + \underbrace{\frac{1}{3}(\nabla \cdot \mathbf{V})\frac{\partial f}{\partial \ln P}}_{\text{iv}} + \underbrace{Q}_{\text{v}}, \tag{1}$$

where $f(\mathbf{r}, P, t)$ denotes the differential cosmic ray phase space distribution function, $\mathbf{r}$ the spatial coordinates, P the particle rigidity, t the time, and (i) the outward convection by the solar wind speed $\mathbf{V}$, (ii) the gradient and curvature drifts in the global heliospheric magnetic field (Jokipii et al., 1977), (iii) the diffusion through the irregular heliospheric magnetic field, (iv) the adiabatic energy change due to the divergence of the expanding solar wind, and (v) the local sources like particles accelerated at the Sun.

Although the modulation of GCRs in the heliosphere strongly depends on all the processes mentioned above, a much simpler analytical approximation can be derived from equation (1). Following Moraal (2013; see also Gleeson & Axford 1968; Caballero-Lopez & Moraal 2004), equation (1) can be reduced to a simple convection-diffusion equation if there is (a) no source of cosmic rays ($Q = 0$), (b) a steady state ($\partial f/\partial t = 0$), (c) an adiabatic energy loss rate $\langle \mathrm{d}P/\mathrm{d}t \rangle = (P/3)\mathbf{V} \cdot \nabla f/f = 0$, and (d) no drifts. Assuming spherical symmetry, that is, only the radial direction is taken into account, this leads to

$$\frac{vP}{3}\frac{\partial f}{\partial P} + \kappa \frac{\partial f}{\partial r} = 0, \tag{2}$$

with $v = V_r$ denoting the solar wind speed. If the diffusion coefficient $\kappa(r, P)$ is separable $\kappa = \kappa_1(r) \cdot \kappa_2(P)$ with r the heliocentric distance and P the particle rigidity, and furthermore, $\kappa_2(P) \propto P$, the following expression for the so-called force field parameter (or solar modulation potential) ϕ can be obtained:

$$\phi(r) = \int_r^{r_b} \frac{v(r')}{3\kappa_1} \mathrm{d}r'. \tag{3}$$

Here r_b represents the outer boundary like the solar wind termination shock or the heliopause (cf. Caballero-Lopez & Moraal 2004). Typical modulation values, still depending on the LIS model used, vary between 300 and 1,500 MV with increasing solar activity. Gleeson and Urch (1973) as well as Caballero-Lopez and Moraal (2004) and Moraal (2013) investigated the validity of the force field approximation by comparing its results with a full numerical solution of the steady state, spherically symmetric (one-dimensional) transport equation and direct measurements (see, e.g., Figure 5 in Moraal, 2013). Although they found that the approximation starts to deviate from the full numerical solution at energies below ~150–550 MeV and when going to the outer

heliosphere, it is still a useful way to describe differential intensity spectra J_{1AU} at 1 AU during intermediate and low solar activity by using the following equation:

$$J_{1AU}(E,\phi) = J_{LIS}(E+\Phi)\frac{(E)(E+2E_r)}{(E+\Phi)(E+\Phi+2E_r)}. \quad (4)$$

The force field function Φ is given by $\Phi = (Ze/A)\phi$, where Z and A are the charge and mass number of the cosmic ray nuclei, respectively. E represents the kinetic energy of the particles, E_r their rest energy ($E_r = 0.938$ GeV for protons), and J_{LIS} gives the differential energy spectra of the LIS representing the boundary condition of the force field approximation. However, the full LIS by now has not been measured; thus, multiple LIS models exist in the literature.

In what follows, we perform a χ^2 minimization process similar to Wiedenbeck et al. (2005) to derive the solar modulation potential ϕ for an actual measurement of the intensity spectrum J_{1AU} at 1 AU. First, we generate model intensity spectra for the investigated energy (respectively rigidity) range using the force field solution with varying ϕ. In this process we use either the LIS from Burger et al. (2000) as described by Usoskin et al. (2005) (used for a more in-detail analysis later on) or the newer model by Vos and Potgieter (2015), which is used by Usoskin et al. (2017). Then, for each spectrum we calculate the sum-of-squares deviation to the measured spectrum and choose that ϕ with the smallest deviation.

3. Observation and Data Analysis

As already mentioned, the energy (rigidity)-dependent modulation of galactic cosmic rays (GCRs) with solar activity is shown in Figure 1a, where the intensity variations of the Kiel neutron monitor (black curve) and of 1.28 GV proton proxies (blue curves) as a proxy for high and low-energy GCRs are plotted over time, respectively. A simple comparison with the sunspot number in Figure 1b gives the anticorrelation between solar activity and GCR intensity. As described in section 2, the time profile of high-energy GCRs in the inner heliosphere can be reasonably approximated by the force field approximation. In this process, the energy spectrum of a GCR species at 1 AU is derived from its unmodulated local interstellar spectrum (LIS) only by the modulation potential ϕ.

3.1. Proton Proxies

Neutron monitors at Earth have been proven to be very reliable proxies for long-time GCR measurements. However, they are limited with respect to the observable energies due to the shielding of the Earth's magnetic field and atmosphere. To measure energies below the GeV range, one has to take advantage of balloon-borne or spacecraft experiments. In this work we will use energetic particle observations from the spacecraft ACE, IMP-8, and PAMELA to cover the time period from the 1970s to the last, commonly called unusual solar minimum in 2009 and beyond.

In a first step we are interested in the temporal behavior of different ions with the same rigidity. The rigidity P is calculated from the particle momentum p by $P = \frac{pc}{|Z|e}$. It has been shown previously that ions with the same ratio $\frac{Ze}{A}$ like helium, carbon, or oxygen undergo the same temporal variation (e.g., Heber et al., 2008; Gieseler et al., 2008; McDonald et al., 2010; Webber et al., 2005). We take advantage of this and use IMP-8 helium and ACE/CRIS carbon measurements as proxies for protons at the same rigidity. Figure 2 shows the correlation between monthly proton intensities measured by PAMELA (Adriani et al., 2011a) and normalized ACE/CRIS carbon intensities (ACE Science Center) at three corresponding rigidities (the highest available for ACE/CRIS carbon) in the time 2006–2009 (left), and the same three carbon intensities correlated with normalized IMP-8 helium intensities (F. B. McDonald, private communication, 2006) at 1.03–1.45 GV for 1997–2000 (right), respectively. In both cases the three different ACE/CRIS carbon intensities show good linear correlations with the PAMELA protons and IMP-8 helium, yielding slopes from 0.93±0.02 to 0.95±0.02 and 0.91±0.01 to 0.96 ± 0.02 for the best fit linear regressions, respectively.

Although the different particles should undergo the same temporal variations by the solar modulation, differences in the spectral slopes of their individual LIS can lead to variations in their intensity ratios. The significance of this effect has been investigated by calculating the differential rigidity spectra ratios at Earth of protons to carbon, helium to carbon, and protons to helium, respectively. Here the force field approach with different LIS for all three particles has been used. We choose to utilize the model from Bisschoff and Potgieter (2016) because it provides independent LIS for each investigated species: proton, helium, and carbon. In Figure 3,

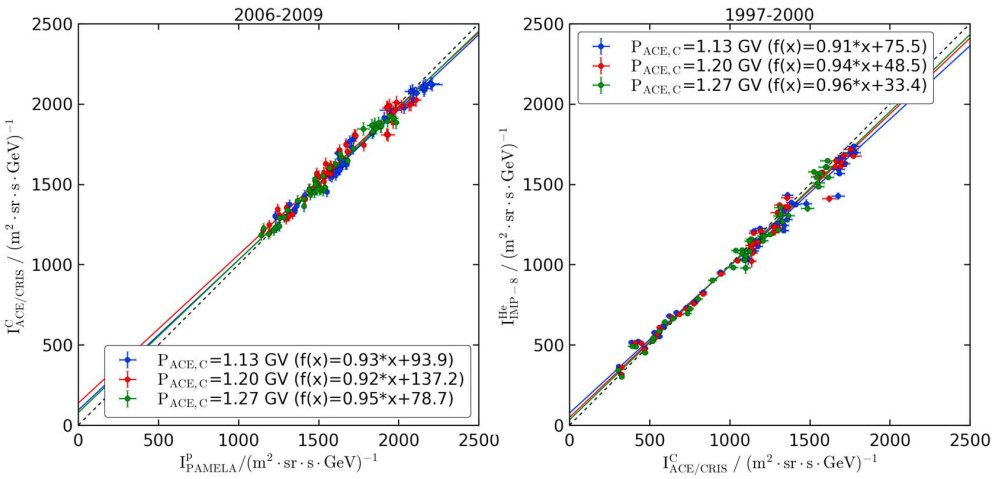

Figure 2. (left) Normalized carbon intensities from ACE/CRIS with respect to PAMELA proton intensities at three corresponding rigidities. (right) Normalized helium intensities from IMP-8 (1.03–1.45 GV) with respect to normalized ACE/CRIS carbon intensities at three different rigidities (all data with statistical errors). For each data set the best fit linear regression is given.

these ratios are plotted with respect to the solar modulation potential for different rigidities. At low particle rigidities all ratios show a dependency with the solar modulation potential, which gets significant for very low rigidities. At the observed 1.3 GV the intensity ratios can vary by a maximal factor of 19.2% for protons to carbon, 8.9% for protons to helium, and 9.5% for helium to carbon, when comparing intensities at low (ϕ = 300 MV) and high (ϕ = 1,200 MV) solar activity. However, the effect vanishes when intensities are compared at the same level of solar activity. For the periods with solar modulation potentials between 530 MV and 690 MV (i.e., years 2006–2009) the ratio of the measured 1.28 GV proton intensity from PAMELA and 1.27 GV carbon intensity from ACE/CRIS follows the same behavior, albeit with a constant offset. In what follows we will use the 1.27 GV ACE/CRIS carbon intensity, normalized to the 1.28 GV PAMELA proton intensity, and the 1.03-1.45 GV IMP-8 helium intensity, normalized to the normalized 1.27 GV ACE/CRIS carbon intensity, as proxies for 1.28 GV protons.

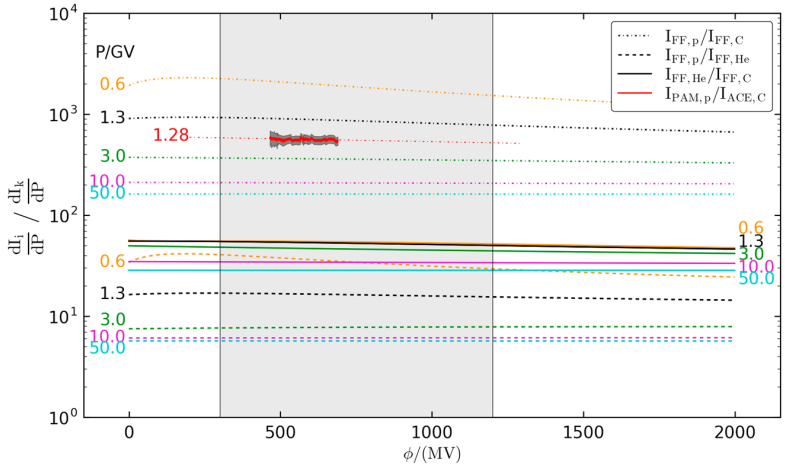

Figure 3. Dependency of the ratio of force field model differential rigidity spectra of protons to carbon (dash-dotted lines), helium to carbon (solid lines), and proton to helium (dashed lines), with respect to the solar modulation potential ϕ and for different rigidities (denoted next to lines). All LIS based on Bisschoff and Potgieter (2016). The red line shows the ratio of the proton intensities measured by PAMELA at 1.28 GV and the carbon intensities measured by ACE/CRIS at 1.27 GV with statistical errors (gray shaded area with additional systematic errors for PAMELA; red dash-dotted line shows a fit line through the measurements). Marked by shading from 300 to 1200 MV is the range of typical solar modulation.

3.2. Intensity Time Profiles

Figure 4 (top) displays the intensity time profiles of 1.28 GV protons measured by PAMELA (red curve) and the corresponding proton proxies derived from IMP-8 helium (1973–2000, blue curve) and ACE/CRIS carbon measurements (1997–2017, blue curve). The orange curve shows the intensity time profile at 1.28 GV using the solar modulation potential from Usoskin et al. (2011) based on the LIS from Burger et al. (2000), while the black curve shows the same intensity for the updated modulation potential as given by Usoskin et al. (2017) using the LIS from Vos and Potgieter (2015). Figure 4 (bottom) shows the deviation of the calculated force field intensities for ϕ from Usoskin et al. (2011) (orange) and Usoskin et al. (2017) (black) compared to the proton proxies, respectively. Utilizing the solar modulation values from Usoskin et al. (2011), the intensities are overestimated by up to 70% and 50% during the 1980s and 2000s solar minima, respectively. The differences are significantly smaller during the 1970s and 1990s. This behavior is somehow expected due to the hardening of the spectra during an $A < 0$ solar magnetic epoch. Usoskin et al. (2017) presented an updated version of their modulation potential reconstruction (for the energy range 1–30 GeV, i.e., 1.7–30.9 GV), which includes three main changes: (1) the usage of the new yield function for neutron monitors at sea level by Mishev et al. (2013); (2) the usage of a recent LIS by Vos and Potgieter (2015), which incorporates Voyager measurements in the outer heliosheath; and (3) the calibration of the neutron monitor response to the direct PAMELA proton measurements from 2006 to 2009. Because of the changes in the used LIS, the solar modulation potentials from Usoskin et al. (2005, 2011) and Usoskin et al. (2017) cannot be compared directly (cf. Figure 10 in Usoskin et al., 2017). However, the yielded intensities are comparable and shown in Figure 4 (top). The intensity calculated using the force field solution with the new modulation potential from Usoskin et al. (2017) (black line) agrees quite well with the PAMELA proton intensities from 2006 to 2009 because of the calibration to these measurements and also with the proton proxies during the previous $A < 0$ cycle (cf. Figure 4, bottom). Usoskin et al. (2017) noted that their model may slightly underestimate the modulation during periods of high solar activity (i.e., low solar modulation potential). This can be seen in the time periods around 1980–1983, 1989–1992, 2001–2004, and 2012–2016, where their model overestimates the intensities compared to the measured proton proxies by up to 50%, 85%, 130%, and 100%, respectively. However, more important are the discrepancies between the Usoskin et al. (2017) model and the proton proxies in the $A > 0$ cycles. During the 1970s and 1990s solar minima the model underestimates the intensities permanently by up to 20%. Note that this cannot be explained by the effect of different LIS for protons, helium, and carbon (as investigated in Figure 3) because at all solar minima there were comparable intensity levels and thus ϕ values. The only exception is in 2009 where the highest space-age intensities were detected, but this time period does not show any different behavior.

3.3. Solar Modulation Potential for Different Rigidity Ranges

Gil et al. (2015) and Usoskin et al. (2017) showed that the solar modulation potential ϕ from Usoskin et al. (2011), which is calculated using neutron monitor observations, is not in agreement with ϕ values obtained by the analysis based on PAMELA proton data. Details of the fitting procedure of the PAMELA data are only given in Usoskin et al. (2017), where ϕ is fitted to proton energies from 1 to 30 GeV (i.e., 1.7 to 30.9 GV), which the authors claimed is the most effective part of the energy spectrum for GCR detection by neutron monitors. In the following we investigate in more detail which part of the PAMELA proton spectra should be used to calculate the solar modulation potential in order to compare it with one derived by neutron monitor measurements. As discussed in section 1, the most recent yield function of a sea level neutron monitor is given by Mishev et al. (2013). Their Figure 3 indicates the strong decrease of the yield function with decreasing energies below 10 GeV. To investigate the implications of this effect, we used the force field approach to generate rigidity-dependent GCR proton intensity spectra for two typical solar modulation potentials, 300 and 1,200 MV, reflecting low and high solar activity, respectively. These spectra are then folded with the proton yield function from Mishev et al. (2013) (in the analytical form given by Caballero-Lopez, 2016), resulting in Figure 5. Marked by shading are the areas containing 1% and 50% of the particles; that is, the rigidity range up to 3 GV contains only 1% of all particles for the scenario with $\phi = 1,200$ MV (and even less for a smaller ϕ), while up to 15–20 GV 50% of the particles are detected, yielding an approximation for the mean neutron monitor rigidity. This indicates that neutron monitors are almost not sensitive to the rigidity range below 3 GV, where the PAMELA proton data show the strongest modulation effects.

Figure 6 (first and second panels) shows the solar modulation potential during the time period 2006–2010 derived as described in section 2 using the proton proxies and different rigidity ranges of the PAMELA

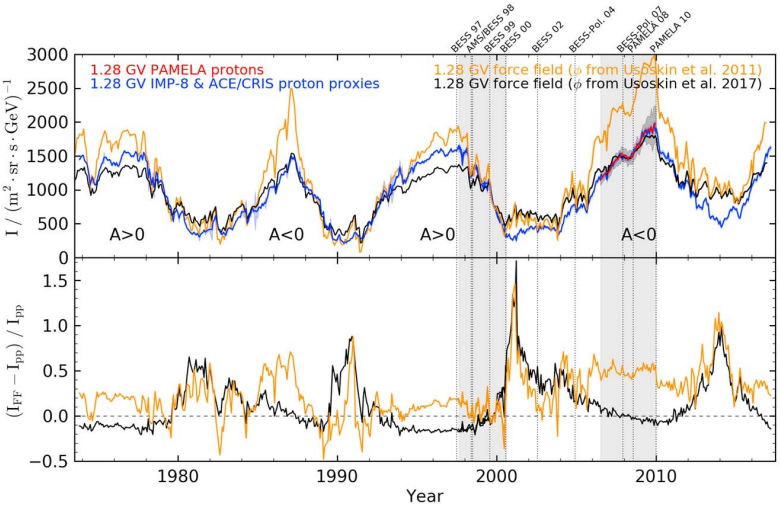

Figure 4. (top) Measured and calculated intensity time profiles of 1.28 GV protons. The red and blue curves reflect the measurements of protons by PAMELA (with statistical uncertainties in red and systematics given by gray shaded area, respectively) as well as proton proxies by IMP-8 helium (1973–2000) and ACE/CRIS carbon (1997–2017, both with statistical errors), respectively. The calculated intensity of the force field solution at 1.28 GV using the modulation potential from Usoskin et al. (2011) based on the LIS from Burger et al. (2000) is displayed by the orange curve, while the black curve shows the same intensity for the updated modulation potential as given by Usoskin et al. (2017) using the LIS from Vos and Potgieter (2015). (bottom) The deviation of the calculated force field intensities for ϕ from Usoskin et al. (2011) (orange) and Usoskin et al. (2017) (black) compared to the proton proxies, respectively. The two shaded time periods mark the normalization interval of IMP-8 helium to ACE/CRIS carbon and of ACE/CRIS carbon to PAMELA protons, respectively (cf. Figure 2). Vertical dotted lines with annotations above plot indicate the measurement periods used in Figure 10.

proton measurements together with the neutron monitor based results of Usoskin et al. (2011) (ϕ_{Uso11}) and the deviations between these findings. All potentials were calculated using the LIS of Burger et al. (2000). Figure 6 (third and fourth panels) shows the same potentials from proton proxies and PAMELA as well as results from Usoskin et al. (2017) (ϕ_{Uso17}), but now the LIS of Vos and Potgieter (2015) was used. $\Delta\phi_{\mathrm{Uso11}}$ is given as a 1σ uncertainty of 26 MV (Usoskin et al., 2011) and $\Delta\phi_{\mathrm{Uso17}} < 10$ MV (Usoskin et al., 2017; in Figure 6 (third and fourth panels) 10 MV is shown). The uncertainties $\Delta\phi_{\mathrm{pp}}$ of the calculated solar modulation potential derived

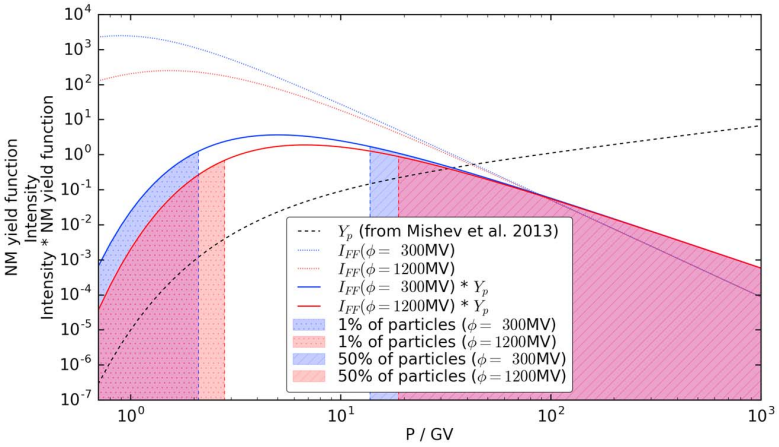

Figure 5. Rigidity-dependent force field proton intensity spectra I_{FF} for two typical solar modulation potentials (300 and 1,200 MV) folded with the proton yield function Y_p from Mishev et al. (2013) (arbitrary units on y axis). Marked by blue and red shading are the areas containing 1% and 50% of the particles, respectively.

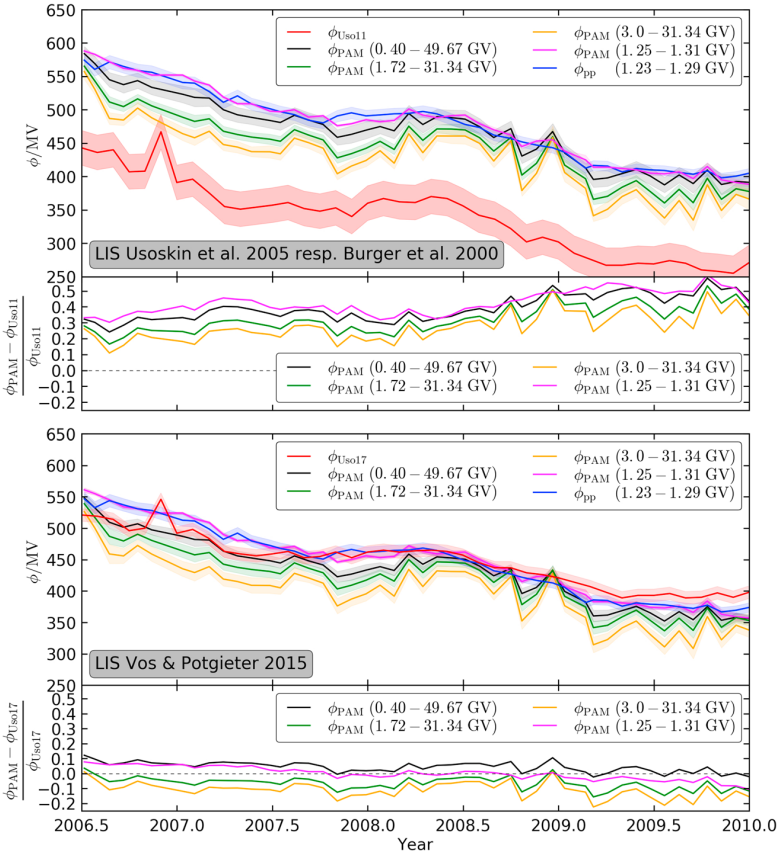

Figure 6. (first and second panels) Solar modulation potential (with uncertainty range) from Usoskin et al. (2011) based on neutron monitor measurements (red curve), derived from 1.23–1.29 GV proton proxies (ACE/CRIS carbon, blue curve) and from PAMELA proton measurements in different rigidity ranges. All modulation potentials were calculated using the LIS from Burger et al. (2000). The deviations of the solar modulation potentials derived by PAMELA to those from Usoskin et al. (2011) are plotted in the panel below. (third and fourth panels) Same as above, but now the solar modulation potentials are calculated using the LIS from Vos and Potgieter (2015) or are taken from Usoskin et al. (2017), respectively.

from the proton proxy measurements are determined by estimating the influences of the uncertainties of rigidity, ΔP, and of intensity, ΔI, as follows:

$$\Delta\phi_P = \max|\phi(P,I) - \phi(P \pm \Delta P, I)| \tag{5}$$

$$\Delta\phi_I = \max|\phi(P,I) - \phi(P, I \pm \Delta I)| \tag{6}$$

$$\Delta\phi_{\rm pp} = \sqrt{\Delta\phi_P{}^2 + \Delta\phi_I{}^2}. \tag{7}$$

Here ΔI is the statistical uncertainty of the measured intensities. ΔP, the uncertainty of the mean rigidity of the single proton proxy measurement channel, is estimated by using a force field intensity $I_{\rm FF}$ to calculate the spectral-dependent mean rigidity at very low ($\phi = 200$ MV) and at very high solar activity ($\phi = 1,500$ MV) following

$$\langle P \rangle = \frac{\sum I_{\rm FF}(P_i,\phi)\cdot P_i}{\sum I_{\rm FF}(P_i,\phi)} \tag{8}$$

$$\Delta P = \frac{1}{2}\cdot\left|\langle P_{\rm low}\rangle - \langle P_{\rm high}\rangle\right|. \tag{9}$$

The different $\phi_{\rm PAM}$ are derived from different parts of the PAMELA proton spectrum by a nonlinear least squares fit procedure weighting each data point by its uncertainties in rigidity and intensity. To estimate their

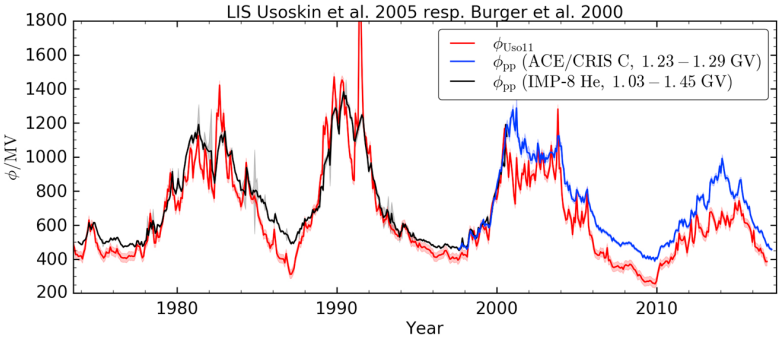

Figure 7. Similar to Figure 6 (first panel) but now for the time period 1973–2017: Solar modulation potential from Usoskin et al. (2011) based on neutron monitor measurements (red curve) and derived from 1.28 GV proton proxies (IMP-8 helium and ACE/CRIS carbon, black and blue curve, respectively). All modulation potentials were calculated using the LIS from Burger et al. (2000).

errors $\Delta\phi_{\mathrm{PAM}}$, the 1σ uncertainties are used. An exception is ϕ_{PAM} for the single channel PAMELA proton measurement "1.25–1.31 GV." Because it contains only one rigidity data point, the same approach as for the $\Delta\phi_{\mathrm{pp}}$ is used here.

The significant difference between ϕ_{Uso11} and the potentials from PAMELA, ϕ_{PAM_i}, is visible in Figure 6 (first and second panels), especially if it is compared to the potentials derived from single measurement channels at lower rigidities (magenta and blue lines) or from the whole spectrum from 0.4 to 50 GV (black line). This offset gets smaller when only higher rigidity parts of the PAMELA proton spectrum are used for the potential calculation, starting from the rigidity range 1.7–31.3 GV (green line) used by Usoskin et al. (2017) up to neglecting all lower rigidity particles and also the high rigidities where almost no solar modulation takes place (3–31.3 GV, orange line). Still, the offset is between 10% and 50%. Furthermore, the deviations of ϕ_{PAM_i} to ϕ_{Uso11} show a small temporal trend. Altogether, from Figure 6 (first and second panels) it seems obvious that the smallest deviation can be achieved if the lower rigidities are left out from the ϕ calculation, as indicated in Figure 5, and only the spectrum from 3 GV upward is used. Defining this threshold at higher rigidities would result in losing sensitivity to the solar modulation, which significantly decreases with increasing rigidity in this range. This will be shown in more detail in section 3.4. The overall picture seems to be more coherent in Figure 6 (third and fourth panels), where ϕ_{Uso17} was calculated using PAMELA measurements to calibrate the neutron monitor responses in the investigated time interval. This results in much smaller deviations between ϕ_{PAM_i} and ϕ_{Uso17}. But also in the fact that the neutron monitor based ϕ_{Uso17} now better reflects the lower rigidity parts of the PAMELA proton spectrum than the rigidity ranges, which should correspond to neutron monitor measurements.

Because we want to use a solar modulation potential reflecting the neutron monitor measurements in the following analysis, we continue using ϕ_{Uso11} from Usoskin et al. (2011) and calculate ϕ_{pp} reflecting the proton proxy measurements using the LIS from Burger et al. (2000) for the time period from 1973 to 2017. These results are presented in Figure 7 and are available as Data Set S1 in the supporting information (also online at http://www.ieap.uni-kiel.de/et/ag-heber/cosmicrays).

3.4. Rigidity Dependence of the Solar Modulation Potential

In order to derive the rigidity dependence of the solar modulation potential, we utilize the monthly averaged proton measurements from PAMELA (Adriani et al., 2011a) and apply the following procedure:

1. The LIS from Burger et al. (2000) is used as the input spectrum for equation (4).
2. For each small PAMELA rigidity bin the solar modulation potential ϕ_{PAM_i} that fits best the measured intensity is determined by a minimizing process.
3. These solar modulation potentials are plotted with respect to rigidity (colored lines in Figure 8).

Since the modulation is small compared to the measurement uncertainties at rigidities above 10 GV, the minimization process is not reliable here and the yielding ϕ values are not representative. Note that this picture also depends on the used LIS model. Figure 8 clearly indicates a nonconstant dependency of the solar modulation potential with respect to rigidity. This shows that it is not reasonable to describe GCR intensities in

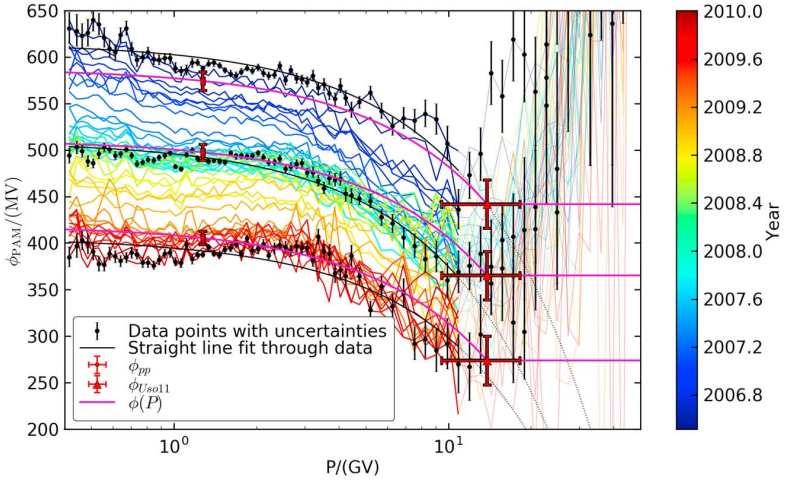

Figure 8. Solar modulation potential derived from PAMELA proton measurements for each rigidity bin and monthly measurement interval (colored lines). The values above 10 GV (plotted with lighter colors) are not reliable; see text for details. In addition, for the first, middle and last investigation period all data points with uncertainties are plotted (black points). Through each ensemble of this data points a straight line fit is calculated (in linear space), omitting the range above 10 GV (black solid line; the dotted line prolongs this fit to higher rigidities). For these three periods also the measured ϕ_{pp} and ϕ_{Uso11} with their uncertainties are included (red data points). Assuming a linear relationship, each pair of ϕ_{pp} and ϕ_{Uso11} is connected by a straight line (in linear space), yielding the rigidity-dependent $\phi(P)$ as given in equation (10) (magenta line).

the inner heliosphere by only one rigidity-independent parameter ϕ. To get an analytically description of the rigidity dependence of ϕ_{PAM}, straight line fits have been calculated for each monthly averaged proton measurement, omitting the unreliable rigidity range above 10 GV (solid black lines in Figure 8). These fits are used to calculate the corresponding rigidities for the neutron monitor-based solar modulation potentials ϕ_{Uso11}: For each monthly potential the rigidity at which the corresponding fit line has the same value is calculated, afterward the mean and standard deviation of these rigidities is calculated. This yields a mean rigidity for ϕ_{Uso11} of $P_{Uso11} = 13.83 \pm 4.39$ GV, which is in the rigidity range expected from Figure 5. With these two solar modulation potentials for two different rigidities in the spectrum we can now establish a full rigidity-dependent modulation potential.

4. The Two-Parameter Force Field Approach

In section 3.4 we showed that it is not sufficient to describe GCR intensities at Earth by only one rigidity-independent parameter. As a work-around, we now present a modified force field approach which utilizes two solar modulation potentials at two different rigidities. We use these two parameters: (1) ϕ_{pp}, derived from the 1.28 GV proton proxies IMP-8 helium and ACE/CRIS carbon, which are normalized to PAMELA proton measurements at the same rigidity, and (2) ϕ_{Uso11}, calculated by Usoskin et al. (2011) and representing the neutron monitor measurements at higher rigidities.

We base our analysis on the modulation potential from Usoskin et al. (2011) and not Usoskin et al. (2017) because we need a potential that reflects the solar modulation at neutron monitor rigidities. In Usoskin et al. (2017) the neutron monitor response has been calibrated to the direct PAMELA proton measurements, thus reflecting these rigidities (cf. section 3.3 and especially Figure 6). In Figure 8 we already showed that the rigidity dependence of ϕ can be approximated by a straight line (in linear scale). Accordingly, we assume a linear interpolation between our two parameters, ϕ_{pp} and ϕ_{Uso11}. Figure 8 also shows the measured ϕ_{pp} and ϕ_{Uso11} for the first, middle, and last PAMELA time period including their uncertainties as given in section 3.3 (red data points). Each pair of ϕ_{pp} and ϕ_{Uso11} is then connected by a straight line (in linear space), yielding our new rigidity-dependent modulation parameter $\phi(P)$ (magenta line):

$$\phi(P) = \begin{cases} \frac{\phi_{Uso11} - \phi_{pp}}{P_{Uso11} - P_{pp}} \cdot (P - P_{pp}) + \phi_{pp} & \text{if } P < P_{Uso11} \\ \phi_{Uso11} & \text{if } P \geq P_{Uso11} \end{cases} \quad (10)$$

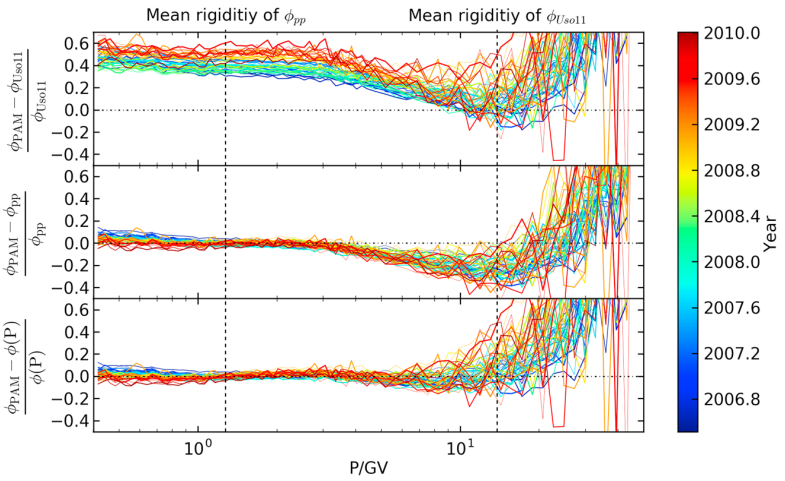

Figure 9. Deviations of the solar modulation potential ϕ_{PAM}, derived from PAMELA proton measurements for each rigidity bin and monthly measurement interval (as in Figure 8), to the rigidity-independent (top) ϕ_{Uso11}, (middle) ϕ_{pp}, and as the (bottom) rigidity-dependent $\phi(P)$.

with $P_{pp} = 1.28 \pm 0.01$ GV and $P_{Uso11} = 13.83 \pm 4.39$ GV as derived in sections 3.1 and 3.4, respectively. Note that $\phi(P) = \phi_{Uso11}$ for higher (i.e., neutron monitor) rigidities, where the minimization process to derive ϕ is not reliable (see section 3.4). The lower limit of $\phi(P)$ is given by the validity of the force field approach at lower rigidities. As described in section 2, at 1 AU the force field solution starts to show significant deviations from a full numerical solution at energies below approximately 150–550 MeV, that is, 0.55–1 GV. Because of that the two-parameter approach presented here—like the standard force field approximation—should not be applied below these rigidities.

Figure 9 shows the deviation of the rigidity-independent ϕ_{Uso11} (top) and ϕ_{pp} (middle), as well as the rigidity-dependent $\phi(P)$ (bottom) to ϕ_{PAM}. Here ϕ_{PAM} is the solar modulation potential derived from PAMELA proton measurements for each rigidity bin and monthly measurement interval from Figure 8. Figure 9 illustrates the rigidity ranges for which ϕ_{Uso11} and ϕ_{pp} are valid (i.e., the deviation vanishes): ϕ_{Uso11}, derived from neutron monitor measurements, is only able to reproduce ϕ_{PAM} measured by PAMELA at rigidities above 10 GV. And ϕ_{pp} can only be used up to 4 GV without deviating significantly from ϕ_{PAM}. However, our newly derived rigidity-dependent modulation parameter $\phi(P)$ is able to describe the ϕ_{PAM} values obtained from PAMELA proton spectrum measurements over the whole rigidity range from 0.4 GV up to neutron monitor rigidities at 15 GV, where the minimization process becomes unreliable with increasing rigidities.

4.1. Comparison With Other Measurements

To test our two-parameter force field approach, a comparison with independent measurements of proton spectra at different times is given in Figure 10 where the deviation between model and measurement is displayed. The model intensities are calculated using equation (4) with the LIS from Burger et al. (2000) and $\phi(P)$ from equation (10), taking the monthly solar modulation potentials ϕ_{pp} and ϕ_{Uso11} as shown in Figure 7 (and available as Data Set S1 in the supporting information). The measurements are from AMS-01 (Alcaraz et al., 2000), BESS (Shikaze et al., 2007), and BESS-Polar I+II (Abe et al., 2016), partly obtained from the Database of Charged Cosmic Rays (Maurin et al., 2014). In addition, two PAMELA measurements, which were used in our previous analysis to determine ϕ_{pp} and $\phi(P)$, are also included here. Note that the time intervals of measurements (given in days next to the year) and models (i.e., ϕ values) can differ significantly, especially for the BESS missions. The BESS balloon flights each took measurements over roughly a day, whereas the solar modulation potentials were calculated for the whole corresponding month. This can result in significant deviations. For BESS-Polar II a weighted mean of the ϕ values for the mission time (December 2007 and January 2008) has been calculated. The shaded areas indicate the uncertainties for the zero deviation lines, resulting from the statistical and systematic errors of the measured intensities (inner shading) and the uncertainties of the ϕ calculations (additional outer shadings). For an interpretation of Figure 10, it is important to also take a look at the long-term temporal variation of GCRs, presented in Figure 4 (top). Here the proton proxy time series

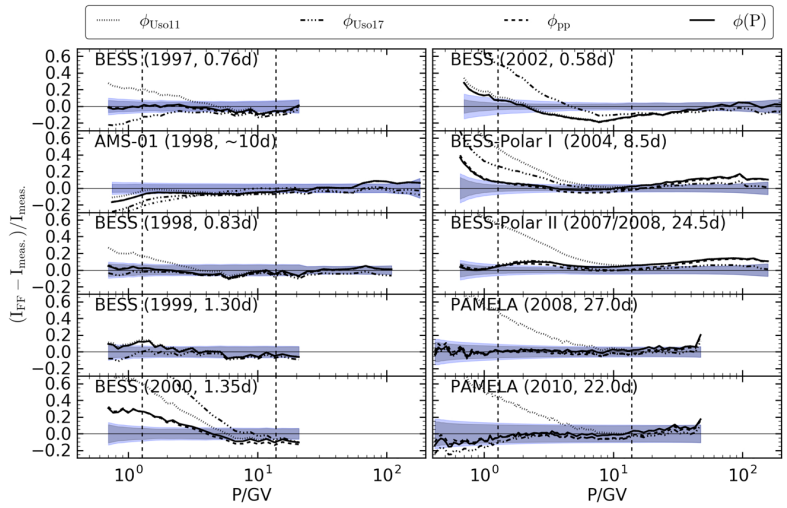

Figure 10. Deviations of proton spectra measured by AMS-01, BESS, BESS-Polar, and PAMELA to force field models for solar modulation potentials from Usoskin et al. (2011) (ϕ_{Uso11}, dotted lines), Usoskin et al. (2017) (ϕ_{Uso17}, dash-dotted lines), derived from proton proxies (ϕ_{pp}, dashed lines), and from equation (10) ($\phi(P)$, solid lines), respectively. The shaded areas indicate the uncertainties for the zero deviation lines, resulting from the statistical and systematic errors of the measured intensities (inner shading) and the uncertainties of the ϕ calculations (additional outer shadings). Note that the time intervals of measurements (given in days next to the year) and models (i.e., ϕ values, monthly values) can differ significantly, especially for the BESS missions. The measurement periods are also indicated in time series plot Figure 4.

is plotted, and the time intervals of all measurements shown in Figure 10 and the solar polarity cycles are indicated. In the following each panel of Figure 10 is interpreted in detail:

1. The three measurements by BESS and AMS from 1997 and 1998 were all obtained during an $A > 0$ solar cycle and show similar results: for the BESS measurements, the ϕ_{Uso11} model delivers too high, the ϕ_{Uso17} model too low intensities at lower investigated rigidities, whereas the $\phi(P)$ model shows the lowest deviation at these rigidities; for AMS 1998 all models yield slightly too low intensities and are quite close to each other.
2. Measurements from BESS 1999 were made in the declining phase of the $A > 0$ epoch and show similar results for all models, with the ϕ_{Uso17} model giving slightly lower deviations.
3. The BESS 2000 and 2002 observations provide less good agreements between models and measurement because they took place during the solar maximum. However, there are big differences between the models at lower rigidities. The $\phi(P)$ model yields deviations of up to 30% in 2000 and 20% in 2002, while the ϕ_{Uso11} model deviates by up to 60% and 20% and the ϕ_{Uso17} model by more than 60% for the same periods.
4. BESS-Polar I was launched 2004 in the rising phase of the last $A < 0$ solar cycle. The deviations show similar behavior as before: at higher rigidities all models show comparable and good results, while below 5 GV only the $\phi(P)$ model gives deviations of less than 10%. As in 2002, for the very low investigated rigidities all models provide too high intensities.
5. The comparisons in 2007, 2008, and 2010 with BESS-Polar II and PAMELA, respectively, all took place during the last $A < 0$ epoch and yield comparable results: the models for $\phi(P)$ and ϕ_{Uso17} show good agreements with the measurements, while the ϕ_{Uso11} model shows big deviations below 5 GV.

In summary, we state that for all analyzed time intervals from 1997 to 2010, covering the last $A > 0$ epoch and its declining phase as well as the last $A < 0$ epoch with its rising phase, the $\phi(P)$ model yields the lowest deviations and delivers for almost all cases good results. The ϕ_{Uso17} model shows good agreements with the measurements for all observations in the $A < 0$ solar cycle, at which it has been calibrated to the measurements. But it has the biggest deviations in the solar maximum phase and underestimates the intensities in the last $A > 0$ solar cycle. The ϕ_{Uso11} model can only describe the measurements at all rigidities during some intervals in the last $A > 0$ solar cycle and for one measurement at solar maximum; apart from that it shows big deviations below 5 GV.

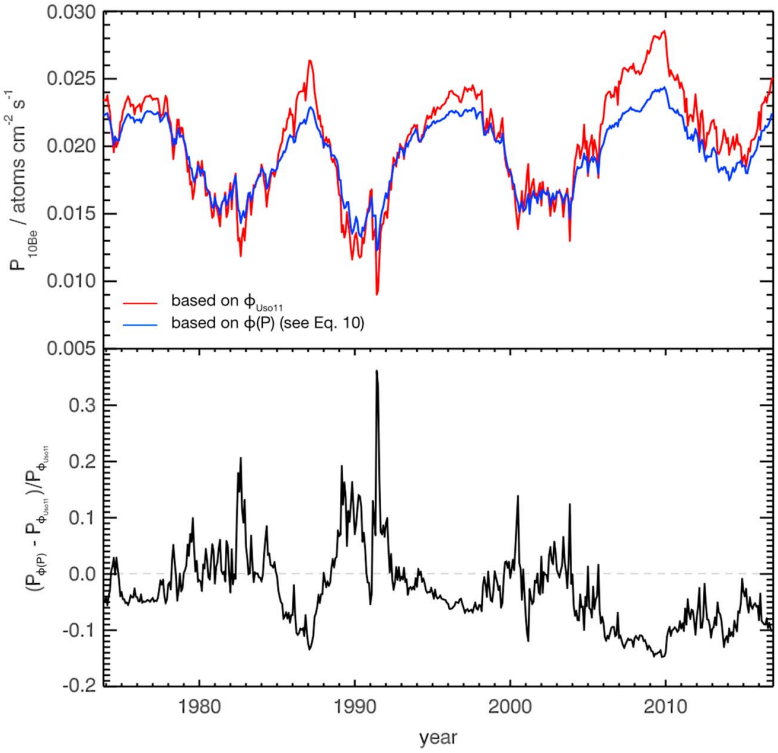

Figure 11. (top) Time profiles of global ^{10}Be production rate values based on the solar modulation parameter by Usoskin et al. (2011) (red line) and $\phi(P)$ from equation (10) (blue line). (bottom) Deviation of these two production rate values.

5. Importance of the New Solar Modulation Potential Values for the Production Rate Values of ^{10}Be

The production of secondary particles within the Earth's atmosphere strongly depends on the GCR flux interacting with the atmospheric constituents. These secondary particles may also produce so-called cosmogenic radionuclides like ^{10}Be, ^{14}C, and ^{36}Cl, which are often used as a proxy of the solar activity on time scales of thousands of years (see, e. g. Muscheler et al., 2016; Steinhilber et al., 2012). Since there is an anticorrelation between the production and the solar activity, the force field solution and its solar modulation potential ϕ is commonly used to compute the production rate values. For further information on the computations itself see, for example, Herbst et al. (2017).

In order to estimate the influence of changes in the solar modulation potential due to the analysis of its rigidity dependence as described in section 3.4, we compute the global production rate values of ^{10}Be for the newly presented rigidity-dependent $\phi(P)$ as defined in equation (10). Figure 11 (top) shows the temporal evolution of the global ^{10}Be production based on the solar modulation potential by Usoskin et al. (2011) (red line) as well as the newly derived $\phi(P)$ (blue line). As discussed in Herbst et al. (2017), a direct comparison is only possible because both records are based on the same LIS model (here Burger et al., 2000). It shows that the results displayed in Figure 7 are reflected in these computations. While the production rate values are in good agreement during times of similar solar modulation potential values (i.e., around 1980 and 2000) strong deviations occur when the ϕ values strongly differ from each other (i.e., around 1990 and 2010). Figure 11 (bottom) shows the deviation between the production rates based on $\phi(P)$ and ϕ_{Uso11}, respectively. Nonnegligible differences of more than $\pm$15% occur. This is of great importance, because the solar activity reconstructions from the cosmogenic radionuclide records, which go back thousands of years, are based on the solar modulation values during the spacecraft era. Utilizing the newly reconstructed rigidity-dependent $\phi(P)$ values may have a strong influence on these reconstructions.

Note that this analysis has not been performed for the newer solar modulation potential values from Usoskin et al. (2017) based on the LIS by Vos and Potgieter (2015). As noted before due to its derivation ϕ_{Uso17} reflects the solar modulation as observed by PAMELA proton measurements and not by neutron monitors. Thus, using ϕ_{Uso17}, we lack information of the solar modulation at higher rigidities, and therefore, we cannot derive a rigidity dependence based on this parameter.

6. Summary

In this work we have demonstrated that the commonly used force field approach shows a significant rigidity dependence below 10 GV. As a simple yet sufficient work-around we introduced a modification to the model using two solar modulation potential parameters determined by GCR measurements at different rigidities. Thus, we were able to provide a monthly rigidity-dependent solar modulation potential for the period from 1973 to 2016, covering two $A > 0$ and two $A < 0$ solar magnetic cycles. It can easily be calculated following equation (10) using the Data Set S1 included in the supporting information of this manuscript (also online at http://www.ieap.uni-kiel.de/et/ag-heber/cosmicrays).

In order to obtain the solar modulation potential for protons at around 1.28 GV for the whole time period of more than 40 years, we took advantage of the fact that different GCR ions show the same temporal behavior in the inner heliosphere if compared at the same rigidity. Thus, we could use IMP-8 helium and ACE/CRIS carbon measurements, normalized to PAMELA proton observations, to obtain so called 1.28 GV proton proxies, which were then used to calculate the corresponding solar modulation potential at these lower rigidities. In addition, we utilized the solar modulation potential calculated by Usoskin et al. (2011) from neutron monitor measurements for higher rigidities. Compared to newer findings by the same authors (Usoskin et al., 2017), this potential was found to reflect the neutron monitors observations best. These two modulation potentials at mean rigidities of approximately 1.28 GV and 13.83 GV already demonstrate the rigidity dependence of the force field approach. The significance of this dependency has been emphasized by the full rigidity-dependent solar modulation function, which we calculated from PAMELA proton spectra from 2006 to 2010 by connecting our two modulation potentials from spacecraft and neutron monitor observations with an empirical rigidity transition function. We compared the rigidity-independent modulation potentials from Usoskin et al. (2011, 2017) and from our proton proxies together with the newly derived rigidity-dependent potential function to independent observations by AMS-01, BESS, and BESS-Polar (as well as dependent PAMELA measurements) for time periods from 1997 to 2010. Thereby, we could demonstrate that the here presented force field modification is the only model in the comparison that is able to describe the observed proton spectra from 1 to 100 GV in both solar polarity cycles.

The impact of the different solar modulation potentials on the production rates of the cosmogenic radionuclide ^{10}Be has been illustrated at the end of this work. We showed that the production rate values based on our newly developed rigidity-dependent solar modulation potential $\phi(P)$ have a nonnegligible difference of more than $\pm$15% from those based on the record by Usoskin et al. (2011), especially during solar minima. And although our simplified model cannot replace full numerical solutions of the transport equation, which are necessary to further investigate all propagation processes of GCRs in the heliosphere, it is an easy to use (and within its limitations reasonable) two-parameter model to describe the solar modulation during the spacecraft era, on which all solar modulation reconstructions from cosmogenic radionuclide records are based on.

Upcoming updated data sets from PAMELA and AMS-02 (with potentially higher precision) for time periods after 2010 will help to investigate the rigidity dependence of the solar modulation potential in more detail. In addition, they will improve the normalization of the proton proxies by covering not only a part of but the full $A < 0$ and also the beginning of the next $A > 0$ solar cycle.

Acknowledgments
This work was partly carried out within the framework of the bilateral BMBF-NRF-project "Astrohel" (01DG15009) funded by the Bundesministerium für Bildung und Forschung. We thank the PAMELA collaboration for providing the proton data via the Italian Space Agency (ASI) Science Data Center (http://tools.asdc.asi.it/cosmicRays.jsp). We thank the ACE/CRIS instrument team and the ACE Science Center for providing the ACE data (http://www.srl.caltech.edu/ACE/ASC/). We acknowledge the NMDB database (http://www.nmdb.eu), for providing the Kiel neutron monitor data. We thank the Sodankylä Geophysical Observatory of the University of Oulu for providing the solar modulation potential from Usoskin et al. (2005, 2011) (http://cosmicrays.oulu.fi). Sunspot number data used in this study were obtained via the web site http://www.sidc.be/silso/ courtesy of the SIDC-team, World Data Center for the production, preservation, and dissemination of the international sunspot number, Royal Observatory of Belgium. We thank the Database of Charged Cosmic Rays (http://lpsc.in2p3.fr/crdb) for providing easy access to multiple cosmic ray data sets. J. G. would like to thank M. Potgieter and D. Strauss for many fruitful discussions. The data presented in Figure 7 are included in the supporting information for this manuscript (also online at http://www.ieap.uni-kiel.de/et/ag-heber/cosmicrays).

References

Abe, K., Fuke, H., Haino, S., Hams, T., Hasegawa, M., Horikoshi, A., … Yoshimura, K. (2016). Measurements of cosmic-ray proton and helium spectra from the BESS-Polar long-duration balloon flights over Antarctica. *The Astrophysical Journal*, *822*, 65. https://doi.org/10.3847/0004-637X/822/2/65, 1506.01267

Adriani, O., Barbarino, G. C., Bazilevskaya, G. A., Bellotti, R., Boezio, M., Bogomolov, E. A., … Zverev, V. G. (2011a). PAMELA measurements of cosmic-ray proton and helium spectra. *Science*, *332*, 69–72. https://doi.org/10.1126/science.1199172, 1103.4055

Adriani, O., Barbarino, G. C., Bazilevskaya, G. A., Bellotti, R., Boezio, M., Bogomolov, E. A., … Zverev, V. G. (2011b). Cosmic-ray electron flux measured by the PAMELA experiment between 1 and 625 GeV. *Physical Review Letters*, *106*(20), 201101. https://doi.org/10.1103/PhysRevLett.106.201101

Aguilar, M., Aisa, D., Alpat, B., Alvino, A., Ambrosi, G., Andeen, K., … Zurbach, C. (2015). Precision measurement of the proton flux in primary cosmic rays from rigidity 1 GV to 1.8 TV with the alpha magnetic spectrometer on the international space station. *Physical Review Letters*, *114*(17), 171103. https://doi.org/10.1103/PhysRevLett.114.171103

Alcaraz, J., Alpat, B., Ambrosi, G., Anderhub, H., Ao, L., Arefiev, A., … Zimmermann, B. (2000). Cosmic protons. *Physics Letters B*, *490*, 27–35. https://doi.org/10.1016/S0370-2693(00)00970-9

Beatty, J. J., Garcia-Munoz, M., & Simpson, J. A. (1985). The cosmic-ray spectra of H-1, H-2, and He-4 as a test of the origin of the hydrogen superfluxes at solar minimum modulation. *The Astrophysical Journal*, *294*, 455–462. https://doi.org/10.1086/163311

Bisschoff, D., & Potgieter, M. S. (2016). New local interstellar spectra for protons, helium and carbon derived from PAMELA and Voyager 1 observations. *Astrophysics and Space Science*, *361*, 48. https://doi.org/10.1007/ s10509-015-2633-8, 1512.04836

Burger, R. A., Potgieter, M. S., & Heber, B. (2000). Rigidity dependence of cosmic ray proton latitudinal gradients measured by the Ulysses spacecraft: Implications for the diffusion tensor. *Journal of Geophysical Research*, *105*, 27,447–27,456. https://doi.org/10.1029/2000JA000153

Caballero-Lopez, R. A (2016). An estimation of the yield and response functions for the mini neutron monitor. *Journal of Geophysical Research: Space Physics*, *121*, 7461–7469. https://doi.org/10.1002/2016JA022690

Caballero-Lopez, R. A., & Moraal, H. (2004). Limitations of the force field equation to describe cosmic ray modulation. *Journal of Geophysical Research*, *109*, A01101. https://doi.org/10.1029/2003JA010098

Cholis, I., Hooper, D., & Linden, T. (2016). A predictive analytic model for the solar modulation of cosmic rays. *Physical Review D*, *93*, 43016. https://doi.org/10.1103/PhysRevD.93.043016, 1511.01507

Corti, C., Bindi, V., Consolandi, C., & Whitman, K. (2016). Solar modulation of the local interstellar spectrum with Voyager 1, AMS-02, PAMELA, and BESS. *The Astrophysical Journal*, *829*, 8. https://doi.org/10.3847/0004-637X/829/1/8, 1511.08790

Cummings, A. C., Stone, E. C., Heikkila, B. C., Lal, N., Webber, W. R., Jóhannesson, G., … Porter, T. A. (2016). Galactic cosmic rays in the local interstellar medium: Voyager 1 observations and model results. *The Astrophysical Journal*, *831*, 18. https://doi.org/10.3847/0004-637X/831/1/18

Ghelfi, A., Barao, F., Derome, L., & Maurin, D. (2016). Non-parametric determination of H and He interstellar fluxes from cosmic-ray data. *Astronomy and Astrophysics*, *591*, A94. https://doi.org/10.1051/0004-6361/201527852

Ghelfi, A., Maurin, D., Cheminet, A., Derome, L., Hubert, G., & Melot, F. (2017). Neutron monitors and muon detectors for solar modulation studies: 2. ϕ time series. *Advances in Space Research*, *60*, 833–847. https://doi.org/10.1016/j.asr.2016.06.027, 1607.01976

Gieseler, J., Heber, B., Dunzlaff, P., Müller-Mellin, R., Klassen, A., Gómez-Herrero, R., … Mewaldt, R. A. (2008). The radial gradient of galactic cosmic rays: Ulysses KET and ACE CRIS measurements. *International Cosmic Ray Conference*, *1*, 571–574.

Gil, A., Usoskin, I. G., Kovaltsov, G. A., Mishev, A. L., Corti, C., & Bindi, V. (2015). Can we properly model the neutron monitor count rate? *Journal of Geophysical Research: Space Physics*, *120*, 7172–7178. https://doi.org/10.1002/2015JA021654

Gleeson, L. J., & Axford, W. I. (1968). Solar modulation of galactic cosmic rays. *The Astrophysical Journal*, *154*, 1011. https://doi.org/10.1086/149822

Gleeson, L. J., & Urch, I. H. (1973). A study of the force-field equation for the propagation of galactic cosmic rays. *Astrophysics and Space Science*, *25*, 387–404. https://doi.org/10.1007/BF00649180

Gurnett, D. A., Kurth, W. S., Burlaga, L. F., & Ness, N. F. (2013). In situ observations of interstellar plasma with Voyager 1. *Science*, *341*, 1489–1492. https://doi.org/10.1126/science.1241681

Heber, B., Gieseler, J., Dunzlaff, P., Gómez-Herrero, R., Klassen, A., Müller-Mellin, R., … Ferreira, S. E. S. (2008). Latitudinal gradients of galactic cosmic rays during the 2007 solar minimum. *The Astrophysical Journal*, *689*, 1443–1447. https://doi.org/10.1086/592596

Herbst, K., Kopp, A., Heber, B., Steinhilber, F., Fichtner, H., Scherer, K., & Matthiä, D. (2010). On the importance of the local interstellar spectrum for the solar modulation parameter. *Journal of Geophysical Research*, *115*, D00I20. https://doi.org/10.1029/2009JD012557

Herbst, K., Muscheler, R., & Heber, B. (2017). The new local interstellar spectra and their influence on the production rates of the cosmogenic radionuclides ^{10}Be and ^{14}C. *Journal of Geophysical Research: Space Physics*, *121*, 23–34. https://doi.org/10.1002/2016JA023207

Jokipii, J. R., Levy, E. H., & Hubbard, W. B. (1977). Effects of particle drift on cosmic-ray transport I—General properties, application to solar modulation. *The Astrophysical Journal*, *213*, 861–868. https://doi.org/10.1086/155218

Kota, J., & Jokipii, J. R. (1983). Effects of drift on the transport of cosmic rays VI—A three-dimensional model including diffusion. *The Astrophysical Journal*, *265*, 573–581. https://doi.org/10.1086/160701

Kühl, P., Dresing, N., Heber, B., & Klassen, A. (2017). Solar energetic particle events with protons above 500 MeV between 1995 and 2015 measured with SOHO/EPHIN. *Solar Physics*, *292*, 10. https://doi.org/10.1007/s11207-016-1033-8

Maurin, D., Melot, F., & Taillet, R. (2014). A database of charged cosmic rays. *Astronomy and Astrophysics*, *569*, A32. https://doi.org/10.1051/0004-6361/201321344, 1302.5525

McDonald, F. B., Webber, W. R., & Reames, D. V. (2010). Unusual time histories of galactic and anomalous cosmic rays at 1 AU over the deep solar minimum of cycle 23/24. *Geophysical Research Letters*, *37*, L18101. https://doi.org/10.1029/2010GL044218

Mewaldt, R. A., Looper, M. D., Cohen, C. M. S., Haggerty, D. K., Labrador, A. W., Leske, R. A., … von Rosenvinge, T. T. (2012). Energy spectra, composition, and other properties of ground-level events during solar cycle 23. *Space Science Reviews*, *171*, 97–120. https://doi.org/10.1007/s11214-012-9884-2

Mishev, A. L., Usoskin, I. G., & Kovaltsov, G. A. (2013). Neutron monitor yield function: New improved computations. *Journal of Geophysical Research: Space Physics*, *118*, 2783–2788. https://doi.org/10.1002/jgra.50325

Moraal, H. (2013). Cosmic-ray modulation equations. *Space Science Reviews*, *176*, 299–319. https://doi.org/10.1007/s11214-011-9819-3

Muscheler, R., Adolphi, F., Herbst, K., & Nilsson, A. (2016). The revised sunspot record in comparison to cosmogenic radionuclide-based solar activity reconstructions. *Solar Physics*, *291*, 3025–3043. https://doi.org/10.1007/s11207-016-0969-z

Parker, E. N. (1965). The passage of energetic charged particles through interplanetary space. *Planetary and Space Science*, *13*, 9–49. https://doi.org/10.1016/0032-0633(65)90131-5

Potgieter, M. (2013). Solar modulation of cosmic rays. *Living Reviews in Solar Physics*, *10*, 3. https://doi.org/10.12942/lrsp-2013-3, 1306.4421.

Potgieter, M. S., & Moraal, H. (1985). A drift model for the modulation of galactic cosmic rays. *The Astrophysical Journal*, *294*, 425–440. https://doi.org/10.1086/163309

Potgieter, M. S., Vos, E. E., Munini, R., Boezio, M., & Di Felice, V. (2015). Modulation of galactic electrons in the heliosphere during the unusual solar minimum of 2006–2009: A modeling approach. *The Astrophysical Journal*, *810*, 141. https://doi.org/10.1088/0004-637X/810/2/141

Reinecke, J. P. L., & Potgieter, M. S. (1994). An explanation for the difference in cosmic ray modulation at low and neutron monitor energies during consecutive solar minimum periods. *Journal of Geophysical Research*, *99*, 14,761–14,767. https://doi.org/10.1029/94JA00792

Richardson, J. D., Kasper, J. C., Wang, C., Belcher, J. W., & Lazarus, A. J. (2008). Cool heliosheath plasma and deceleration of the upstream solar wind at the termination shock. *Nature*, *454*, 63–66. https://doi.org/10.1038/nature07024

Scherer, K., Fichtner, H., Strauss, R. D., Ferreira, S. E. S., Potgieter, M. S., & Fahr, H.-J. (2011). On cosmic ray modulation beyond the heliopause: Where is the modulation boundary? *The Astrophysical Journal*, *735*, 128. https://doi.org/10.1088/0004-637X/735/2/128
Shalchi, A. (2015). Analytic forms of the perpendicular diffusion coefficient in NRMHD turbulence. *The Astrophysical Journal*, *799*, 232. https://doi.org/10.1088/0004-637X/799/2/232
Shikaze, Y., Haino, S., Abe, K., Fuke, H., Hams, T., Kim, K. C., … Yoshimura, K. (2007). Measurements of 0.2 20 GeV/n cosmic-ray proton and helium spectra from 1997 through 2002 with the BESS spectrometer. *Astroparticle Physics*, *28*, 154–167. https://doi.org/10.1016/j.astropartphys.2007.05.001, astro-ph/0611388
Steinhilber, F., Abreu, J. A., & Beer, J. (2008). Solar modulation during the Holocene. *Astrophysics and Space Sciences Transactions*, *4*, 1–6. https://doi.org/10.5194/astra-4-1-2008
Steinhilber, F., Abreu, J. A., Beer, J., Brunner, I., Christl, M., Fischer, H., … Wilhelms, F. (2012). 9,400 years of cosmic radiation and solar activity from ice cores and tree rings. *Proceedings of the National Academy of Sciences*, *109*(16), 5967–5971. https://doi.org/10.1073/pnas.1118965109
Stone, E. C., Cummings, A. C., McDonald, F. B., Heikkila, B. C., Lal, N., & Webber, W. R. (2005). Voyager 1 explores the termination shock region and the heliosheath beyond. *Science*, *309*, 2017–2020. https://doi.org/10.1126/science.1117684
Stone, E. C., Cummings, A. C., McDonald, F. B., Heikkila, B. C., Lal, N., & Webber, W. R. (2013). Voyager 1 observes low-energy galactic cosmic rays in a region depleted of heliospheric ions. *Science*, *341*, 150–153. https://doi.org/10.1126/science.1236408
Strauss, R. D., Potgieter, M. S., Büsching, I., & Kopp, A. (2011). Modeling the modulation of galactic and Jovian electrons by stochastic processes. *The Astrophysical Journal*, *735*, 83. https://doi.org/10.1088/0004-637X/735/2/83
Tautz, R. C., Shalchi, A., & Dosch, A. (2014). Pitch-angle scattering of energetic particles with adiabatic focusing. *The Astrophysical Journal*, *794*, 138. https://doi.org/10.1088/0004-637X/794/2/138, 1408.6947
Thakur, N., Gopalswamy, N., Mäkelä, P., Akiyama, S., Yashiro, S., & Xie, H. (2016). Two exceptions in the large sep events of solar cycles 23 and 24. *Solar Physics*, *291*, 513–530. https://doi.org/10.1007/s11207-015-0830-9
Usoskin, I. G., Alanko-Huotari, K., Kovaltsov, G. A., & Mursula, K. (2005). Heliospheric modulation of cosmic rays: Monthly reconstruction for 1951–2004. *Journal of Geophysical Research*, *110*, A12108. https://doi.org/10.1029/2005JA011250
Usoskin, I. G., Bazilevskaya, G. A., & Kovaltsov, G. A. (2011). Solar modulation parameter for cosmic rays since 1936 reconstructed from ground-based neutron monitors and ionization chambers. *Journal of Geophysical Research*, *116*, A02104. https://doi.org/10.1029/2010JA016105
Usoskin, I. G., Gil, A., Kovaltsov, G. A., & Alexander, L. (2017). Heliospheric modulation of cosmic rays during the neutron monitor era: Calibration using PAMELA data for 2006–2010. *Journal of Geophysical Research: Space Physics*, *122*, 3875–3887. https://doi.org/10.1002/2016JA023819
Vonmoos, M., Beer, J., & Muscheler, R. (2006). Large variations in Holocene solar activity Constraints from ^{10}Be in the Greenland ice core project ice core. *Journal of Geophysical Research*, *111*, A10105. https://doi.org/10.1029/2005JA011500
Vos, E. E., & Potgieter, M. S. (2015). New modeling of galactic proton modulation during the minimum of solar cycle 23/24. *The Astrophysical Journal*, *815*, 119. https://doi.org/10.1088/0004-637X/815/2/119
Webber, W. R., Heber, B., & Lockwood, J. A. (2005). Time variations of cosmic ray electrons and nuclei between 1978 and 2004: Evidence for charge-dependent modulation organized by changes in solar magnetic polarity and current sheet tilt. *Journal of Geophysical Research*, *110*, A12107. https://doi.org/10.1029/2005JA011291
Webber, W. R., & Higbie, P. R. (2003). Production of cosmogenic Be nuclei in the Earth's atmosphere by cosmic rays: Its dependence on solar modulation and the interstellar cosmic ray spectrum. *Journal of Geophysical Research*, *108*, 1355. https://doi.org/10.1029/2003JA009863
Webber, W. R., & Higbie, P. R. (2010). What Voyager cosmic ray data in the outer heliosphere tells us about ^{10}Be production in the Earth's polar atmosphere in the recent past. *Journal of Geophysical Research*, *115*, A05102. https://doi.org/10.1029/2009JA014532
Wiedenbeck, M. E., Davis, A. J., Leske, R. A., Binns, W. R., Cohen, C. M. S., Cummings, A. C., … von Rosenvinge, T. T. (2005). The level of solar modulation of galactic cosmic rays from 1997 to 2005 as derived from ACE measurements of elemental energy spectra. In *Proceedings of the 29th International Cosmic Ray Conference*, *2* (pp. 277–280). Pune, India: Tata Institute of Fundamental Research.

Erratum

Four adjustments have been made to the originally published version of this article to correct errors introduced in the typesetting process. These include correction of a typo in the key points, updates to the Supporting Information files, and removal of mention of one incorrect funding source. The present version may be considered the authoritative version of record.

As already mentioned in Sect. 1.3, there exists a variety of different models to describe the LIS of GCRs. Recent Voyager 1 observations (Stone et al., 2013; Cummings et al., 2016) allowed for the first direct measurement of the LIS, thus setting clear boundaries for the LIS models. Especially the LIS from Burger et al. (2000) as given by Usoskin et al. (2005), which we used for our analysis in this chapter, has been derived prior to the new Voyager 1 findings and does not agree well with these measurements (see Fig. 5 in Sect. 1.3). Nevertheless, for the time being we chose to use this LIS so that the solar modulation potentials from Usoskin et al. (2005, 2011) can be used, which are based on this LIS (cf. Sect. 5.1.3). This was done because obtaining the the solar modulation potential from neutron monitor measurements is not a straightforward process and depends, among others, on the yield function of the individual neutron monitor (e.g. Mishev et al., 2013; Mangeard et al., 2016). However, for the future it would be worthwhile to conduct the same analysis as in Usoskin et al. (2005, 2011) but this time with a newer, more accurate LIS model.

The modification of the underlying LIS model of course changes the resulting solar modulation potential (again, cf. Sect. 5.1.3). This directly affects the rigidity dependence we derived for the modulation potentials shown in Fig. 8 in Sect. 5.1.3, and analytically used in Eq. 10 in Sect. 5.1.4. Figure 12 illustrates this effect. Like Fig. 8 of Sect. 5.1.3, it shows the solar modulation potentials derived from PAMELA proton measurements for each rigidity bin and monthly measurement interval between 2006 and 2010. But this time the recent LIS models by Herbst et al. (2017, cf. Fig. 5 in Sect. 1.3) and Vos and Potgieter (2015) were used to calculate the modulation potentials in the top and bottom panel of Fig. 12, respectively. The resulting rigidity dependences show a similar trend like before: At lower rigidities up to around 1 GV there is almost no dependence at all, whereas above $\sim$3 GV the solar modulation potential values decrease with increasing rigidity. Significant deviations can be observed in the intermediate range. Here, the findings based on the LIS model from Burger et al. (2000) show a flat profile like at lower rigidities. However, the recent LIS models indicate a significant (Herbst et al., 2017) or at least moderate (Vos and Potgieter, 2015) increase between 1 and 3 GV, respectively. This leads to the fact that the derived rigidity dependence cannot anymore be described by a linear function (in linear space) as it has been done in Eq. 10 in Sect. 5.1.4. Therefore, the usage of one of these LIS models requires a modified, more complex approach in describing the rigidity dependence.

Thus, a future endeavor would be to establish a time series of solar modulation potentials for the last decades based on neutron monitor measurements using one of the recent LIS models. As already mentioned in Sect. 5.1.6, upcoming data from PAMELA and AMS-02 for time periods after 2010 would further improve the determination of the rigidity dependence of the modulation potential for this LIS. The described two-parameter force field approach could then be applied to these new findings.

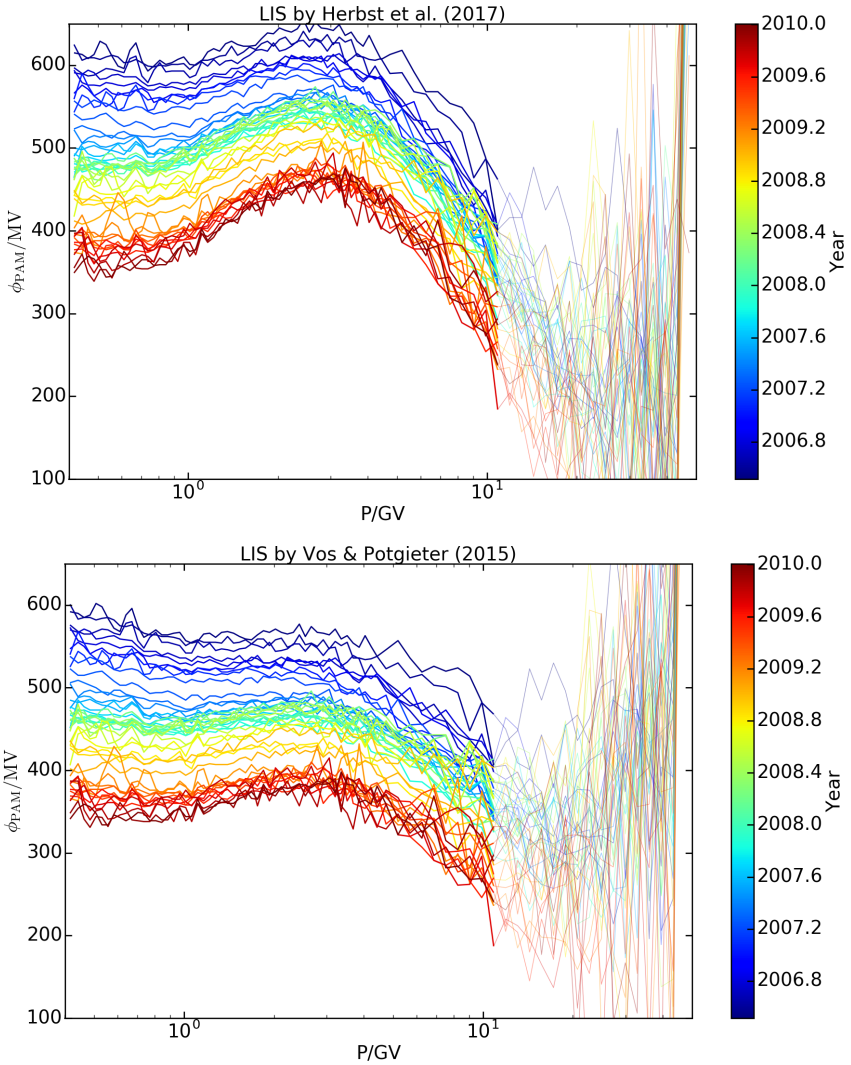

Figure 12: Solar modulation potentials derived from PAMELA proton measurements for each rigidity bin and monthly measurement interval (colored lines), using the LIS models of Herbst et al. (2017, top) and Vos and Potgieter (2015, bottom), respectively. The values above 10 GV (plotted with lighter colors) are not reliable; see text for details.

6

SUMMARY

Although GCRs were discovered more than a century ago, both their galactic origin as well as the modulation inside the heliosphere are still subject of recent investigations. The goal of this thesis was to contribute to the understanding of GCR modulation on various topics. In the two Chapts. 2 and 4, time-scales shorter than the 11-year solar cycle and charge-sign effects of the GCRs were analyzed. The study of Recurrent Cosmic Ray Decreases (RCRDs) in the time period 2007-2008 gave a recent example of periodic short-term variations of GCRs and Jovian electrons, illustrating the influence CIRs can have on the propagation of charged particles in the inner heliosphere and the resulting 27-day periodicity. In addition, this analysis pointed out the difference in the time profiles between Jovian electrons that stem from a point-like source, the magnetosphere of Jupiter, and GCRs that impinge on the heliosphere isotropically. The investigation of charge-sign effects during the 2000s $A < 0$ solar minimum was the topic of Chap. 4. This study demonstrated the HMF polarity-dependent influence of drift effects during solar minimum conditions on the intensities of GCR electrons and protons measured by Ulysses/KET in the inner heliosphere. Furthermore, it helped to understand the importance of the different modulation processes by showing that the behavior of oppositely charged GCR particles with the HMF strength and the tilt angle is essentially the same in the two $A < 0$ solar minima in the 1980s and 2000s. As laid out in Sect. 4.2, this analysis could profit much from the precise new measurements provided by PAMELA and AMS-02, and has recently been topic of a new publication using PAMELA observations (Di Felice et al., 2017). On the other hand, the findings presented in this thesis will be important for the purpose of comparison with previous solar cycles because PAMELA and AMS-02 measurements only started during or after the last solar minimum, respectively.

The newly available high-precision measurements of GCR proton spectra from 2006-2009 provided by PAMELA allowed also to significantly improve another analysis carried out for the 2000s $A < 0$ solar minimum: The calculation of the radial and more importantly the latitudinal gradients of GCRs, using measurements by Ulysses/KET on a highly inclined orbit around the Sun and a 1 AU baseline at Earth. Previously, this analysis had been done using same-rigidity helium and carbon measurements because there were no corresponding observations available at Earth. The assumption that protons, helium and carbon at the same rigidity undergo in principal the same modulation was verified later in Sect. 5.1.3, showing that this approach is valid. With the PAMELA proton measurements it was possible to confirm the previous analysis, and to study the rigidity-dependence of the latitudinal gradient in more detail than ever before. The general picture predicted by models was verified, that is, the latitudinal gradient for positively charged GCR particles from 0.45 to 2 GV has small negative values (see Fig. 11).

However, a predicted maximum around 1 GV was not observed. Furthermore, while the values at 0.45 GV match the predictions quite well, between 1 and 2 GV the measured gradients were significantly smaller than expected. Nevertheless, the fact that the latitudinal gradients were still non-zero for the period from 2006 to 2009 shows that although drift effects were somehow weaker during this unusual solar minimum, they were still non-negligible. These findings offer further insights into the distribution of GCRs in the heliosphere, confining theoretic models and helping to estimate the influence of the different modulation processes.

The last topic covered in this work once more benefited from the recent PAMELA measurements, providing the whole rigidity spectrum of GCR protons with good statistics and a high rigidity resolution from 0.4 GV up to 50 GV, thus covering the range where modulation is significant as well as the uninvolved high-rigidity parts. This allowed to investigate whether the widely used force field model is able to reproduce the full rigidity spectrum measured at Earth. The force field approach uses a given LIS for a particle species and implements the modulation in the heliosphere with a single parameter, yielding the rigidity spectrum expected to be measured at Earth. This parameter, the modulation potential, is derived to be independent of rigidity. In Chap. 5 it was shown that this is not reflected in the PAMELA measurements. Figure 8 therein clearly demonstrated the non-negligible rigidity dependence of the modulation potential. This indicates that the assumption of a linear dependence with rigidity of the diffusion coefficient, which is used in the derivation of the force field approach, is a too simple approach. But this also means that using the standard force field approach, a single parameter is not able to describe both the low-rigidity and the high-rigidity parts of the GCR spectrum. Nevertheless, because this model is commonly used, a simple workaround implementing a rigidity-dependent modulation parameter has been introduced. Utilizing the already available modulation potentials derived by neutron monitor observations (which reflect higher rigidities) as well as those obtained from spacecraft measurements at lower rigidities, this workaround allows to construct a modulation potential for a given rigidity. For this purpose, the measurements of different same-rigidity particles by previously launched smaller spacecraft detectors with limited rigidity resolution were connected to the precise proton measurements by PAMELA. The combination of these results together gave us the opportunity to provide an easy to use empirical estimate for complete rigidity spectra of GCR protons for the last 30 years.

BIBLIOGRAPHY

Adriani, O., Barbarino, G.C., Bazilevskaya, G.A., Bellotti, R., Boezio, M., Bogomolov, E.A., Bongi, M., Bonvicini, V., Borisov, S., Bottai, S. et al. Time Dependence of the Proton Flux Measured by PAMELA during the 2006 July-2009 December Solar Minimum. *Astrophys. J.*, 765:91, Mar. 2013. doi:10.1088/0004-637X/765/2/91.

Adriani, O., Barbarino, G.C., Bazilevskaya, G.A., Bellotti, R., Boezio, M., Bogomolov, E.A., Bongi, M., Bonvicini, V., Bottai, S., Bruno, A. et al. Time Dependence of the e^- Flux Measured by PAMELA during the July 2006-December 2009 Solar Minimum. *Astrophys. J.*, 810:142, Sept. 2015. doi:10.1088/0004-637X/810/2/142.

Adriani, O., Barbarino, G.C., Bazilevskaya, G.A., Bellotti, R., Boezio, M., Bogomolov, E.A., Bongi, M., Bonvicini, V., Bottai, S., Bruno, A. et al. Time Dependence of the Electron and Positron Components of the Cosmic Radiation Measured by the PAMELA Experiment between July 2006 and December 2015. *Physical Review Letters*, 116(24):241105, June 2016. doi:10.1103/PhysRevLett.116.241105.

Adriani, O., Barbarino, G.C., Bazilevskaya, G.A., Bellotti, R., Boezio, M., Bogomolov, E.A., Bongi, M., Bonvicini, V., Bruno, A., Cafagna, F. et al. Unexpected cyclic behavior in cosmic-ray protons observed by pamela at 1 au. *The Astrophysical Journal Letters*, 852(2):L28, 2018. doi:10.3847/2041-8213/aaa403.

Aguilar, M., Alberti, G., Alpat, B., Alvino, A., Ambrosi, G., Andeen, K., Anderhub, H., Arruda, L., Azzarello, P., Bachlechner, A. et al. First Result from the Alpha Magnetic Spectrometer on the International Space Station: Precision Measurement of the Positron Fraction in Primary Cosmic Rays of 0.5-350 GeV. *Physical Review Letters*, 110(14):141102, Apr. 2013. doi:10.1103/PhysRevLett.110.141102.

Aguilar, M., Aisa, D., Alpat, B., Alvino, A., Ambrosi, G., Andeen, K., Arruda, L., Attig, N., Azzarello, P., Bachlechner, A. et al. Precision Measurement of the Proton Flux in Primary Cosmic Rays from Rigidity 1 GV to 1.8 TV with the Alpha Magnetic Spectrometer on the International Space Station. *Physical Review Letters*, 114(17):171103, May 2015. doi:10.1103/PhysRevLett.114.171103.

Aguilar, M., Ali Cavasonza, L., Alpat, B., Ambrosi, G., Arruda, L., Attig, N., Aupetit, S., Azzarello, P., Bachlechner, A., Barao, F. et al. Antiproton Flux, Antiproton-to-Proton Flux Ratio, and Properties of Elementary Particle Fluxes in Primary Cosmic Rays Measured with the Alpha Magnetic Spectrometer on the International Space Station. *Physical Review Letters*, 117(9):091103, Aug. 2016. doi:10.1103/PhysRevLett.117.091103.

Bindi, V., Corti, C., Consolandi, C., Hoffman, J. and Whitman, K. Overview of galactic cosmic ray solar modulation in the AMS-02 era. *Advances in Space Research*, 60:865–878, Aug. 2017. doi:10.1016/j.asr.2017.05.025.

Bisschoff, D. and Potgieter, M.S. New local interstellar spectra for protons, helium and carbon derived from PAMELA and Voyager 1 observations. *Astrophys. Space Sci.*, 361:48, Feb. 2016. doi:10.1007/s10509-015-2633-8.

Blasi, P. The origin of galactic cosmic rays. *Astron. Astrophys. Rev.*, 21:70, Nov. 2013. doi:10.1007/s00159-013-0070-7.

Burger, R.A. and Visser, D.J. Reduction of Drift Effects due to Solar Wind Turbulence. *Astrophys. J.*, 725:1366–1372, Dec. 2010. doi:10.1088/0004-637X/725/1/1366.

Burger, R.A., Potgieter, M.S. and Heber, B. Rigidity dependence of cosmic ray proton latitudinal gradients measured by the Ulysses spacecraft: Implications for the diffusion tensor. *J. Geophys. Res.*, 105:27447–27456, Dec. 2000. doi:10.1029/2000JA000153.

Caballero-Lopez, R.A. and Moraal, H. Limitations of the force field equation to describe cosmic ray modulation. *Journal of Geophysical Research (Space Physics)*, 109:A01101, Jan. 2004. doi:10.1029/2003JA010098.

Cane, H.V. Coronal Mass Ejections and Forbush Decreases. *Space Sci. Rev.*, 93: 55–77, July 2000. doi:10.1023/A:1026532125747.

Chenette, D.L. The propagation of Jovian electrons to earth. *J. Geophys. Res.*, 85: 2243–2256, May 1980. doi:10.1029/JA085iA05p02243.

Chowdhury, P., Kudela, K. and Moon, Y.J. A Study of Heliospheric Modulation and Periodicities of Galactic Cosmic Rays During Cycle 24. *Solar Phys.*, 291: 581–602, Feb. 2016. doi:10.1007/s11207-015-0832-7.

Cliver, E.W., Richardson, I.G. and Ling, A.G. Solar Drivers of 11-yr and Long-Term Cosmic Ray Modulation. *Space Sci. Rev.*, 176:3–19, June 2013. doi:10.1007/s11214-011-9746-3.

Compton, A.H. and Getting, I.A. An Apparent Effect of Galactic Rotation on the Intensity of Cosmic Rays. *Physical Review*, 47:817–821, June 1935. doi:10.1103/PhysRev.47.817.

Corti, C., Bindi, V., Consolandi, C. and Whitman, K. Solar Modulation of the Local Interstellar Spectrum with Voyager 1, AMS-02, PAMELA, and BESS. *Astrophys. J.*, 829:8, Sept. 2016. doi:10.3847/0004-637X/829/1/8.

Cummings, A.C., Stone, E.C. and Webber, W.R. Latitudinal and radial gradients of anomalous and galactic cosmic rays in the outer heliosphere. *Geophys. Res. Lett.*, 14:174–177, Mar. 1987. doi:10.1029/GL014i003p00174.

Cummings, A.C., Stone, E.C., Heikkila, B.C., Lal, N., Webber, W.R., Jóhannesson, G., Moskalenko, I.V., Orlando, E. and Porter, T.A. Galactic Cosmic Rays in the Local Interstellar Medium: Voyager 1 Observations and Model Results. *Astrophys. J.*, 831:18, Nov. 2016. doi:10.3847/0004-637X/831/1/18.

De Simone, N., Di Felice, V., Gieseler, J., Boezio, M., Casolino, M., Picozza, P., Heber, B. and PAMELA Collaboration. Latitudinal and radial gradients of galactic cosmic ray protons in the inner heliosphere - PAMELA and Ulysses observations. *Astrophysics and Space Sciences Transactions*, 7:425–434, Sept. 2011. doi:10.5194/astra-7-425-2011.

Di Felice, V., Munini, R., Vos, E.E. and Potgieter, M.S. New Evidence for Charge-sign-dependent Modulation During the Solar Minimum of 2006 to 2009. *Astrophys. J.*, 834:89, Jan. 2017. doi:10.3847/1538-4357/834/1/89.

Ferreira, S.E.S., Potgieter, M.S., Heber, B. and Fichtner, H. Charge-sign dependent modulation in the heliosphere over a 22-year cycle. *Annales Geophysicae*, 21: 1359–1366, June 2003. doi:10.5194/angeo-21-1359-2003.

Fichtner, H. Anomalous Cosmic Rays: Messengers from the Outer Heliosphere. *Space Sci. Rev.*, 95:639–754, Feb. 2001. doi:10.1023/A:1010376901322.

Forbush, S.E. On the Effects in Cosmic-Ray Intensity Observed During the Recent Magnetic Storm. *Physical Review*, 51:1108–1109, June 1937. doi:10.1103/PhysRev.51.1108.3.

Fujii, Z. and McDonald, F.B. Radial intensity gradients of galactic cosmic rays (1972-1995) in the heliosphere. *J. Geophys. Res.*, 102:24201–24208, Oct. 1997. doi:10.1029/97JA01871.

Fujii, Z. and McDonald, F.B. The spatial distribution of galactic and anomalous cosmic rays in the heliosphere at solar minimum. *Advances in Space Research*, 35: 611–616, 2005. doi:10.1016/j.asr.2005.01.023.

Gaisser, T.K. Cosmic Rays at the Knee. In Sato, K. and Hisano, J., editors, *Energy Budget in the High Energy Universe*, pages 45–55, Mar. 2007. doi:10.1142/9789812708342_0006.

Gaisser, T.K. and Stanev, T. High-energy cosmic rays. *Nuclear Physics A*, 777: 98–110, Oct. 2006. doi:10.1016/j.nuclphysa.2005.01.024.

Galper, A.M., Sparvoli, R., Adriani, O., Barbarino, G., Bazilevskaya, G.A., Bellotti, R., Boezio, M., Bogomolov, E.A., Bongi, M., Bonvicini, V. et al. The PAMELA experiment: a decade of Cosmic Ray Physics in space. In *Journal of Physics Conference Series*, volume 798 of *Journal of Physics Conference Series*, page 012033, Jan. 2017. doi:10.1088/1742-6596/798/1/012033.

Garcia-Munoz, M., Mason, G.M. and Simpson, J.A. The anomalous He-4 component in the cosmic-ray spectrum at below approximately 50 MeV per nucleon during 1972-1974. *Astrophys. J.*, 202:265–275, Nov. 1975. doi:10.1086/153973.

Giacalone, J., Drake, J.F. and Jokipii, J.R. The Acceleration Mechanism of Anomalous Cosmic Rays. *Space Sci. Rev.*, 173:283–307, Nov. 2012. doi:10.1007/s11214-012-9915-z.

Gieseler, J. and Heber, B. Spatial gradients of GCR protons in the inner heliosphere derived from Ulysses COSPIN/KET and PAMELA measurements. *Astron. Astrophys.*, 589:A32, May 2016. doi:10.1051/0004-6361/201527972.

Gieseler, J., Dresing, N., Dunzlaff, P., Gómez-Herrero, R., Heber, B., Klassen, A., Kopp, A., Müller-Mellin, R., Potgieter, M.S. and Ferreira, S.E.S. Recurrent modulation of galactic cosmic rays: A comparative study between IMP, SOHO, STEREO, and Ulysses. *Proc. 31st Int. Cosm. Ray Conf. (Lodz, Poland)*, 2009.

Gieseler, J., Boezio, M., Casolino, M., De Simone, N., Di Felice, V., Martucci, M., Picozza, P. and Collaboration, P. Inner heliosphere spatial gradients of GCR protons in the low GeV range. *Proc. 33rd Int. Cosm. Ray Conf. (Rio de Janeiro, Brazil)*, 2013.

Gieseler, J., Heber, B. and Herbst, K. An Empirical Modification of the Force Field Approach to Describe the Modulation of Galactic Cosmic Rays Close to Earth in a Broad Range of Rigidities. *Journal of Geophysical Research (Space Physics)*, 122: 10, Nov. 2017. doi:10.1002/2017JA024763.

Gleeson, L.J. and Axford, W.I. Cosmic Rays in the Interplanetary Medium. *Astrophys. J. Lett.*, 149:L115, Sept. 1967. doi:10.1086/180070.

Gleeson, L.J. and Axford, W.I. Solar Modulation of Galactic Cosmic Rays. *Astrophys. J.*, 154:1011, Dec. 1968. doi:10.1086/149822.

Gurnett, D.A., Kurth, W.S., Burlaga, L.F. and Ness, N.F. In Situ Observations of Interstellar Plasma with Voyager 1. *Science*, 341:1489–1492, Sept. 2013. doi:10.1126/science.1241681.

Hathaway, D.H. The solar cycle. *Living Reviews in Solar Physics*, 12(1):4, Sep 2015. ISSN 1614-4961. doi:10.1007/lrsp-2015-4.

Heber, B. and Potgieter, M.S. Cosmic Rays at High Heliolatitudes. *Space Sci. Rev.*, 127:117–194, Dec. 2006. doi:10.1007/s11214-006-9085-y.

Heber, B., Droege, W., Ferrando, P., Haasbroek, L.J., Kunow, H., Mueller-Mellin, R., Paizis, C., Potgieter, M.S., Raviart, A. and Wibberenz, G. Spatial variation of >40MeV/n nuclei fluxes observed during the ULYSSES rapid latitude scan. *Astron. Astrophys.*, 316:538–546, Dec. 1996a.

Heber, B., Dröge, W., Kunow, H., Müller-Mellin, R., Wibberenz, G., Ferrando, P., Raviart, A. and Paizis, C. Spatial variation of >106 Mev proton fluxes observed during the Ulysses rapid latitude scan: Ulysses COSPIN/KET results. *Geophys. Res. Lett.*, 23:1513–1516, 1996b. doi:10.1029/96GL01042.

Heber, B., Wibberenz, G., Potgieter, M.S., Burger, R.A., Ferreira, S.E.S., Müller-Mellon, R., Kunow, H., Ferrando, P., Raviart, A., Paizis, C. et al. Ulysses Cosmic Ray and Solar Particle Investigation/Kiel Electron Telescope observations: Charge sign dependence and spatial gradients during the 1990-2000 A > 0 solar magnetic cycle. *Journal of Geophysical Research (Space Physics)*, 107:1274, Oct. 2002. doi:10.1029/2001JA000329.

Heber, B., Gieseler, J., Dunzlaff, P., Gómez-Herrero, R., Klassen, A., Müller-Mellin, R., Mewaldt, R.A., Potgieter, M.S. and Ferreira, S.E.S. Latitudinal Gradients of Galactic Cosmic Rays during the 2007 Solar Minimum. *Astrophys. J.*, 689: 1443-1447, Dec. 2008. doi:10.1086/592596.

Heber, B., Kopp, A., Gieseler, J., Müller-Mellin, R., Fichtner, H., Scherer, K., Potgieter, M.S. and Ferreira, S.E.S. Modulation of Galactic Cosmic Ray Protons and Electrons During an Unusual Solar Minimum. *Astrophys. J.*, 699:1956–1963, July 2009. doi:10.1088/0004-637X/699/2/1956.

Herbst, K., Kopp, A. and Heber, B. Influence of the terrestrial magnetic field geometry on the cutoff rigidity of cosmic ray particles. *Annales Geophysicae*, 31: 1637–1643, Oct. 2013. doi:10.5194/angeo-31-1637-2013.

Herbst, K., Muscheler, R. and Heber, B. The new local interstellar spectra and their influence on the production rates of the cosmogenic radionuclides ^{10}Be and ^{14}C. *Journal of Geophysical Research (Space Physics)*, 122:23–34, Jan. 2017. doi:10.1002/2016JA023207.

Hess, V.F. Über Beobachtungen der durchdringenden Strahlung bei sieben Freiballonfahrten. *Physikalische Zeitschrift*, 13:1084–1091, November 1912.

Hess, V.F. and Demmelmair, A. World-wide Effect in Cosmic Ray Intensity, as Observed during a Recent Magnetic Storm. *Nature*, 140:316–317, Aug. 1937. doi:10.1038/140316a0.

Jokipii, J.R. and Thomas, B. Effects of drift on the transport of cosmic rays. IV - Modulation by a wavy interplanetary current sheet. *Astrophys. J.*, 243:1115–1122, Feb. 1981. doi:10.1086/158675.

Jokipii, J.R., Levy, E.H. and Hubbard, W.B. Effects of particle drift on cosmic-ray transport. I - General properties, application to solar modulation. *Astrophys. J.*, 213:861–868, May 1977. doi:10.1086/155218.

Kühl, P., Dresing, N., Dunzlaff, P., Fichtner, H., Gieseler, J., Gómez-Herrero, R., Heber, B., Klassen, A., Kleimann, J., Kopp, A. et al. Simultaneous Analysis of Recurrent Jovian Electron Increases and Galactic Cosmic Ray Decreases. *Central European Astrophysical Bulletin*, 37:643–648, 2013.

Mangeard, P.S., Ruffolo, D., Sáiz, A., Nuntiyakul, W., Bieber, J.W., Clem, J., Evenson, P., Pyle, R., Duldig, M.L. and Humble, J.E. Dependence of the neutron monitor count rate and time delay distribution on the rigidity spectrum of primary cosmic rays. *Journal of Geophysical Research (Space Physics)*, 121:11, Dec. 2016. doi:10.1002/2016JA023515.

McComas, D.J., Alexashov, D., Bzowski, M., Fahr, H., Heerikhuisen, J., Izmodenov, V., Lee, M.A., Möbius, E., Pogorelov, N., Schwadron, N.A. et al. The Heliosphere's Interstellar Interaction: No Bow Shock. *Science*, 336:1291, June 2012. doi:10.1126/science.1221054.

McCracken, K.G. and Rao, U.R. Solar Cosmic Ray Phenomena. *Space Sci. Rev.*, 11:155–233, Oct. 1970. doi:10.1007/BF00241522.

McDonald, F.B., Ferrando, P., Heber, B., Kunow, H., McGuire, R., Müller-Mellin, R., Paizis, C., Raviart, A. and Wibberenz, G. A comparative study of cosmic ray radial and latitudinal gradients in the inner and outer heliosphere. *J. Geophys. Res.*, 102:4643–4652, Mar. 1997. doi:10.1029/96JA03673.

McKibben, R.B. Reanalysis and confirmation of positive latitude gradients for anomalous helium and Galactic cosmic rays measured in 1975-1976 with Pioneer II. *J. Geophys. Res.*, 94:17021–17033, Dec. 1989. doi:10.1029/JA094iA12p17021.

McKibben, R.B., Pyle, K.R. and Simpson, J.A. The solar latitude and radial dependence of the anomalous cosmic-ray helium component. *Astrophys. J. Lett.*, 227:L147–L152, Feb. 1979. doi:10.1086/182887.

Mewaldt, R.A., Davis, A.J., Lave, K.A., Leske, R.A., Stone, E.C., Wiedenbeck, M.E., Binns, W.R., Christian, E.R., Cummings, A.C., de Nolfo, G.A. et al. Record-setting Cosmic-ray Intensities in 2009 and 2010. *Astrophys. J. Lett.*, 723:L1–L6, Nov. 2010. doi:10.1088/2041-8205/723/1/L1.

Mishev, A.L., Usoskin, I.G. and Kovaltsov, G.A. Neutron monitor yield function: New improved computations. *Journal of Geophysical Research (Space Physics)*, 118: 2783–2788, June 2013. doi:10.1002/jgra.50325.

Moraal, H. Cosmic ray modulation studies in the outer heliosphere. *Nuclear Physics B Proceedings Supplements*, 33:161–178, May 1993. doi:10.1016/0920-5632(93)90088-N.

Moraal, H. Cosmic-Ray Modulation Equations. *Space Sci. Rev.*, 176:299–319, June 2013. doi:10.1007/s11214-011-9819-3.

Muscheler, R., Adolphi, F., Herbst, K. and Nilsson, A. The Revised Sunspot Record in Comparison to Cosmogenic Radionuclide-Based Solar Activity Reconstructions. *Solar Phys.*, 291:3025–3043, Nov. 2016. doi:10.1007/s11207-016-0969-z.

Owens, M.J. and Forsyth, R.J. The Heliospheric Magnetic Field. *Living Reviews in Solar Physics*, 10:5, Nov. 2013. doi:10.12942/lrsp-2013-5.

Parker, E.N. Dynamics of the Interplanetary Gas and Magnetic Fields. *Astrophys. J.*, 128:664, Nov. 1958. doi:10.1086/146579.

Parker, E.N. The passage of energetic charged particles through interplanetary space. *Planet. Space Sci.*, 13:9–49, Jan. 1965. doi:10.1016/0032-0633(65)90131-5.

Picozza, P., Galper, A.M., Castellini, G., Adriani, O., Altamura, F., Ambriola, M., Barbarino, G.C., Basili, A., Bazilevskaja, G.A., Bencardino, R. et al. PAMELA A payload for antimatter matter exploration and light-nuclei astrophysics. *Astroparticle Physics*, 27:296–315, Apr. 2007. doi:10.1016/j.astropartphys.2006.12.002.

Potgieter, M.S. The Modulation of Galactic Cosmic Rays in the Heliosphere: Theory and Models. *Space Sci. Rev.*, 83:147–158, Jan. 1998. doi:10.1023/A:1005014722123.

Potgieter, M.S. Solar Modulation of Cosmic Rays. *Living Reviews in Solar Physics*, 10, June 2013a. doi:10.12942/lrsp-2013-3.

Potgieter, M.S. Cosmic Rays in the Inner Heliosphere: Insights from Observations, Theory and Models. *Space Sci. Rev.*, 176:165–176, June 2013b. doi:10.1007/s11214-011-9750-7.

Potgieter, M.S. The global modulation of cosmic rays during a quiet heliosphere: A modeling perspective. *Advances in Space Research*, 60:848–864, Aug. 2017. doi:10.1016/j.asr.2016.09.003.

Potgieter, M.S., Burger, R.A. and Ferreira, S.E.S. Modulation of Cosmic Rays in the Heliosphere From Solar Minimum to Maximum: a Theoretical Perspective. *Space Sci. Rev.*, 97:295–307, May 2001. doi:10.1023/A:1011837303094.

Potgieter, M.S., Vos, E.E., Boezio, M., De Simone, N., Di Felice, V. and Formato, V. Modulation of Galactic Protons in the Heliosphere During the Unusual Solar Minimum of 2006 to 2009. *Solar Phys.*, 289:391–406, Jan. 2014. doi:10.1007/s11207-013-0324-6.

Quenby, J.J. The theory of cosmic-ray modulation. *Space Sci. Rev.*, 37:201–267, Apr. 1984. doi:10.1007/BF00226364.

Richardson, I.G. Energetic Particles and Corotating Interaction Regions in the Solar Wind. *Space Sci. Rev.*, 111:267–376, Apr. 2004. doi:10.1023/B:SPAC.0000032689.52830.3e.

Richardson, J.D., Kasper, J.C., Wang, C., Belcher, J.W. and Lazarus, A.J. Cool heliosheath plasma and deceleration of the upstream solar wind at the termination shock. *Nature*, 454:63–66, July 2008. doi:10.1038/nature07024.

Scherer, K. and Fichtner, H. The Return of the Bow Shock. *Astrophys. J.*, 782:25, Feb. 2014. doi:10.1088/0004-637X/782/1/25.

Schwadron, N.A., Möbius, E., Leonard, T., Fuselier, S.A., McComas, D.J., Heirtzler, D., Kucharek, H., Rahmanifard, F., Bzowski, M., Kubiak, M.A. et al. Determination of Interstellar He Parameters Using Five Years of Data from the IBEX: Beyond Closed Form Approximations. *Astrophys. J., Supplement*, 220:25, Oct. 2015. doi:10.1088/0067-0049/220/2/25.

Schwenn, R. Large-Scale Structure of the Interplanetary Medium. In Schwenn, R. and Marsch, E., editors, *Physics of the Inner Heliosphere I*, page 99. Springer-Verlag Berlin Heidelberg, 1990.

Schwenn, R. Space weather: The solar perspective. *Living Reviews in Solar Physics*, 3(1):2, Aug 2006. ISSN 1614-4961. doi:10.12942/lrsp-2006-2.

Simpson, J.A. Cosmic-Radiation Intensity-Time Variations and Their Origin. III. The Origin of 27-Day Variations. *Physical Review*, 94:426–440, Apr. 1954. doi:10.1103/PhysRev.94.426.

Simpson, J.A., Zhang, M. and Bame, S. A Solar Polar North-South Asymmetry for Cosmic-Ray Propagation in the Heliosphere: The ULYSSES Pole-to-Pole Rapid Transit. *Astrophys. J. Lett.*, 465:L69, July 1996. doi:10.1086/310127.

Smart, D.F. and Shea, M.A. Fifty years of progress in geomagnetic cutoff rigidity determinations. *Advances in Space Research*, 44:1107–1123, Nov. 2009. doi:10.1016/j.asr.2009.07.005.

Stoker, P.H. The IGY and beyond: A brief history of ground-based cosmic-ray detectors. *Advances in Space Research*, 44:1081–1095, Nov. 2009. doi:10.1016/j.asr.2008.10.037.

Stone, E.C., Cummings, A.C., McDonald, F.B., Heikkila, B.C., Lal, N. and Webber, W.R. Voyager 1 Explores the Termination Shock Region and the Heliosheath Beyond. *Science*, 309:2017–2020, Sept. 2005. doi:10.1126/science.1117684.

Stone, E.C., Cummings, A.C., McDonald, F.B., Heikkila, B.C., Lal, N. and Webber, W.R. Voyager 1 Observes Low-Energy Galactic Cosmic Rays in a Region Depleted of Heliospheric Ions. *Science*, 341:150–153, July 2013. doi:10.1126/science.1236408.

Strauss, R.D.T. and Effenberger, F. A hitch-hiker's guide to stochastic differential equations. *Space Science Reviews*, 212(1):151–192, Oct 2017. ISSN 1572-9672. doi:10.1007/s11214-017-0351-y.

Teegarden, B.J., McDonald, F.B., Trainor, J.H., Webber, W.R. and Roelof, E.C. Interplanetary Mev electrons of Jovian origin. *J. Geophys. Res.*, 79:3615, 1974. doi:10.1029/JA079i025p03615.

Usoskin, I.G. A History of Solar Activity over Millennia. *Living Reviews in Solar Physics*, 10:1, Mar. 2013. doi:10.12942/lrsp-2013-1.

Usoskin, I.G., Alanko-Huotari, K., Kovaltsov, G.A. and Mursula, K. Heliospheric modulation of cosmic rays: Monthly reconstruction for 1951-2004. *Journal of Geophysical Research (Space Physics)*, 110:A12108, Dec. 2005. doi:10.1029/2005JA011250.

Usoskin, I.G., Bazilevskaya, G.A. and Kovaltsov, G.A. Solar modulation parameter for cosmic rays since 1936 reconstructed from ground-based neutron monitors and ionization chambers. *Journal of Geophysical Research (Space Physics)*, 116: A02104, Feb. 2011. doi:10.1029/2010JA016105.

Vos, E.E. and Potgieter, M.S. New Modeling of Galactic Proton Modulation during the Minimum of Solar Cycle 23/24. *Astrophys. J.*, 815:119, Dec. 2015. doi:10.1088/0004-637X/815/2/119.

Vos, E.E. and Potgieter, M.S. Global Gradients for Cosmic-Ray Protons in the Heliosphere During the Solar Minimum of Cycle 23/24. *Solar Phys.*, 291: 2181–2195, Aug. 2016. doi:10.1007/s11207-016-0945-7.

Webber, W.R. and Higbie, P.R. Production of cosmogenic Be nuclei in the Earth's atmosphere by cosmic rays: Its dependence on solar modulation and the interstellar cosmic ray spectrum. *Journal of Geophysical Research (Space Physics)*, 108: 1355, Sept. 2003. doi:10.1029/2003JA009863.

Webber, W.R., Heber, B. and Lockwood, J.A. Time variations of cosmic ray electrons and nuclei between 1978 and 2004: Evidence for charge-dependent modulation organized by changes in solar magnetic polarity and current sheet tilt. *Journal of Geophysical Research (Space Physics)*, 110:A12107, Dec. 2005. doi:10.1029/2005JA011291.

Zank, G.P., Heerikhuisen, J., Wood, B.E., Pogorelov, N.V., Zirnstein, E. and McComas, D.J. Heliospheric Structure: The Bow Wave and the Hydrogen Wall. *Astrophys. J.*, 763:20, Jan. 2013. doi:10.1088/0004-637X/763/1/20.

Zieger, B., Opher, M., Schwadron, N.A., McComas, D.J. and Tóth, G. A slow bow shock ahead of the heliosphere. *Geophys. Res. Lett.*, 40:2923–2928, June 2013. doi:10.1002/grl.50576.

APPENDIX: TABLE OF ϕ-VALUES

Table 1: ϕ-values derived from proton proxies (IMP-8 He and ACE/CRIS C) and from Usoskin et al. (2011). $\Delta\phi_{pp}$ as defined by Eq. 7 in Sect. 5.1.3, $\Delta\phi_{Uso11} = 26$ MV for the observed period. All potentials are given in MV.

year	ϕ_{pp}	$\Delta\phi_{pp}$	ϕ_{Uso11}
1973.833	503	16	416
1973.915	497	16	418
1974.0	489	16	420
1974.085	493	16	402
1974.162	510	15	438
1974.247	516	15	461
1974.329	532	15	527
1974.414	564	14	567
1974.496	615	13	630
1974.581	590	14	563
1974.666	584	14	605
1974.748	607	13	590
1974.833	617	13	565
1974.915	596	14	499
1975.0	571	14	494
1975.085	545	15	459
1975.162	532	15	450
1975.247	519	15	429
1975.329	505	22	420
1975.414	496	18	407
1975.496	497	16	417
1975.581	506	16	442
1975.666	506	16	436
1975.748	508	16	437
1975.833	522	15	471
1975.915	519	16	448

Table 1 – continued

year	ϕ_{pp}	$\Delta\phi_{pp}$	ϕ_{Uso11}
1976.0	517	15	446
1976.085	525	15	440
1976.164	520	16	436
1976.249	529	16	461
1976.331	521	15	434
1976.415	506	16	426
1976.497	489	16	412
1976.582	482	16	408
1976.667	476	16	407
1976.749	480	16	408
1976.833	479	16	404
1976.915	480	16	411
1977.0	485	16	421
1977.085	493	16	417
1977.162	492	16	419
1977.247	490	16	416
1977.329	480	16	417
1977.414	482	16	442
1977.496	509	16	487
1977.581	507	15	476
1977.666	490	16	475
1977.748	497	16	438
1977.833	487	16	408
1977.915	486	16	418
1978.0	508	16	478
1978.085	527	27	496
1978.162	571	60	510
1978.247	559	15	588
1978.329	603	14	669
1978.414	587	29	602
1978.496	627	68	591

Table 1 – continued

year	ϕ_{pp}	$\Delta\phi_{pp}$	ϕ_{Uso11}
1978.581	597	18	495
1978.666	558	32	495
1978.748	584	15	566
1978.833	603	14	528
1978.915	595	14	530
1979.0	603	14	584
1979.085	626	13	609
1979.162	663	13	653
1979.247	687	13	738
1979.329	692	13	706
1979.414	736	12	812
1979.496	752	11	799
1979.581	784	15	906
1979.666	868	20	860
1979.748	865	18	778
1979.833	810	13	774
1979.915	789	12	688
1980.0	820	10	716
1980.085	868	50	743
1980.164	829	13	686
1980.249	809	15	762
1980.331	817	11	757
1980.415	903	10	886
1980.497	956	11	885
1980.582	1011	10	855
1980.667	1042	9	866
1980.749	1075	16	960
1980.833	1103	17	1052
1980.915	1124	8	1038
1981.0	1082	14	878
1981.085	1118	15	968
1981.162	1133	16	995
1981.247	1128	42	1055
1981.329	1175	98	1124
1981.414	1141	29	967
1981.496	1104	12	930

Table 1 – continued

year	ϕ_{pp}	$\Delta\phi_{pp}$	ϕ_{Uso11}
1981.581	1083	12	923
1981.666	1058	31	871
1981.748	1074	56	1046
1981.833	1054	32	1010
1981.915	1040	17	886
1982.0	1032	60	813
1982.085	1034	171	982
1982.162	1004	182	828
1982.247	908	13	798
1982.329	866	11	758
1982.414	900	10	1009
1982.496	973	10	1258
1982.581	1044	12	1240
1982.666	1088	21	1422
1982.748	1123	23	1222
1982.833	1099	23	1150
1982.915	1113	23	1256
1983.0	1151	25	1086
1983.085	1060	48	969
1983.162	1019	21	877
1983.247	1009	15	874
1983.329	1016	21	1029
1983.414	1034	20	928
1983.496	984	9	826
1983.581	947	9	836
1983.666	906	9	803
1983.748	881	9	787
1983.833	863	9	762
1983.915	863	12	761
1984.0	806	11	709
1984.085	810	39	736
1984.164	804	62	800
1984.249	789	80	846
1984.331	884	44	967
1984.415	912	20	880
1984.497	853	11	842

Table 1 – continued

year	ϕ_{pp}	$\Delta\phi_{pp}$	ϕ_{Uso11}
1984.582	821	32	778
1984.667	788	22	753
1984.749	795	29	751
1984.833	799	186	772
1984.915	806	73	746
1985.0	799	80	724
1985.085	769	13	656
1985.162	769	13	636
1985.247	758	12	609
1985.329	748	12	596
1985.414	734	12	542
1985.496	735	48	549
1985.581	706	12	543
1985.666	672	14	501
1985.748	638	15	495
1985.833	629	13	464
1985.915	630	15	485
1986.0	629	13	486
1986.085	628	17	575
1986.162	661	16	507
1986.247	629	13	434
1986.329	611	14	416
1986.414	587	14	405
1986.496	564	14	403
1986.581	568	14	402
1986.666	560	15	401
1986.748	553	15	378
1986.833	550	32	433
1986.915	544	19	382
1987.0	522	15	339
1987.085	503	18	311
1987.162	496	16	312
1987.247	500	16	328
1987.329	503	16	349
1987.414	515	16	406
1987.496	542	15	435

Table 1 – continued

year	ϕ_{pp}	$\Delta\phi_{pp}$	ϕ_{Uso11}
1987.581	562	17	468
1987.666	564	26	501
1987.748	582	14	492
1987.833	604	14	534
1987.915	603	14	534
1988.0	640	13	626
1988.085	628	13	593
1988.164	637	13	581
1988.249	646	13	602
1988.331	645	14	590
1988.415	660	13	610
1988.497	692	13	681
1988.582	677	14	697
1988.667	689	13	682
1988.749	694	13	714
1988.833	705	15	728
1988.915	709	14	819
1989.0	825	12	893
1989.085	824	11	898
1989.162	847	17	1183
1989.247	960	31	1132
1989.329	980	25	1234
1989.414	1000	18	1187
1989.496	1045	12	1022
1989.581	975	112	1114
1989.666	1146	56	1195
1989.748	1247	24	1356
1989.833	1266	22	1470
1989.915	1285	20	1362
1990.0	1269	77	1232
1990.085	1166	13	1196
1990.162	1171	13	1275
1990.247	1285	27	1424
1990.329	1329	27	1452
1990.414	1376	27	1435
1990.496	1342	18	1247

Table 1 – continued

year	ϕ_{pp}	$\Delta\phi_{pp}$	ϕ_{Uso11}
1990.581	1352	82	1294
1990.666	1307	18	1187
1990.748	1294	19	1073
1990.833	1247	15	996
1990.915	1229	13	985
1991.0	1183	9	872
1991.085	1098	20	862
1991.162	1100	35	1257
1991.247	1135	36	1197
1991.329	1166	33	1158
1991.414	1194	26	2016
1991.496	1221	20	1938
1991.581	1243	15	1471
1991.666	1201	25	1190
1991.748	1114	23	1126
1991.833	1050	9	1115
1991.915	998	10	1028
1992.0	916	11	1019
1992.085	945	10	1066
1992.164	950	14	948
1992.249	892	10	815
1992.331	864	10	860
1992.415	835	12	748
1992.497	788	27	682
1992.582	774	20	695
1992.667	741	14	724
1992.749	703	18	658
1992.833	680	24	679
1992.915	650	61	616
1993.0	655	49	632
1993.085	667	13	634
1993.162	690	35	685
1993.247	661	56	621
1993.329	624	45	599
1993.414	660	67	580
1993.496	622	67	573

Table 1 – continued

year	ϕ_{pp}	$\Delta\phi_{pp}$	ϕ_{Uso11}
1993.581	614	34	571
1993.666	592	15	548
1993.748	577	15	545
1993.833	572	15	534
1993.915	538	32	541
1994.0	562	16	536
1994.085	578	42	598
1994.162	606	13	603
1994.247	598	15	605
1994.329	596	15	576
1994.414	581	20	573
1994.496	561	15	544
1994.581	554	15	518
1994.666	537	21	497
1994.748	546	24	507
1994.833	537	20	499
1994.915	529	16	505
1995.0	515	15	484
1995.085	516	15	470
1995.162	518	15	494
1995.247	518	15	476
1995.329	513	16	468
1995.414	516	15	472
1995.496	509	16	473
1995.581	509	15	464
1995.666	504	16	459
1995.748	503	16	457
1995.833	496	16	451
1995.915	486	16	437
1996.0	488	16	436
1996.085	478	16	414
1996.164	475	16	412
1996.249	473	16	411
1996.331	478	16	419
1996.415	478	16	424
1996.497	467	16	425

Table 1 – continued

year	ϕ_{pp}	$\Delta\phi_{pp}$	ϕ_{Uso11}
1996.582	473	16	429
1996.667	478	16	431
1996.749	489	16	449
1996.833	489	16	451
1996.915	489	16	437
1997.0	479	16	418
1997.085	474	16	400
1997.162	469	16	404
1997.247	476	16	413
1997.329	474	16	404
1997.414	472	16	405
1997.496	473	16	409
1997.581	464	11	394
1997.666	462	9	404
1997.748	474	9	424
1997.833	495	10	439
1997.915	476	10	424
1998.0	478	9	427
1998.085	471	8	423
1998.162	465	8	413
1998.247	503	10	513
1998.329	556	11	572
1998.414	558	10	555
1998.496	541	9	514
1998.581	538	10	568
1998.666	524	10	515
1998.748	539	11	478
1998.833	556	10	502
1998.915	570	10	540
1999.0	594	11	602
1999.085	614	11	602
1999.162	633	11	589
1999.247	598	11	573
1999.329	608	11	589
1999.414	605	12	539
1999.496	598	10	513

Table 1 – continued

year	ϕ_{pp}	$\Delta\phi_{pp}$	ϕ_{Uso11}
1999.581	600	11	609
1999.666	655	12	691
1999.748	711	13	733
1999.833	760	14	751
1999.915	760	14	787
2000.0	826	15	752
2000.085	867	17	794
2000.164	902	18	865
2000.249	919	18	848
2000.331	951	19	967
2000.415	1022	23	1073
2000.497	1060	32	1167
2000.582	1163	26	1057
2000.667	1182	29	992
2000.749	1146	28	882
2000.833	1174	34	1023
2000.915	1234	32	960
2001.0	1268	31	881
2001.085	1196	27	774
2001.162	1155	26	725
2001.247	1267	72	995
2001.329	1117	27	874
2001.414	1089	24	832
2001.496	1037	22	808
2001.581	1062	26	904
2001.666	1059	28	897
2001.748	1100	31	959
2001.833	1069	34	865
2001.915	1027	25	833
2002.0	1024	35	977
2002.085	1003	21	826
2002.162	982	21	888
2002.247	1004	24	895
2002.329	1016	23	900
2002.414	993	20	863
2002.496	970	26	948

Table 1 – continued

year	ϕ_{pp}	$\Delta\phi_{pp}$	ϕ_{Uso11}
2002.581	1075	26	1058
2002.666	1022	23	963
2002.748	987	20	926
2002.833	1000	21	1023
2002.915	1009	21	986
2003.0	977	20	895
2003.083	995	20	892
2003.167	989	20	876
2003.25	1002	20	909
2003.333	1022	21	945
2003.417	1028	22	1067
2003.5	1020	21	959
2003.583	1003	20	908
2003.667	1041	22	869
2003.75	1031	23	963
2003.833	1124	37	1281
2003.917	1111	25	930
2004.0	1063	22	936
2004.083	1017	21	784
2004.167	944	19	705
2004.25	869	17	676
2004.333	844	16	630
2004.417	855	16	636
2004.5	809	16	693
2004.583	823	18	662
2004.667	775	15	632
2004.75	755	15	545
2004.833	747	15	645
2004.917	746	14	615
2005.0	803	19	788
2005.083	795	15	642
2005.167	771	14	620
2005.25	761	14	589
2005.333	750	15	681
2005.417	751	14	610
2005.5	752	17	643

Table 1 – continued

year	ϕ_{pp}	$\Delta\phi_{pp}$	ϕ_{Uso11}
2005.583	788	17	676
2005.667	810	20	798
2005.75	741	13	596
2005.833	715	13	542
2005.917	684	12	540
2006.0	673	12	516
2006.083	654	12	462
2006.167	627	11	435
2006.25	598	10	430
2006.333	598	11	423
2006.417	576	10	423
2006.5	582	10	443
2006.583	565	10	436
2006.667	572	10	440
2006.75	565	10	407
2006.833	560	10	408
2006.917	553	10	467
2007.0	544	10	391
2007.083	543	10	396
2007.167	531	9	376
2007.25	515	9	355
2007.333	520	9	351
2007.417	510	9	354
2007.5	503	9	357
2007.583	498	9	361
2007.667	490	9	352
2007.75	480	8	348
2007.833	492	9	353
2007.917	498	9	340
2008.0	494	9	360
2008.083	496	9	367
2008.167	495	9	362
2008.25	500	9	361
2008.333	498	9	370
2008.417	493	9	367
2008.5	480	8	356

Table 1 – continued

year	ϕ_{pp}	$\Delta\phi_{pp}$	ϕ_{Uso11}
2008.583	477	8	342
2008.667	465	8	336
2008.75	460	8	322
2008.833	453	8	302
2008.917	448	8	309
2009.0	445	8	302
2009.083	430	8	285
2009.167	417	8	276
2009.25	420	8	267
2009.333	410	7	267
2009.417	416	8	270
2009.5	409	7	269
2009.583	416	8	274
2009.667	402	7	270
2009.75	411	7	260
2009.833	407	7	258
2009.917	400	7	255
2010.0	409	7	271
2010.085	418	8	316
2010.162	441	8	347
2010.247	471	8	376
2010.329	480	8	361
2010.414	476	8	371
2010.496	481	9	377
2010.581	491	9	388
2010.666	497	9	388
2010.748	485	9	374
2010.833	504	9	389
2010.917	503	9	412
2011.0	508	9	398
2011.083	512	9	414
2011.167	558	10	426
2011.25	573	10	496
2011.333	570	11	453
2011.417	608	12	551
2011.5	619	11	518

Table 1 – continued

year	ϕ_{pp}	$\Delta\phi_{pp}$	ϕ_{Uso11}
2011.583	634	12	509
2011.667	599	12	513
2011.75	633	12	534
2011.833	614	11	488
2011.917	593	11	438
2012.0	597	12	490
2012.083	614	12	533
2012.167	677	14	634
2012.25	673	12	506
2012.333	653	12	494
2012.417	676	13	546
2012.5	700	15	664
2012.583	767	16	643
2012.667	752	14	583
2012.75	761	14	587
2012.833	765	14	571
2012.917	781	14	544
2013.0	720	13	533
2013.083	706	13	530
2013.167	712	13	564
2013.25	739	14	559
2013.333	807	18	674
2013.417	867	18	679
2013.5	854	16	665
2013.583	848	16	640
2013.667	886	17	614
2013.75	884	18	571
2013.833	875	18	590
2013.917	919	20	625
2014.0	921	20	606
2014.083	970	23	681
2014.167	960	20	652
2014.25	909	18	633
2014.333	875	17	600
2014.417	879	17	656
2014.5	865	17	628

Table 1 – continued

year	ϕ_{pp}	$\Delta\phi_{pp}$	ϕ_{Uso11}
2014.583	827	17	590
2014.667	791	16	634
2014.75	793	15	632
2014.833	763	14	645
2014.917	772	14	731
2015.0	783	14	695
2015.083	790	15	686
2015.167	839	16	743
2015.25	867	17	705
2015.333	826	16	655
2015.417	769	17	666
2015.5	737	14	617
2015.583	742	13	612
2015.667	723	13	611
2015.75	702	13	601
2015.833	691	13	585
2015.917	651	12	561
2016.0	626	11	500
2016.085	608	11	568
2016.164	589	10	475
2016.249	587	10	468
2016.331	588	10	464
2016.415	564	10	447
2016.497	564	10	464
2016.582	564	10	438
2016.667	542	9	436
2016.749	524	9	407
2016.833	502	9	385
2016.915	481	8	386

ACKNOWLEDGEMENTS

First of all I would like to thank my supervisor, Prof. Dr. Bernd Heber, for his expertise, the guidance and all the advice throughout the years of my PhD.

I am grateful to all the co-authors of the publications I took part in. Special thanks go to all my colleagues from the PAMELA collaboration, especially to Dr. Mirko Boezio, Dr. Marco Casolino, Dr. Nicola De Simone and Dr. Valeria Di Felice for the hospitality and discussions during our mutual visits. The same is true for my South African colleagues from Potchefstroom. In particular I would like to thank Prof. Dr. Marius Potgieter, Dr. Du Toit Strauss and Dr. Etienne Vos for all the fruitful discussions.

All the kind people from the Extraterrestrial Physics working group at the University of Kiel deserve my very special thanks. It has always been a pleasure working with you! I would like to especially thank Konstantin, Nina and Patrick for proofreading this theses, and Robert for being a great office mate.

Finally, I am deeply grateful to my family and friends for their support throughout the years. Very special thanks go to my wonderful wife Nina!

EIDESSTATTLICHE ERKLÄRUNG

Ich versichere an Eides Statt, dass die vorliegende Abhandlung - abgesehen von der Beratung durch meinen Betreuer und der angegebenen Literatur - nach Inhalt und Form meine eigene Arbeit ist.

Ich versichere, dass die Arbeit weder ganz noch zum Teil schon einer anderen Stelle im Rahmen eines Prüfungsverfahrens vorgelegen hat. Teile dieser Arbeit wurden bereits in Fachzeitschriften oder Verhandlungen veröffentlicht und sind als solche gekennzeichnet. Die Quellennachweise der jeweiligen Veröffentlichungen befinden sich ausschließlich in den zugehörigen Literaturverzeichnissen und werden nicht im Literaturverzeichniss dieser Abhandlung aufgeführt.

Ich versichere, dass die Arbeit unter Einhaltung der Regeln guter wissenschaftlicher Praxis der Deutschen Forschungsgemeinschaft entstanden ist.

Kiel, 30. Januar 2018

Jan Gieseler